Photo-Carrier Dynamics and Photo-Induced Melting of Charge Density Waves in Indium Wires

Dissertation

zur Erlangung des Doktorgrades
an der Fakultät für Mathematik, Informatik und Naturwissenschaften
Fachbereich Physik
der Universität Hamburg

vorgelegt von

Mariana Chávez Cervantes, M.Sc.
aus Ciudad de México
México

Hamburg

2019

Eidesstattliche Versicherung / Declaration on oath

Hiermit versichere ich an Eides statt, die vorliegende Dissertationsschrift selbst verfasst und keine anderen als die angegebenen Hilfsmittel und Quellen benutzt zu haben. Die eingereichte schriftliche Fassung entspricht der auf dem elektronischen Speichermedium. Die Dissertation wurde in der vorgelegten oder einer ähnlichen Form nicht schon einmal in einem früheren Promotionsverfahren angenommen oder als ungenügend beurteilt.

I hereby declare, on oath, that I have written the present dissertation on my own and have not used other than the mentioned resources and aids. The submitted written version corresponds to the electronic submitted version. This work has never been presented to other persons or evaluation panels in the context of an examination.

Hamburg, den 17. Juni 2020   Mariana Chávez Cervantes

_____
Unterschrift der Doktorandin

Abstract

The work presented in this thesis is focused on the analysis of the transient changes in the electronic structure of quasi-one-dimensional indium wires during a light-induced insulator-to-metal transition. Due to large parallel sections on their Fermi surface, quasi-one-dimensional metals are unstable at low temperatures with respect to a lattice distortion, transforming the metallic system into an insulator. The In/Si(111)-(4 × 1) surface, made of zig-zag chains of indium atoms, is a well-known system of in-situ grown atomic wires serving as a prime example to explore the physics of one dimensional (1D) systems experimentally. Below a critical temperature of $T_c \sim 125$ K the system undergoes a structural transition into an (8×2) reconstruction, accompanied by a gap opening of $\mathcal{E}_{\mathrm{gap}} = 300$ meV at the Fermi level.

Light pulses impinging on the low-symmetry phase provide the required energy to overcome the condensation energy and transiently turn the system into the metallic state. Photoexcitation changes the occupation of different electronic orbitals, which breaks the bonds responsible for maintaining the low symmetry structure and creates new ones that favor the high symmetry structure. The light-induced phase transition was achieved in two different regimes; single-photon absorption ($\hbar\omega > \mathcal{E}_{\mathrm{gap}}$) and multiphoton absorption ($\hbar\omega < \mathcal{E}_{\mathrm{gap}}$).

To study the dynamics of the electronic structure after photoexcitation time- and angular-resolved photoemission spectroscopy (tr-ARPES) was utilized. Femtosecond extreme-ultraviolet (XUV) laser pulses were used to probe the system through photoemission spectroscopy. As a pump, femtosecond laser pulses at infrared (IR) ($\hbar\omega = 1$ eV) and mid-infrared (MIR) ($\hbar\omega = 190$ meV) wavelengths were used to trigger the phase transition. To quantify the transient phase transition the photocurrent was evaluated as a function of time in different momentum-energy regions.

In the case of single-photon absorption the structural transition was found to be completed within ~ 0.66 ps. The timescale represents a fraction of the period of the amplitude mode. A lifetime of $\tau > 100$ ps of the transient metallic phase was found, explained by the existence of a metastable (4 × 1) phase at temperatures below the transition temperature T_c.

For multiphoton absorption the melting time was found to be slightly longer ($\tau \sim 1$ ps) with a significantly shorter lifetime for the transient metallic state of ~ 6 ps, indicating an incomplete structural transition.

These timescales suggest similar microscopic mechanisms for charge density wave (CDW) melting on indium-wires in single-photon and multiphoton absorption regimes.

Kurzdarstellung

Die in dieser Dissertation vorgestellte Arbeit konzentriert sich auf die Analyse der transienten Änderungen in der elektronischen Struktur von quasi-1D Indium-Drähten während eines lichtinduzierten Übergangs zwischen Isolator und Metall. Auf grund großer paralleler Bereiche auf ihrer Fermi-Fläche sind quasi-1D-Systeme bei niedrigen Temperaturen instabil hinsichtlich einer Gitterverzerrung, die das metallische System in einen Isolator umwandelt. Die In/Si(111)-(4 × 1)-Oberfläche aus Zick-Zack-Ketten von Indiumatomen ist ein bekanntes Beispiel für in-situ gewachsene Atomdrähte, um die 1D-Physik experimentell zu untersuchen. Unterhalb von einer kritischen Temperatur $T_c \sim 125$ K durchläuft das System einen strukturellen Übergang in eine (8 × 2) Struktur, die einer Bandlücke von 300 meV aufweist.

Lichtpulse, die auf das System in der Phase niedriger Symmetrie treffen, können von ihm absorbiert werden, wodurch die notwendige Energie zur Überwindung der Kondensationsenergie bereitgestellt und das System vorübergehend in den metallischen Zustand versetzt wird. Dies verändert die Besetzung der verschiedenen elektronischen Orbitale, welche die für die Aufrechterhaltung der niedrigen Symmetriestruktur verantwortlichen Bindungen durchbrechen und solche erzeugen, die eine hohe Symmetrie begünstigen. Der lichtinduzierte Phasenübergang wurde in zwei verschiedenen Bereichen untersucht: Einzelphotonenabsorption ($\hbar\omega > \mathcal{E}_{gap}$) und Multiphotonenabsorption ($\hbar\omega < \mathcal{E}_{gap}$).

Um die Dynamik der elektronischen Struktur nach der Photoanregung zu untersuchen, wurde zeit- und winkelaufgelöste Photoemissionsspektroskopie (tr-ARPES) verwendet. Als Lichtquelle für den Photoemissionsprozess wurde das von einem Femtosekundenlaser erzeugte extrem-ultraviolette (XUV) Licht verwendet. Zur Anregung der Probe wurden zwei unterschiedliche Photonenenergien verwendet: $\hbar\omega = 1$ eV (Anregung oberhalb der Bandlücke) und $\hbar\omega = 190$ meV (Anregung unterhalb der Bandlücke). Um den transienten Phasenübergang zu quantifizieren wurde der Photostrom als Funktion der Zeit in verschiedenen Impuls und Energiebereichen ausgewertet.

Für die Einzelphotonenabsorption, wurde festgestellt, dass der Phasenübergang innerhalb von ca. $0,66$ ps abgeschlossen ist. Die Zeitskala repräsentiert einen Bruchteil der Periode der Amplitudenmode. Es wurde eine Lebensdauer von $\tau > 100$ ps des transienten metallischen Zustandes gefunden, die durch das Vorhandensein einer metastabilen Phase (4 × 1) bei Temperaturen unter der Übergangstemperatur T_c erklärt werden kann.

Für die Multiphotonenabsorption wurde festgestellt, dass die Schmelzzeit etwas länger ist ($\tau \sim 1$ ps), und es wurde eine deutlich kürzere Lebensdauer für den Metastabilezustand von $\tau \sim 6$ ps gefunden, was auf einen unvollständigen Phasenübergang hinweist.

Die gefundenen Zeitskalen deuten auf ähnliche mikroskopische Mechanismen für das Schmelzen von der Ladungsdichtewelle auf Indium-Drähten im Einzel- und Multiphotonenabsorptionsbereich hin.

" Die Grenzen meiner Sprache
bedeuten die Grenzen meiner Welt. "

Ludwig Wittgenstein

List of Publications

This thesis is the result of my work for the last 4.5 years in the Otto Hahn Group for Ultrafast Electron Dynamics at the Max Planck Institute for the Structure and Dynamics of Matter in Hamburg. The work has partly been funded by the SFB 925 "Light-induced dynamics and control of strongly correlated quantum systems". Furthermore, I was a member of the International Max Planck Research School for Ultrafast Imaging and Structural Dynamics (IMPRS-UFAST).

This is the list of publications relevant for this thesis.

[1] M. Chávez-Cervantes, G. E. Topp, S. Aeschlimann, R. Krause, S. A. Sato, M. A. Sentef, and I. Gierz. *Charge density wave melting in one-dimensional wires with femtosecond sub-gap excitation*, Phys. Rev. Lett., **123**, 036405 (2019).

MCC prepared the samples. MCC, SA and RK performed the tr-ARPES experiments. MCC and IG completed the data analysis. GET and MAS did the theoretical calculation for the absorbed energy. SAS calculated the field amplitude at the sample. MCC and IG interpreted the data with contributions of all other authors. MCC wrote the first manuscript. IG wrote the final manuscript with input of all other authors.

[2] M. Chávez-Cervantes, R. Krause, S. Aeschlimann, and I. Gierz. *Band structure dynamics in indium wires*, Phys. Rev. B, **97**, 201401 (2018).

MCC prepared the samples, performed LEED characterization and did simplified ARPES simulation. MCC, RK and SA performed the tr-ARPES experiments. MCC and IG completed the data analysis and interpretation. IG wrote the manuscript with input of all other authors.

In addition, I participated in the experiments for the following publications:

[3] S. Aeschlimann, A. Rossi, M. Chávez-Cervantes, R. Krause, B. Arnoldi, B. Stadtmüller, M. Aeschlimann, S. Forti, F. Fabbri, C. Coletti, I. Gierz. *Direct evidence for efficient ultrafast charge separation in epitaxial WS₂/graphene heterostructure*, Science Advances **6**, eaay0761 (2020).

[4] S. Aeschlimann, R. Krause, M. Chávez-Cervantes, H. Bromberger, R. Jago, E. Malić, A. Al-Temimy, C. Coletti, A. Cavalleri, and I. Gierz. *Ultrafast momentum imaging of pseudospin-flip excitations in graphene*, Phys. Rev. B, **96**, 020301 (2017).

[5] H. Bromberger, A. Ermolov, F. Belli, H. Liu, F. Calegari, M. Chávez-Cervantes, M. T. Li, C. T. Lin, A. Abdolvand, P. St. J. Russell, A. Cavalleri, J. C. Travers, and I. Gierz. *Angle-resolved photoemission spectroscopy with 9-ev photon-energy pulses generated in a gas-filled hollow-core photonic crystal fiber*, Appl. Phys. Lett., **107**, 091101 (2015).

[6] I. Gierz, F. Calegari, S. Aeschlimann, M. Chávez Cervantes, C. Cacho, R. T. Chapman, E. Springate, S. Link, U. Starke, C. R. Ast, and A. Cavalleri. *Tracking primary thermalization events in graphene with photoemission at extreme time scales*, Phys. Rev. Lett., **115**, 086803 (2015).

Contents

List of Figures

List of Tables

Introduction

Electronic devices like smart phones, smart watches, medical implants, etc. have become an essential part of our everyday life, due to the ceaseless development of smaller, faster and cheaper components. The technology employed in the individual components arises from the understanding of the electronic properties of the materials used. In many cases their behavior can be derived from simple models. However, as the components reach atomic limits their behavior will be influenced by quantum effects and many-body interactions, making it necessary to include these interactions in the models. Reaching these atomic limits in electronic devices will reduce the dimensionality, confine the particles and make them more likely to interact with each other. Electron-phonon interactions in one-dimensional systems can trigger a phase transition forming a broken-symmetry ground state with a charge density modulation. Charge density wave (CDW) ground states were first discussed by Fröhlich and Peierls in the 1950s [1, 2] but were experimentally not observed until the 1970s when materials with highly anisotropic band structures were studied [3, 4].

The design of future devices requires a deep understanding and control of the electronic properties of solids. The conventional control parameters are chemical composition, pressure, temperature and external electric or magnetic fields. Recently, femtosecond pulses have become an alternative tool for controlling the properties of solids by inducing sudden changes in the system on very short timescales. The use of femtosecond lasers as tools to modify the electronic structure of solids has lead to the discovery of light-induced phase transitions [5, 6, 7]. The study of such light-induced phase transitions can reveal the underlying microscopic mechanisms for the formation of the ground state and has an enormous potential for the development of ultrafast optoelectronic devices such as switches and detectors.

To study light-induced phase transitions and their dynamics on femtosecond timescales, we not only need femtosecond pulses as a driving force, but also to follow the evolution of the system in time. To this end, we used time- and angular-resolved photoemission spectroscopy (tr-ARPES), which is a technique that combines angular-resolved photoemission spectroscopy (ARPES) with a femtosecond laser pump-probe scheme. ARPES is based on the photoelectric effect and gives the possibility of directly studying the electronic structure of one dimensional (1D) and two dimensional (2D) systems in energy and momentum space. Time- and angular-resolved photoemission spectroscopy (tr-ARPES) allows to measure transient changes of electronic distributions when the system is perturbed by an ultrashort laser pulse. The analysis of the transient electronic distributions after photo-excitation on a femtosecond timescale can reveal the responsible microscopic mechanisms for different electronic processes.

This thesis is focused on the study of a quasi-one dimensional (1D) system: Self-assembled in-

dium wires grown on a Si(111) substrate. The system presents a structural phase transition accompanied by a metal-to-insulator transition at $T_c \sim$ 125 K. The carrier dynamics of the metallic phase as well as the light-induced insulator-to-metal transition at $T < T_c$ under two different photo-excitation mechanisms was investigated. It was found that the electronic distribution after photo-excitation of the metallic phase follows a Fermi-Dirac distribution at every time delay between pump- and probe-pulse. The investigation showed that cooling of the hot electrons happens within $\sim$ 1 ps by dissipating their energy into a phonon bath. In addition, coherent oscillations of the pump-probe signal were found, revealing strong coupling between electrons and certain phonons. From the investigation of the light-induced insulator-to-metal transition, the band structure changes were found to be completed on a timescale slightly longer than 1/4 period of the phonons responsible for the structural transition [8, 9], consistent with a Peierls transition. Afterwards, the system gets trapped in a metastable metallic phase due to the peculiar shape of the potential energy surface which exhibits two minima below the transition temperature [9, 10]. The melting dynamics observed for single-photon and multiphoton absortion agree with the microscopic picture of the photo-induced phase transition proposed in [11]: Photo-excitation transiently changes the occupation of different electronic orbitals, which breaks existing and forms new chemical bonds, leading to atomic forces that enable the structural transition.

Structure of the Thesis

The thesis is divided in 8 chapters. The first two chapters present the theoretical background. In chapter 1 the physics of a one-dimensional metal is discussed, followed by the theory of light-induced dynamics in chapter 2. The experimental results were obtained using the tr-ARPES technique. Hence, the basic principle of photoemission spectroscopy and the experimental setup and its characteristics are explained in chapter 3. Indium wires are self-assembled chains of indium atoms on a silicon wafer. They form a (4×1) surface reconstruction in the metallic phase while at low temperatures the system undergoes a phase transition into an (8×2) reconstruction. The electronic and real space structure of the indium wires, as well as the equilibrium mechanisms that lead to the phase transition at low temperatures together with the corresponding sample preparation are discussed in chapter 4. In chapter 5 the carrier dynamics in the metallic (4×1) phase after photo-excitation was investigated. The observed light-induced insulator-to-metal transition under two different excitations is presented and analyzed in chapter 6 and 7 corresponding to the results in my publications [12, 13]. Finally, in chapter 8, open question regarding the result of this thesis are discussed and further experimental ideas on how to modify the electronic properties of indium wires are outlined.

1 One-Dimensional Systems

One-Dimensional systems can be seen as a simple theoretical approach to understand the physics of more complicated systems, but they are interesting in their own right. In low-dimensional systems electrons are confined, thus enabling the interactions between them and with other particles, which can lead to symmetry-broken ground states. Fröhlich suggested in 1950 that lattice distortions were responsible of binding repellent electrons in superconductors [1]. The strength of the binding and hence the temperature at which the transition to a superconducting phase takes place depends on the rapidity of the lattice response. Little thought that the build up of positive charge by a passing electron could be accelerated if instead of moving the ions just an electron rearrangement was needed. Following this idea Little proposed in 1964 that a certain kind of chain made of organic material could confine the electrons in such a way that could exhibit superconductivity at room temperature [14]. In 1970 it was observed that the organic chain TTF-TCNQ turned into an insulator at low temperatures instead of turning superconducting. This was the first experimental example of what Peierls came across in 1955 while preparing material for a textbook [2]. He theoretically demonstrated that a metallic periodic chain of atoms with one electron per ion cannot be stable at $T = 0$ K and would turn into an insulator.

1.1 One-Dimensional Electronic Properties

In order to derive the basic electronic properties of 1D wires we first consider a gas of free electrons confined in a 1D box. Following, we will add a periodic lattice potential to the free electrons and finally consider a particular periodic lattice distortion as the origin of a metal-to-insulator transition.

1.1.1 Free Electron Gas

We consider a collection of non-interacting electrons confined in a box with length L, each electron has mass m_e and momentum p. The electronic wave functions $\psi_n(x)$ will be a solution to the Schrödinger equation $\mathcal{H}\psi = \varepsilon\psi$ of the form $\psi = Ae^{-ikx}$ with $\mathcal{H} = \frac{p^2}{2m_e} + V(x)$ where the potential $V(x) = 0$ inside the box and $V(x) = \infty$ outside. The corresponding parabolic dispersion relation is given by

$$\varepsilon_n(k_n) = \frac{\hbar^2 k_n^2}{2m_e} \tag{1.1}$$
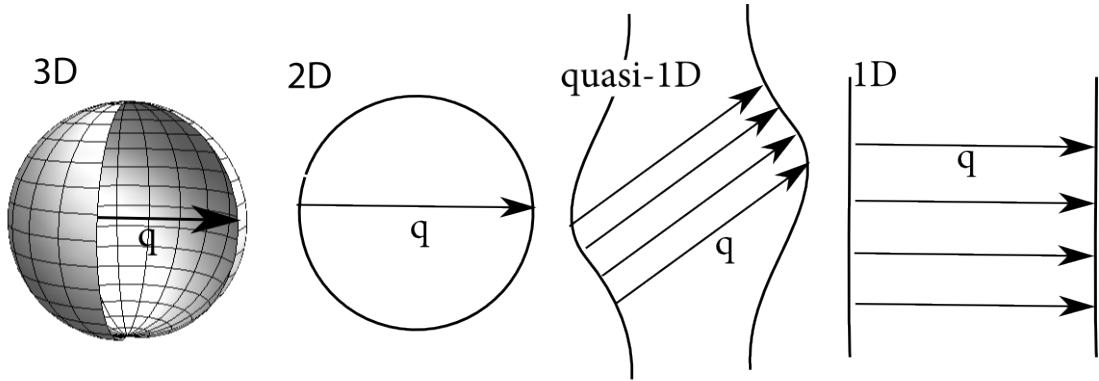
Figure 1.1 | Fermi surface. for an electron gas in 3D, 2D, quasi-1D and 1D with vector $q = 2k_F$.

where $k_n = \frac{n\pi}{2L}$ is the wave vector for electron $n \in \mathbb{N}$ and $\varepsilon_n(k_n)$ is its corresponding energy. If N is the total number of electrons, following Pauli principle the topmost filled energy level in the ground state ($T = 0\,\text{K}$) is given by the Fermi energy

$$\varepsilon_F = \frac{\hbar^2}{2m_e} \left(\frac{N\pi}{2L} \right)^2 = \frac{\hbar^2 k_F^2}{2m_e} \tag{1.2}$$

where $k_F = \frac{N\pi}{2L}$ is the Fermi wave vector. The density of states for one spin direction is

$$n(\varepsilon) = \frac{L}{\pi\hbar} \sqrt{\frac{m_e}{2\varepsilon}}. \tag{1.3}$$

At $T > 0\,\text{K}$ the kinetic energy of the electrons will increase, and therefore some levels will be occupied that were vacant before. The probability that a state with energy ε is occupied is given by the Fermi-Dirac distribution

$$f_{\text{FD}}(\varepsilon) = \frac{1}{\exp\left(\frac{\varepsilon - \mu}{k_B T}\right) + 1} \tag{1.4}$$

where μ is the chemical potential and K_B the Boltznamm constant. The Fermi surface is given by all the points that have $\varepsilon(k) = \varepsilon_F$. In one dimension it consists of the points $k_x = -k_F$, and $k_x = +k_F$ and has no dispersion in the other direction (k_y) creating two parallel lines when seen in two dimensions. A sketch of the Fermi surface for different dimensions is shown in Fig. 1.1. The Fermi surface of a quasi-1D system has two almost parallels lines. In the sketch vectors connecting parallel parts on the Fermi Surface are drawn separarted by $q = 2k_F$.

1.1.2 In a Periodic Potential: Band Gap Formation

A more realistic description of the electronic properties of a 1D solid is to consider a collection of electrons under the effect of a periodic potential $V(x + a) = V(x)$ with periodicity a (lattice constant)

given by the positions of the ions in the solid. Using Bloch's theorem, the solutions to the corresponding Schröedinger equation of such a system can be written as $\psi_k(x) = u_k(x) \exp(ik \cdot x)$ where u contains the periodicity of the chain. Finding the exact solutions can be done in different ways, for example following the Kronig-Penny model [15], doing quasi-degenerate second order perturbation theory [16], or using the tight binding model, but the result in all cases will be that no solution exists for certain values of ε and k. As a result, the continuous parabolic dispersion will be interrupted by energy gaps at the Brillouin zone boundaries $k = \frac{n\pi}{a}$. In Fig. 1.2 the band gap opening at the first Brillouin zone boundary where $k = \pm\frac{\pi}{a}$ is exemplified. In red the free electron dispersion is plotted for comparison. Depending on the total number of electrons in the system the Fermi energy can be located inside a band or in the band gap. In the former case the system will have a metallic behavior and in the latter the solid will be an insulator.
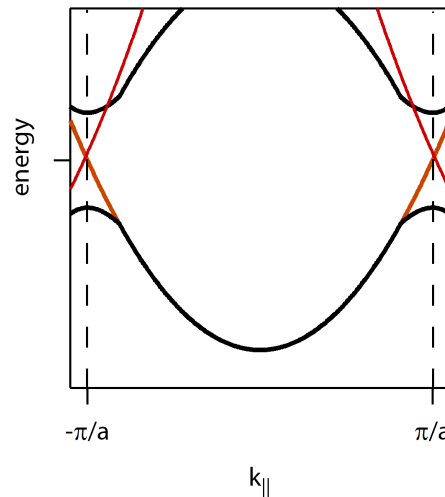
Figure 1.2 | 1D dispersion relation. 1D dispersion relation for a free electron (red), for a non interacting electron in a periodic potential (black) in the reduced zone scheme.

1.2 Peierls Instability

The Peierls instability arises from the electron-phonon interaction in the system. To intuitively explain the Peierls mechanism we can consider the same chain of atoms, with a periodic spacing a, but with just one electron per ion. The band energy will have the same shape as shown in Fig. 1.2 but the band will be just half full, i.e. $k_F = \pi/2a$ (Fig. 1.3 (a)). In the presence of electron-phonon interaction it is energetically favorable to introduce a periodic lattice distortion. If we would displace every second atom by a small distance, the atoms will form dimers and the periodicity of the chain will be $2a$ rather than a. In a similar manner as explained in the previous section, this would result in a gap $\mathcal{E}_{gap} = 2\Delta$ in the energy dispersion at the new Brillouin zone boundary $k = \pi/2a$, which for a half-filled band happens to be at k_F. As a result of the gap opening electrons at the Fermi level will

lower their energy by Δ. The dispersion for the distorted chain of atoms is shown in Fig. 1.3 (b). This distortion is energetically favorable if the decrease of electronic energy compensates the increase of elastic energy resulting from the distortion. The behavior of the electronic energy reduction for small displacements d of the atoms from its equilibrium position is proportional to $-d^2 \ln d$. The increase in elastic energy due to the lattice distortion is proportional to d^2. Therefore the decrease in electron energy must dominate for small displacements [17].
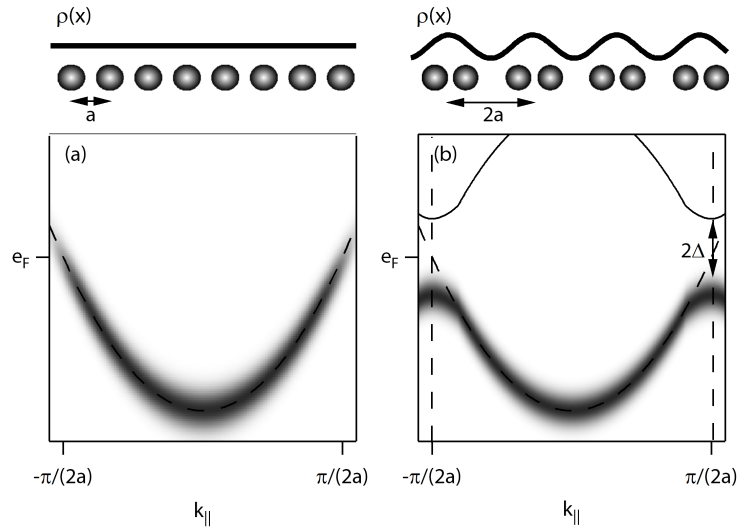
Figure 1.3 | Peierls transition. Single particle band, charge density $\rho(x)$ and lattice arrangement for a half filled atomic chain above and below the transition temperature. Adapted from [18].

Furthermore, the response of an electron gas to an external perturbation in 1D is very different from the response in higher dimensions as a consequence of its particular Fermi surface shown in Fig. 1.1. As we can see in Fig. 1.4 (a) the Lindhard response function (χ) for a 1D electron gas diverges at $q = 2k_{\mathrm{F}}$. Therefore an external perturbation ϕ_{ext} will lead to a divergent charge redistribution $\rho^{\mathrm{ind}} = \chi(q)\phi_{\mathrm{ext}}(q)$. At $T = 0\,\mathrm{K}$ the electron gas is unstable with respect to the formation of a periodically varying electron charge density with period $\lambda_0 = \frac{\pi}{k_{\mathrm{F}}}$. The biggest contributions to the Lindhard response function come from pairs of states with the same energy (one full and one empty) which differ by $q = 2k_{\mathrm{F}}$. In one dimension all the states at the Fermi level fulfill this condition, also called perfect nesting. For high temperatures the response of a 1D system is not divergent at $q = 2k_F$, i.e the electron gas is stable, as shown in 1.4 (b).
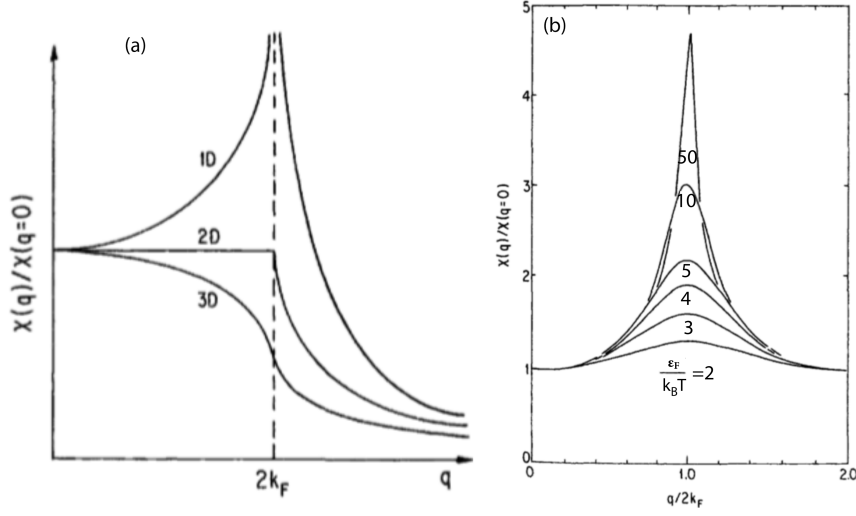
Figure 1.4 | Lindhard response function. (a) Response function vs. momentum at T = 0 for one, two and three dimensions and (b) for 1D at different temperatures. Taken form [18].

1.3 Mean Field Theory of Charge Density Waves

The main features of the transition and the collective modes of the ground state can be described by the mean field treatment of the 1D electron-phonon Hamiltonian [19], also called the Fröhlich Hamiltonian (Eq. 1.5), which is given by the sum of the individual Hamiltonians for the electronic and phononic system as well as the Hamiltonian resulting from the electron-phonon interaction.

$$\mathcal{H} = \mathcal{H}_{el} + \mathcal{H}_{ph} + \mathcal{H}_{el-ph} = \sum_{k,\sigma} \varepsilon_k c^\dagger_{k,\sigma} c_{k,\sigma} + \sum_{k,\sigma} \hbar \omega^0_q b^\dagger_q b_q + \sum_{k,q,\sigma} g(k) c^\dagger_{k+q,\sigma} c_{k,\sigma} (b_q + b^\dagger_{-q}) \tag{1.5}$$

where $c^\dagger_k (c_k)$, $b^\dagger_q (b_q)$ are the electron and phonon creation (annihilation) operators with momenta k and q, and spin σ, ε_k and ω^0_q are the electron and phonon dispersion, and $g(k)$ the electron-phonon coupling constant. The effects of the electron-phonon coupling that lead to the metal-to-insulator transition in 1D can be described by establishing the equations of motion for the normal coordinates Q_q and $P_{q'}$. Following [18] the solution gives a renormalized phonon frequency

$$\omega_{ren,q} = \omega^2_q + \frac{2g^2 \omega_q}{\hbar} \chi(q, T). \tag{1.6}$$

For a 1D electron gas $\chi(q, T)$ has its maximum value at $q = 2k_F$. Consequently, the renormalization will be most significant at this wavevector. The phonon frequency for $q = 2k_F$ is given by

$$\omega^2_{ren,2k_F} = \omega^2_{2k_F} - \frac{2g^2 n(\varepsilon_F) \omega_{2k_F}}{\hbar} \ln\left(\frac{1.14\varepsilon_F}{k_B T}\right). \tag{1.7}$$

The transition temperature T_c is defined by the temperature at which $\omega_{ren,2k_F}$ goes to zero. This happens at $T_c^{MF} = \frac{1.14\,\varepsilon_F}{k_F}\exp\left[-(\hbar\omega_{2k_F})/(g^2 n(\varepsilon_F))\right]$. For $T < T_c$ the phonon is frozen and the lattice dimerized. The electronic spectrum has a band gap at ε_F and the gap is given at by the BCS gap equation

$$2\Delta = 3.52 k_B T_c. \tag{1.8}$$

The behavior near the transition temperature can be discussed using the Ginzburg-Landau theory of phase transitions with a complex order parameter $\Delta = \Delta e^{i\phi}$. The amplitude of the complex order parameter is given by the single particle gap. The free energy for a one-dimensional chain described by the Fröhlich Hamiltonian (Eq. 1.5) is

$$F = F(0) + n(\varepsilon_F)\int \mathrm{d}x[a\Delta^2 + b\Delta^4 + ..] \tag{1.9}$$

where a and b are functions of T that depend on the microscopic quantities of the system. In Fig. 1.5 the free energy for a one-dimensional chain is depicted. The high symmetry phase is characterized by a minimum at $\Delta = 0$. As the system crosses the transition temperature the free energy surface takes a Mexican hat shape with a new ground state corresponding to $\Delta \neq 0$. The new charge density wave ground state is characterized by the amplitude Δ and the phase ϕ of the order parameter.
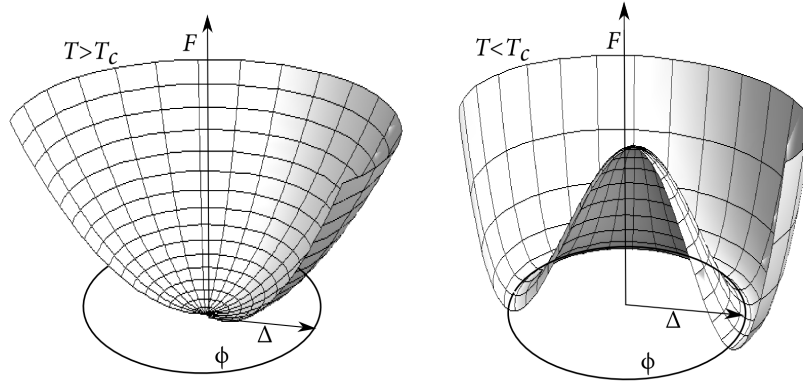
Figure 1.5 | Free energy surface. Free energy surface as a function of the amplitude Δ and phase ϕ of the complex order parameter Δ.

1.4 Collective Modes of the CDW Ground State

Fluctuations of the order parameter will give rise to collective motion of charges and atoms in the ground state. The excitation of the charge density wave ground state related to the variations of the amplitude and phase of the order parameter can be described close to $T = 0\,\mathrm{K}$ with the Ginzburg-

Landau formalism in terms of a position- and time-dependent order parameter $\Delta(x, t)$ [18]

$$\Delta(x, t) = [\Delta + \delta(x, t)]e^{i\phi(x,t)} \tag{1.10}$$

where Δ is the amplitude of the order parameter and $\delta(x, t)$ and $\phi(x, t)$ represent the amplitude and phase fluctuations, respectively, as shown in Fig. 1.6. These fluctuations can be added in the free
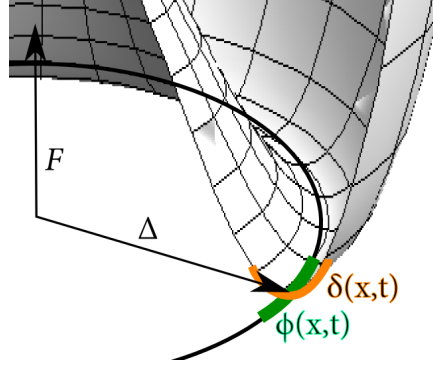
Figure 1.6 | Amplitude and phase fluctuations of the order parameter. Free energy surface around the minimum for the low-symmetry phase with fluctuations of the order parameter.

energy functional. Solving the equation of motion yields two decoupled modes, the amplitude mode which is Raman-active and the phase mode which is infrared (IR)-active. The corresponding dispersion relations at $T = 0\,\text{K}$ are shown in Fig. 1.7 (a). The excitations of the phase and amplitude modes are usually referred to as phasons and amplitudons, respectively. In general the amplitude mode excitation leads to a periodically modulated gap size, and the phase mode modulates the position of the gap in k-space. In the presence of strong electron-phonon coupling, the amplitude and phase mode excitation lead to fluctuations of the ionic position around the equilibrium position. As a result of the excitation the charge density wave formed in the ground state will also vary its amplitude. The band gap modulation, the charge distribution as well as the ionic positions for an amplitude mode excitation in a Peierls system are shown in Fig. 1.7 (b). The phase excitation represents a translational motion of the undistorted condensate and involves a phase shift of the charge density. The charge distribution as well as the ionic positions for a phase excitation are shown in Fig. 1.7 (c).
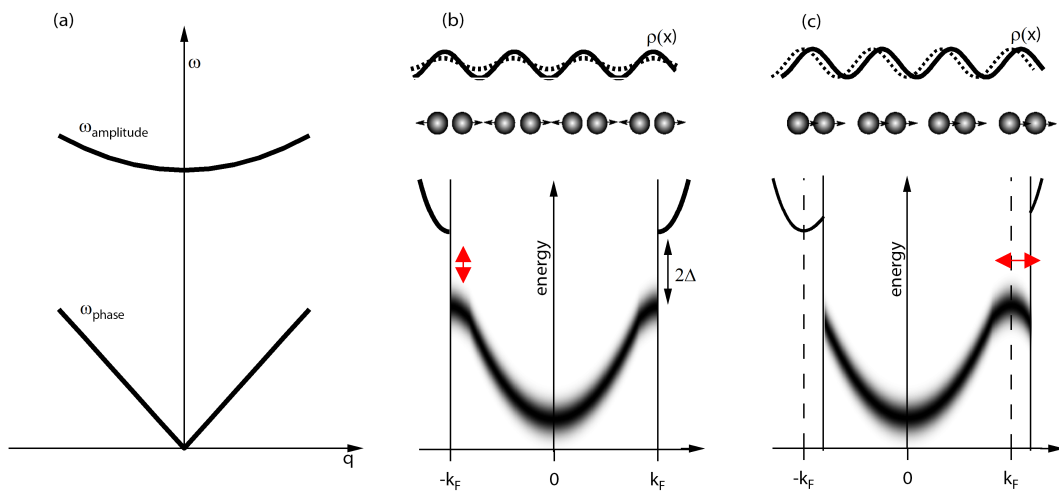
Figure 1.7 | Amplitude and phase excitations of the charge density wave ground state. Dispersion of the amplitude and phase mode close to q = 0 (a). Charge density, ion displacement and band structure changes associated with an amplitudon (b) and a phason (c).

2 Light-Induced Dynamics

Light can couple to all infrared (IR)-active modes including phonons and electronic excitations. The pump photons couple to the electrons producing interband transitions or intraband absorption, thereby increasing the electronic temperature or alternatively dressing the electronic states.

2.1 Two-Temperature Model

During an off-resonant interaction with light the electronic systems becomes hot without affecting the lattice, because the ions are too massive to directly follow the oscillations of the light field. The electron-phonon coupling usually dominates the energy dissipation of hot electrons. The energy transfer from the electronic system into the lattice usually takes between hundreds of femtosecond to several picoseconds. The process is exemplify in Fig. 2.1.
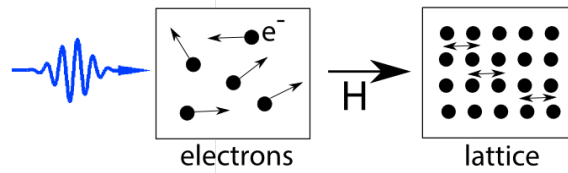
Figure 2.1 | Two-temperature model. Light pulse couples to electronic bath that transfers the energy into a phonon bath

To explain the relaxation process we can use the so-called two-temperature model, which assumes two individual heat baths for the electronic and phononic subsystems. It is assumed that electron-electron scattering and phonon-phonon scattering are much stronger than electron-phonon coupling leading to thermal distributions for both systems at all times. The temperatures of the electronic and phononic systems are given by the following coupled differential equations[20, 21]:

$$\frac{dT_{el}}{dt} = \frac{1}{C_{el}}\left[\frac{\partial}{\partial z}\left(\kappa\frac{\partial}{\partial z}T_{el}\right) - H(T_{el}, T_{ph}) + S\right] \tag{2.1}$$

$$\frac{dT_{ph}}{dt} = \frac{1}{C_{ph}}H(T_{el}, T_{ph}) \tag{2.2}$$

where C_{el} and C_{ph} are the heat capacities, κ is the heat diffusion of the electrons, S is the absorption of the light pulse and H is the energy transfer from the electronic to the phononic systems. To solve the two-temperature model numerically the following approximations can be made. The electronic

heat capacity C_{el} is taken to be proportional to the electronic temperature.

$$C_{el} = \gamma T_{el}. \tag{2.3}$$

The energy transfer rate H is given by the sum over all elementary one-photon absorption and emission processes, weighted by the energy transfer per collision. The transfer rate can be symplified [22, 23] by setting it proportional to the temperature difference between the electronic and phononic systems with g as the electron-phonon coupling constant.

$$H(T_{el}, T_{ph}) = g(T_{el} - T_{ph}) \tag{2.4}$$

The electronic temperature is homogeneous and the diffusive transport is small compared to the laser pulse. Therefore, the first term in equation 2.2 can be ignored. With the previous aproximation we obtain the following equations.

$$\frac{\mathrm{d}T_{el}}{\mathrm{d}t} = \frac{1}{\gamma T_{el}}\big(-g(T_{el} - T_{ph}) + S(t)\big) \tag{2.5}$$

$$\frac{\mathrm{d}T_{ph}}{\mathrm{d}t} = \frac{1}{C_{ph}}g(T_{el} - T_{ph}) \tag{2.6}$$

A numerical solution to equations 2.5 and 2.6 for the electronic and phononic temperatures is shown in Fig. 2.2. In the solution we clearly see a fast rise in the electronic temperature due to the light pulse
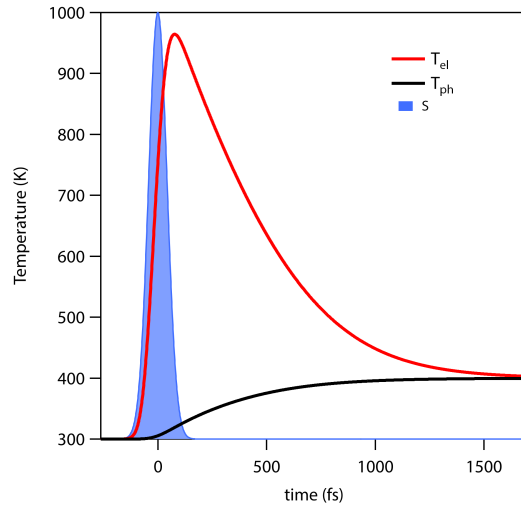
Figure 2.2 | Two-temperature model solution. Electronic and phononic temperature as a function of time with the following constants $g = 3 \times 10^{17}$ Wm^{-3}K^{-1} , $C_{ph} = 9.9 \times 10^5$ Jm^{-3}K^{-1} , $\gamma = 2 \times 10^2$ Jm^{-3}K^{-2} with an initial temperature of 300 K and a Gaussian laser pulse with FWHM = 200 fs.

followed by a slower cooling processes mediated by the electron-phonon coupling which increases the phononic temperature. The two-temperature model has been succesfully use to explain electron termalization and cooling [20, 24] and in some cases where non-thermal carriers are observed or

others effects take part in the cooling an extended two-temperature model has been used to model experiments [25, 26, 27].

2.2 Generation of Coherent Optical Phonons

A femtosecond laser can also initiate a collective, coherent atomic motion by electron-phonon coupling. The classical equation of motion describing coherent phonons for a small nuclear displacement Q is that of a driven harmonic oscillator.

$$m^* \left[\frac{\partial^2 Q(t)}{\partial t^2} + 2\zeta \frac{\partial Q(t)}{\partial t} + \omega_0^2 Q(t) \right] = \mathcal{F}(t) \tag{2.7}$$

where m^* is the effective lattice mass, ζ the damping, and ω_0 the phonon frequency. Depending on the temporal profile and origin of the force $\mathcal{F}(t)$ [28], three excitation mechanisms are distinguished. A sketch of the different mechanisms is shown in Fig. 2.3 and each process is explained in the following text.
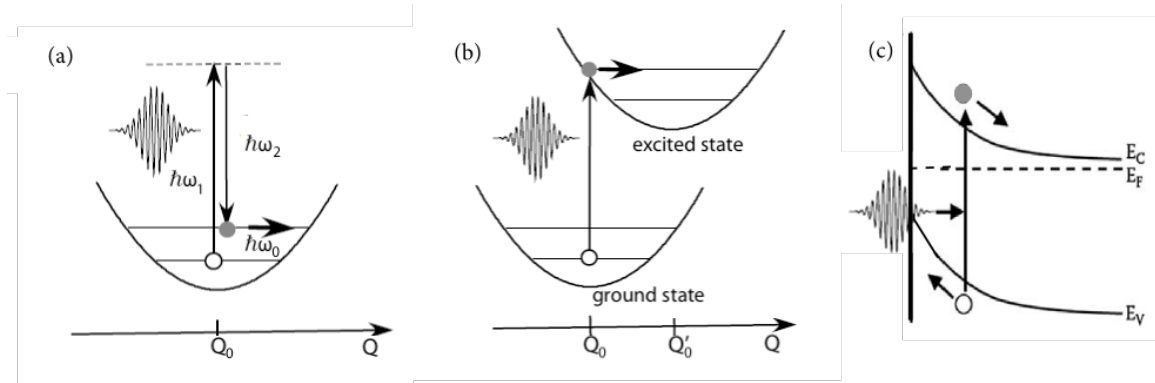
Figure 2.3 | Generation models of coherent optical phonons. (a) Impulsive stimulated Raman scattering (ISRS), (b) displacive excitation of coherent phonons (DECP) and (c) transient depletion field screening adapted from [28].

Impulsive stimulated Raman scattering (ISRS)

A short laser pulse has a broad spectral, i.e. energetic bandwidth that can give multiple combinations of photon pairs such that $\hbar\omega_1 - \hbar\omega_2$ matches $\hbar\omega_0$ and can act as an impulsive driving force to initiate coherent motion on the ground electronic state [29]. This process is schematically shown in Fig. 2.3 (a). The driving force is given by the Raman polarizability [28]. The resulting oscillation will follow a sine function in time. The necessary conditions for impulsive stimulated Raman scattering to occur are that the phonon is Raman-active and that the pulse duration is much shorter than the phonon period.

Displacive Excitation of Coherent Phonons (DECP)

The pulse will change the electron temperature at the Fermi level $\Delta T(f)$ of a metal or produce inter-band transitions in a semiconductor which will generate an electron density $n(t)$ in the conduction band. The excitation leads to a sudden change of the quasi-equilibrium phonon coordinate Q (Fig. 2.3 (b)) giving rise to the coherent motion of the atoms. The atomic displacement depends linearly on $n(t)$ or $\Delta T(f)$ [30]. The oscillation will follow a cosine. Therefore, the force $\mathcal{F}(t)$ can be described as $\mathcal{F}(t) \propto n(t)$. The requirements for DECP are that the electronic excitation can shift the potential energy surface by electron-phonon coupling and that the pulse duration is shorter than the phonon period.

Transient Depletion Field Screening

In polar semiconductors photocarriers can screen the band bending inducing a sudden change of the electric field that causes the ions to move as sketched in Fig. 2.3 (c). The driving force $\mathcal{F}(t)$ can be written as the Raman contribution and the nonlinear longitudinal polarization which includes the drift-diffusion currents generated by the rearrangement of the ions [31].

2.3 Light-Induced Phase Transitions

The behaviour of light-induced phase transition can be studied in terms of the free energy as a function of an order parameter. If there are no IR-active phonons in the material, light couples directly to the electronic system and drives it out of equilibrium without affecting the lattice directly. At equilibrium the system is at a minimum of the free energy surface. For the low symmetry phase the equilibrium position is at $\Delta = \Delta_0$. A sufficiently intense light pulse interacting with a material will change its free energy surface, by changing the depth of the free energy minimum as well as the equilibrium position (Fig. 2.4 (a)). The excitation will take the system from the bottom of the low symmetry energy surface into a position in the modified free energy surface without modifying the order parameter. The system will relax towards to the new equlibrium $\Delta < \Delta_0$ position, leading to a gap size reduction, in a damped motion or start to oscillate around the new minimum. The latter describes amplitude mode oscillations.

For a strong excitation (Fig. 2.4 (b)) the minima at Δ_0 will completely quench, leaving as the only possible equilibrium state the high symmetry phase, i.e. minimum at $\Delta = 0$. The excitation will take the system from the bottom of the ground state energy surface into a position in the modified free energy surface without modifying the order parameter. The system will relax to the new minimum $\Delta = 0$, transforming into the high symmetry phase.

For all excitations, the transient state reached will relax until the ground state is recoverd. The recovery is often accompanied by displacive excitations of coherent phonons.

It has been shown that charge density wave (CDW) and similar symmetry-broken ground states are transiently destroyed with femtosecond laser pulses [6, 5, 7, 32]. The associated band structure

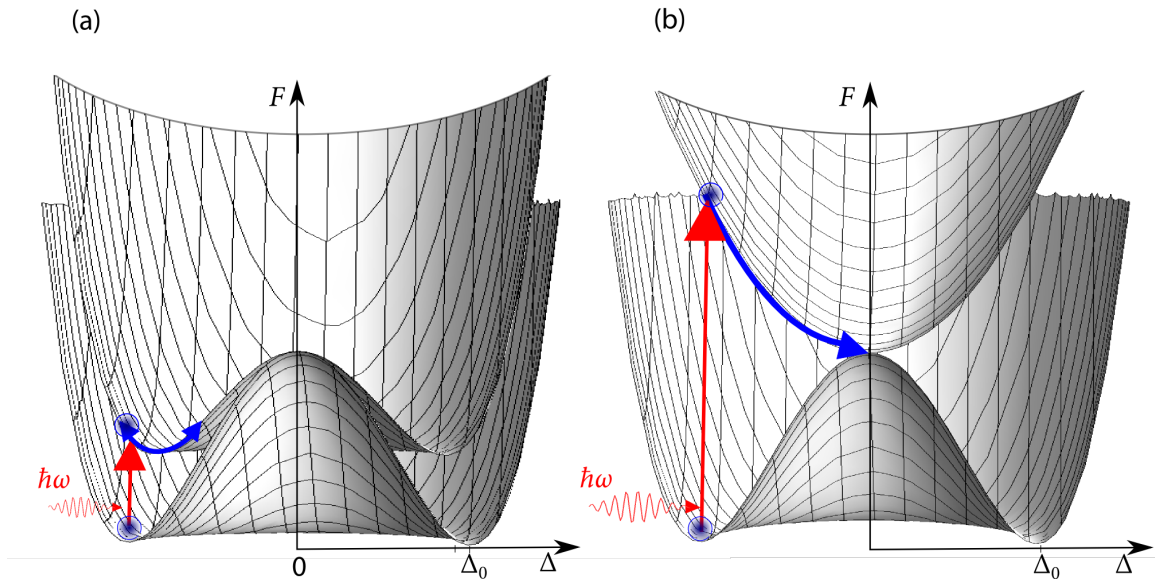**Figure 2.4 | Light-induced phase transitions.** Free energy surface for the ground state and the photo-excited state for (a) weak excitation and (b) strong excitation.

changes and the dynamics can be traced with tr-ARPES [33, 34, 35, 36, 37, 38, 39, 40]. While the melting time is intimately linked to the mechanisms for CDW formation, the timescale for CDW recovery reveals the dominant energy dissipation channels.

3 Time- and Angular-Resolved Photoemission Spectroscopy

Tr-ARPES combines photoemission spectroscopy, giving a direct measurement of the electronic band structure in solids, with a pump-probe scheme adding time information to it. The sample gets photo-excited by the pump and a time-delayed extreme-ultraviolet (XUV) pulse ejects photo-electrons. A hemispherical analyzer disperses the photoelectrons according to their emission angle (in-plane momentum) and kinetic energy (binding energy). In this way snapshots of the electronic band structure along selected lines through the Brillouin zone are obtained on a 2D detector. By changing the optical path length of either the pump or probe a variable delay is introduced such that the system can be probed at different times after the excitation. The first time-resolved photoemission spectroscopy (PES) experiments with picosecond resolution were used to observe unoccupied states and obtain the relaxation times of the excited states [41]. In general, the timescale can give important information about the underlying mechanisms of the excitation and relaxation. For instance, the response of a Peierls insulator to impulsive excitations is between 100 fs to 1 ps [37]. Therefore, to impulsively excite and study the dynamics associated with the light-induced phase transition in a Peierls insulator, femtosecond laser pulses are needed. Following the uncertainty principle a femtosecond laser pulse is required to have a broad spectral bandwidth. The product of the frequency bandwidth ($\Delta\nu$) and temporal full-width at half-maximum (FWHM) (Δt) of a transformed-limited Gaussian pulse is given by

$$\Delta\nu\Delta t \geq \frac{2\ln 2}{\pi}.$$

(3.1)

For instance, such a pulse of 50 fs requires a spectral width of 36 meV, which consequently limits the energy resolution of the tr-ARPES experiment.

The tr-ARPES setup at the Max Planck Institute for the Structure and Dynamics of Matter in Hamburg uses a 12 mJ titanium-sapphire (Ti:Al$_2$O$_3$) amplifier operating at a repetition rate of 1 kHz to generate synchronized pump and probe pulses from the same source. In this chapter a short explanation of the theory of photoemission spectroscopy is discussed followed by a detailed explanation of the tr-ARPES experimental setup.

3.1 Photoemission Spectroscopy

PES is a technique based in the photo-electric effect. The photo-electric effect was first observed by Hertz in 1887 [42] and later, in 1905, explained by Einstein as a result of the quantum nature of light [43]. He explained that a bound electron could increase its kinetic energy and escape into the vacuum by absorbing a quantum of light, nowadays called photon. Following energy conservation, the kinetic energy of the electron is given by

$$\mathcal{E}_{\text{kin}} = \hbar\omega - \Phi - |\mathcal{E}_B| \tag{3.2}$$

where $\mathcal{E}_B$ is the binding energy and Φ is the work function of the material, i.e. the potential barrier that an electron at the Fermi level needs to overcome in order to escape into the vacuum. For most materials Φ is ~ 5 eV [44]. Figure 3.1 (a) shows the relation between the energy levels inside the solid and the electronic distribution produced by photons with energy $\hbar\omega$. The wave vector $\vec{K} = \vec{p}/\hbar$ of
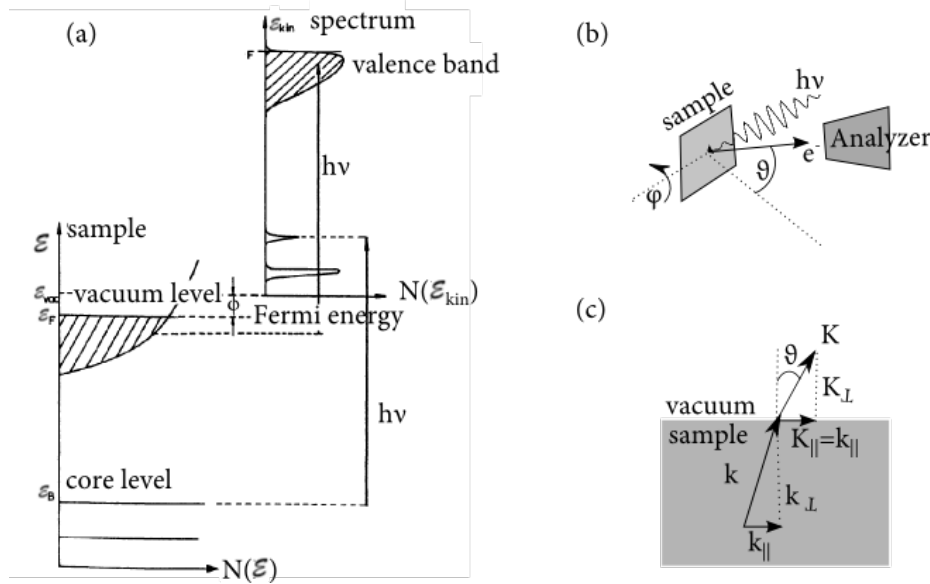
Figure 3.1 | Photoemission process. (a) Energetics of the photoemission process from [45], (b) geometry of the photoemission process and (c) refraction process of the photoelectron at the material-vacuum transition.

the photoelectrons in vacuum is completely determined: its modulus is given by $K = \sqrt{2m\mathcal{E}_{\text{kin}}}/\hbar$ and the components parallel $\vec{K}_{\parallel} = K_x + K_y$ and perpendicular $\vec{K}_{\perp} = K_z$ to the sample surface are given

in terms of the polar (ϑ) and tilt (φ) emission angle shown in Fig. 3.1 (b) by:

$$K_x = \frac{1}{\hbar} \sqrt{2m\mathcal{E}_{\text{kin}}} \sin \vartheta \cos \varphi \tag{3.3a}$$

$$K_y = \frac{1}{\hbar} \sqrt{2m\mathcal{E}_{\text{kin}}} \sin \vartheta \sin \varphi \tag{3.3b}$$

$$K_z = \frac{1}{\hbar} \sqrt{2m\mathcal{E}_{\text{kin}}} \cos \vartheta \tag{3.3c}$$

In the photoemission process the in-plane momentum is conserved. Therefore, the electron's in-plane momentum component $\vec{k}_{\parallel}$ in the crystal is equal to the in-plane momentum component of the photoelectron $\vec{K}_{\parallel}$.

3.1.1 Photoemission Process and the Spectral Function

For a more accurate description of the photoemission process we have to consider the excitation from an initial state ψ_i^N into a final state ψ_f^N by a photon field with vector potential $\vec{A}$ [46]. The photocurrent I is proportional to the transition probability w_{fi} obtained from Fermi´s Golden Rule.

$$I \propto w_{fi} = \frac{2\pi}{\hbar} |\langle \psi_f^N | \mathcal{H}_{int} | \psi_i^N \rangle|^2 \delta(\mathcal{E}_f^N - \mathcal{E}_i^N - \hbar\omega) \tag{3.4}$$

Using the commutator relation $[\vec{p}, \vec{A}] = -i\hbar \vec{\nabla} \cdot \vec{A}$ and the dipole approximation the interaction with the photon can be treated as a perturbation given by the Hamiltonian

$$\mathcal{H}_{int} = -\frac{e}{2mc} (\vec{A} \cdot \vec{p} + \vec{p} \cdot \vec{A}) = -\frac{e}{mc} \vec{A} \cdot \vec{p} \tag{3.5}$$

where $\vec{p}$ is the electronic momentum operator. Here, the gauge $\Phi_A = 0$ was chosen and the quadratic term in $\vec{A}$ was assumed to be negligible with respect to the linear term. In the sudden approximation, i.e. no interactions between the photoelectron and the system left behind, the final states can be rewritten as the state of a photoelectron with momentum $\vec{k}$ and the $(N-1)$ state left from removing an electron $\psi_f^N = \mathcal{S}\phi_f^k \psi_f^{N-1}$ with $\mathcal{S}$ an antisymmetric operator to satisfy the Pauli principle. Assuming that the initial state is a single Slater determinant we can rewrite the initial state in terms of one-orbital wave functions ϕ_n^k and a $(N-1)$ particle term $\psi_i^N = \mathcal{S}\phi_i^k \psi_i^{N-1}$. The matrix elements in equation 3.4 are given by:

$$\langle \psi_f^N | \mathcal{H}_{int} | \psi_i^N \rangle = \langle \phi_f^k | \mathcal{H}_{int} | \phi_i^k \rangle \langle \psi_m^{N-1} | \psi_i^{N-1} \rangle \tag{3.6}$$

where $M_{f,i}^k = \langle \phi_f^k | \mathcal{H}_{int} | \phi_i^k \rangle$ is the one-electron dipole matrix element and the other term $c_{m,i} = \langle \psi_m^{N-1} | \psi_i^{N-1} \rangle$ is the $(N-1)$ overlap integral. The state ψ_f^{N-1} can be chosen from any excited state ψ_m^{N-1}. The total photoemission intensity as a function of momentum k and kinetic energy $\mathcal{E}_{\text{kin}}$ is

given by the sum of all possible transitions from initial to final state.

$$I(k, m\mathcal{E}_{\text{kin}}) = \frac{2\pi}{\hbar} f_{\text{FD}}(\mathcal{E}_{\text{kin}}) \sum_{fi} |M_{fi}^k|^2 \sum_m |c_{m,i}|^2 \delta(\mathcal{E}_{\text{kin}} + \mathcal{E}_m^{N-1} - \mathcal{E}_i^N - \hbar\omega) \tag{3.7}$$

$$= \frac{2\pi}{\hbar} f_{\text{FD}}(\mathcal{E}_{\text{kin}}) \sum_{fi} |M_{fi}^k|^2 \mathcal{A}(k, \mathcal{E}) \tag{3.8}$$

where f_{FD} is the Fermi-Dirac distribution to take into account that photoemission probes only the occupied states and $\mathcal{A}$ is the spectral function for the electrons. In a non-interacting electronic system $|c_{m,i}|^2 = 1$ for just $m = i$, otherwise the spectral function and thus the photoemission intensity will be given by a delta function at the orbital energy $\mathcal{E}_B{}^k = \varepsilon_k$. For strongly correlated systems many elements will be non-zero, making this term more complicated. We can rewrite the spectral function $\mathcal{A}$ in terms of the electron proper self energy $\Sigma(\vec{k}, \omega) = \Sigma'(\vec{k}, \omega) + i\Sigma''(\vec{k}, \omega)$ to separate the single particle contribution from the many-body interactions.

$$\mathcal{A}(\varepsilon, \omega) = -\frac{1}{\pi} \frac{\Sigma''(\vec{k}, \omega)}{[\varepsilon - \varepsilon_k - \Sigma'(\vec{k}, \omega)]^2 + [\Sigma''(\vec{k}, \omega)]^2} \tag{3.9}$$

where ε_k is the single particle dispersion. The real part of the self energy contains the energy renormalization, while the imaginary part describes the lifetime due to many-body effects. Therefore photoemission spectra give access to the single particle dispersion as well as information about many-body interactions.

3.1.2 Angular-Resolved Photoemission Spectroscopy

In an ARPES experiment both the kinetic energy and the emission angle of the photoemitted electrons are determined with a hemispherical analyzer. Once $\mathcal{E}_{\text{kin}}$ and the emission angles (φ, ϑ) are known, $\mathcal{E}_B(k_x, k_y)$ can be obtained by equation 3.2 and equation 3.3. It is worth noticing that the Fermi level of the sample and the analyzer are leveled due to ground connection as shown in Fig. 3.2. Therefore equation 3.2 should be replaced by $\mathcal{E}_{\text{kin}} = \hbar\omega - \phi_A - |\mathcal{E}_B|$ where ϕ_A is the work function of the analyzer. The relation between angle and momentum is given by $k_x[\text{Å}^{-1}] = 0.512\sqrt{\mathcal{E}_{\text{kin}}[\text{eV}]} \sin\vartheta$ from equation 3.3.

We used a hemispherical analyzer (HSA) (PHOIBOS 100 SPECS) for the experiments in this thesis. The analyzer can sort the electrons by their kinetic energy in the radial direction, and image the angular distribution in the azimutal direction. A sketch of the analyzer is shown in Fig. 3.3. The HSA has a mean radius $R_0 = 100\,\text{mm}$. Charged particles entering the the HSA through the entrance slit are deflected in elliptical trajectories by the radial electric field between the inner and outer hemisphere. The resolution or FWHM of the transmitted line $\Delta\mathcal{E}_{\text{an}}$ is given by

$$\Delta\mathcal{E}_{\text{an}} = \frac{S_1}{R_o} \mathcal{E}_p \tag{3.10}$$
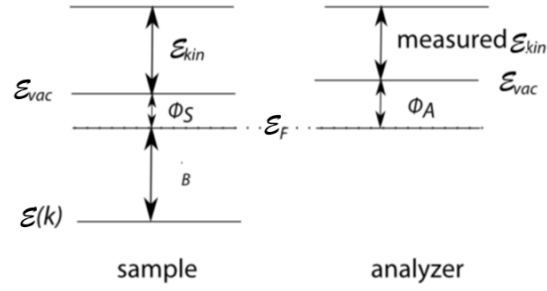
Figure 3.2 | Energy levels. Sketch of the energy levels at sample and analyzer grounded.
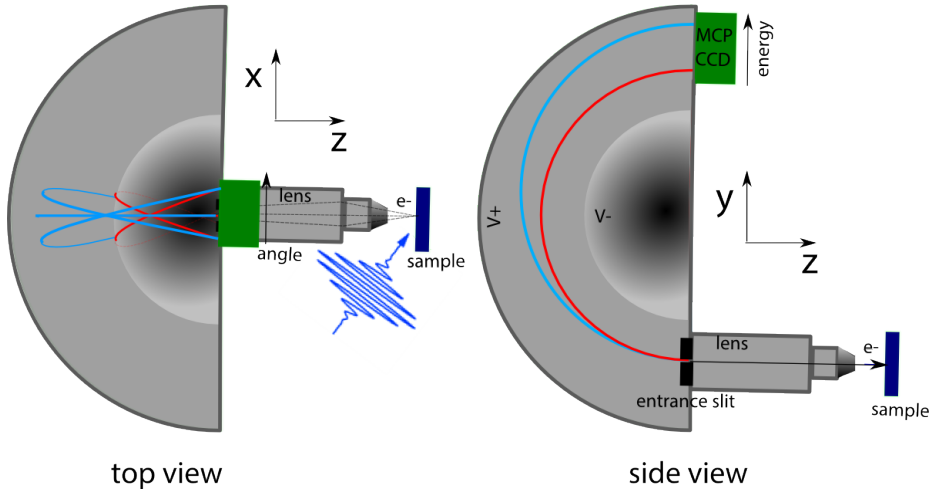
Figure 3.3 | Hemispherical analyzer. Top and side view showing the angular and energy distribution of the photoemitted electrons inside the analyzer

where S_1 is the size of the slit and $\mathcal{E}_p$ the pass energy. For all the experiments in this thesis the wide angle lens mode was used, which gives a 30° angular acceptance window. A pass energy of 10 eV was mostly used resulting in a detected energy range of 2 eV. For the previous settings and an entrance slit of $1 \times 20\,\text{mm}^2$ the best energy resolution that can be achieved is $\Delta\mathcal{E}_{\text{an}} = 100\,\text{meV}$ for a monochromatic light source. There are additional contributions to the observed energy resolution, for instance the natural width of the radiation used for excitation $\Delta\mathcal{E}_{\text{ph}}$. Assuming Gaussian lines for all the contributions, the total resolution will be given by the convolution of all of them:

$$\Delta\mathcal{E}_{\text{tot}} = \sqrt{\Delta\mathcal{E}_{\text{an}}^2 + \Delta\mathcal{E}_{\text{ph}}^2} \tag{3.11}$$

3.2 Experimental Setup

The setup is based on the commercial $Ti:Al_2O_3$ amplifier system, Coherent Legend Elite Duo which delivers 12 mJ femtosecond pulses at a repetition rate of 1 kHz. In the system, the pulses from a $Ti:Al_2O_3$ oscillator are stretched, and amplified in two steps based on the chirped pulse amplification (CPA) scheme invented by Mourou and Strickland [47], where the so-called seed pulse from the oscillator is first stretched in time to a few ps duration, then amplified, before it is compressed again. Here, the first amplification stage is a regenerative cavity, where a single pulse from the mode-locked train of pulses is confined by polarization until the desired amplification is reached. The second stage is a single-pass amplifier. The output is separated in two branches, where one (probe) is used to generate XUV by high-harmonic generation (HHG) , while the other (pump) is either directly used to excite the sample or used to generate light at longer wavelength by optical parametric amplification (OPA) to pump the system. Each branch has a separate compressor to compensate for the different optical elements in each path and to optimize the pulse duration independently for HHG and for OPA. To characterize the femtosecond pulses from the amplifier we used a second-harmonic generation (SHG) frequency-resolved optical gating (FROG). This technique was developed by Trebino [48] and consist in spatially overlapping two previously divided beams of the laser in a nonlinear crystal, that will generate light at the sum of the individual optical frequencies. The spectrum of the sum-frequency generated by the two beams is measured as a function of temporal delay by changing the path difference between the beams, resulting in a trace as the one shown in Fig. 3.4 (a). By using iterative algorithms the original electric field can be retrieved from this measured trace, often referred to as spectrogram. The FROG trace was measured for the HHG arm after the compressor, giving a pulse duration of 50 fs at FWHM and a spectral bandwidth of 24 nm (47 meV) with a central wavelength of 790 nm (1.57 eV). The retrieved intensity of the electric field as well as the spectrum are shown in Fig. 3.4 (c) and (d).
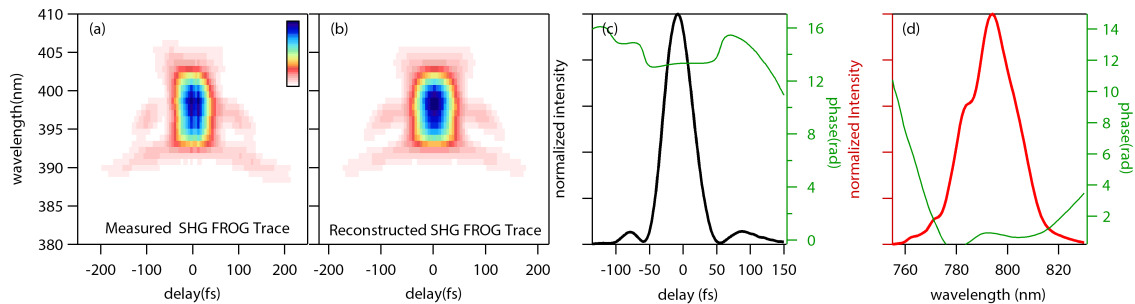
Figure 3.4 | Amplifier pulse characterization. (a) FROG trace of the fundamental laser at the low power branch, (b) reconstructed FROG trace, retrieved electric field (c) and spectrum (d).

In Fig. 3.5 a sketch of the complete setup is shown with its two optical branches after the laser amplifier. One branch is responsible for generating and focusing a XUV pulse that will be used as a probe for the photoemission process. The other branch seeds an OPA device followed by a difference-frequency generation (DFG) stage to generate mid-infrared (MIR) light to excite the sample, while

it is also possible to use the light directly at its fundamental wavelength (path not shown)
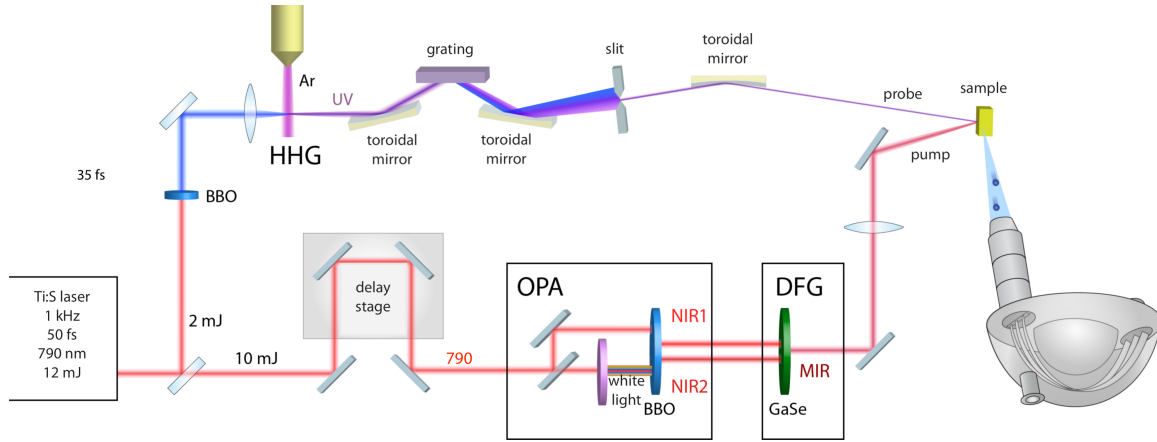
Figure 3.5 | Tr-ARPES setup. Sketch of the Ti:Al$_2$O$_3$ amplifier based tr-ARPES setup. Courtesy of J. Harms.

3.2.1 Extreme-Ultraviolet Generation

To achieve photoemission from a solid, photons with energies higher than the work function of the material in question are required. The average work function of materials is around 5 eV [44]. There-fore a photon energy of $\hbar\omega > 5$ eV is sufficient to enable photoemission. This, in principle, can be realized by consecutively doubling the frequency of the fundamental Ti:Al$_2$O$_3$ laser in two β-Barium Borate (BBO) crystals, achieving $\hbar\omega > 6.2$ eV. This approach is used in many tr-ARPES measurement schemes [49], where the research focuses on the center of the Brillouin zone. For photon energies $\hbar\omega = 6.2$ eV the maximum in-plane momentum that can be reached at an emission angle of $\vartheta = 90°$ is limited to $k_{\parallel} = 0.512\sqrt{\hbar\omega - \phi} \sim 0.5\,\text{Å}^{-1}$. In Fig. 3.6 the photoemission angle as a function of photon energy is plotted for photo-electrons at the Fermi level for different values of k_x. For crys-tals with a small unit cell, the first Brillouin zone can easily extend beyond $0.5\,\text{Å}^{-1}$. In the case of In/Si(111) $- (4 \times 1)$, the X point is located at $k_x = 0.8\,\text{Å}^{-1}$. To reach the X point of the indium wires and cover all interesting features in the band structure with tr-ARPES we need probe photon energies above 10 eV.

To obtain higher photon energies in the extreme ultraviolet region the high-harmonic generation (HHG) was employed. The basic principle of HHG can be explained within the three step model [50], sketched in Fig. 3.7 (a). First, an intense femtosecond laser pulse is focused into an inert gas jet, being Argon in our setup. The laser field changes the potential of the Argon atoms making the electrons to tunnel out of the potential barrier, but as the oscillating laser field changes direction, the electrons are accelerated back to their parent ion until they re-collide, emitting high energy photons. Not every ionized atom's electron finds its parent ion making this prosseces highly ineffecnt. The efficiency is proprtional to λ^{-6} [51]. During each half cycle of the fundamental pulse an XUV burst will be emitted as shown in Fig. 3.7 (b). In first approximation each XUV burst will have a continuous spectrum up to a cut off energy given by $E_{\max} \sim I_p + 3U_p$ [54], where I_p is the ionization potential
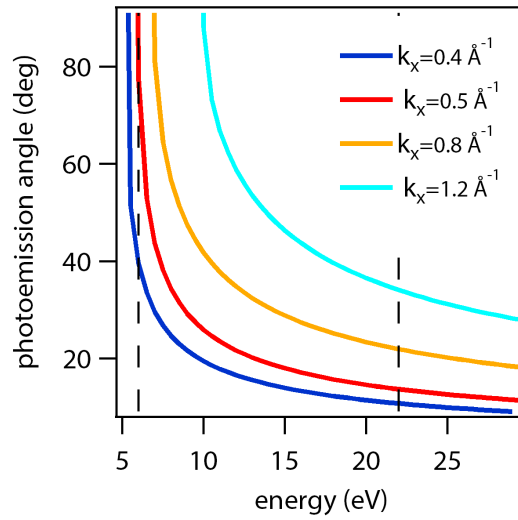
Figure 3.6 | Photoemission momentum range. Photoemission angle vs photon energy for four different momenta with $k_x = 0.8 \, \text{Å}^{-1}$ corresponding to the X point of In/Si(111)-(4×1). Dashed lines correspond to photon energies 6.2 eV and 22 eV.

and U_p is the ponderomotive energy of the ionization potential. The ponderomotive energy is given by $U_p = \frac{I}{4\omega^2}$, were I and ω are the driving laser field's intensity and frequency. For longer drive laser wavelength, higher photon energies can be reached. However, the process efficiency will be lower for longer wavelegths because it is proportional to λ^{-6}. Each pulse has many cycles, making the driving field periodic in time, consequently the energy spectrum will be periodic in frequency, composed by odd harmonics of the driving field. For the experiments described in this thesis two slightly different HHG setups were used. In the first case, the fundamental $\lambda = 790 \, \text{nm}$ (1.57 eV) beam of the Ti:Al$_2$O$_3$ amplifier was directly used to drive the HHG process, while in in the second case, the second harmonic of the fundamental was used for the generation, by placing a BBO crystal
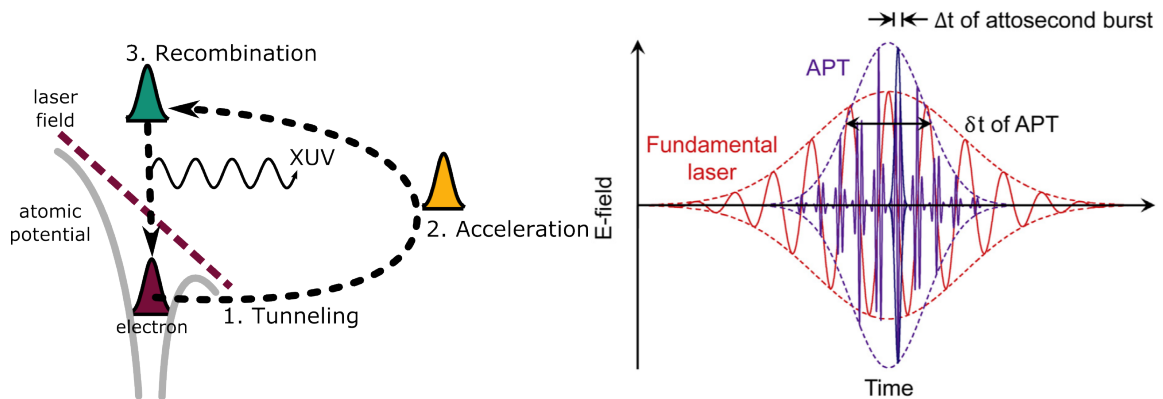
Figure 3.7 | High harmonic generation. Three step model taken from [52] and fundamental and emitted electric field during the high harmonic generation process taken from [53].

before the focusing optics. In both cases the beam was focused into the Argon jet. The corresponding pulse energy was 1 mJ (λ = 790 nm) and 100 μJ (λ = 395 nm). The intensity of the harmonics in the measured XUV spectrum (see Fig. 3.8 (a)) generated by λ = 395 nm is significantly higher than the XUV generated from λ = 790 nm for harmonics up to $\hbar\omega$ = 22 eV, but as expected higher energy harmonics are reached with λ = 790 nm compared to λ = 395 nm.
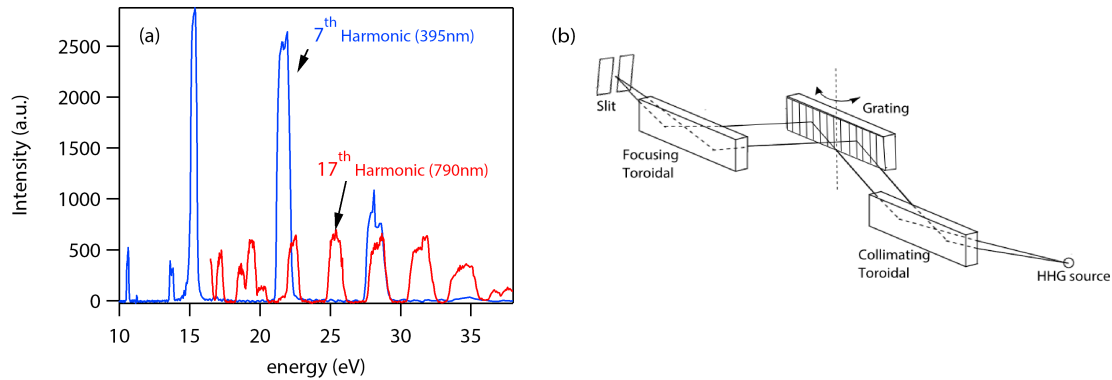
Figure 3.8 | XUV spectrum and monochromator configuration. Measured XUV spectrum (a) and monochromator sketch (b) adapted from [55].

To select a single harmonic from the complete spectrum, a grating monochromator similar to [55] was implemented. In contrast to the time-preserving monochromator described in [55] a design using a grating in the classical diffraction geometry at grazing incidence was preferred to achieve high energy resolution. The grating is used in the external diffraction order, i.e. $\alpha < \beta$, where α and β are the incidence and diffraction angles. The use of the external diffraction order has the advantage of a minimum temporal broadening for a given subtended angle, since the number of illuminated grooves is proportional to $1/\cos(\alpha)$ and, therefore is decreasing for lower α. The configuration is shown in Fig 3.8 (b) consisting of two toroidal mirrors that collimate and refocus the incoming light into a slit with a grating in between the two mirrors. In the setup used for this thesis, three different gratings can be used depending on the desired energy and time resolutions for the experiment. The monochromator is operated without an entrance slit, since the HHG source has a small size of ~ 50 μm. The calculated time and energy resolution for different gratings are shown in Fig. 3.9 assuming a 50 μm source and a 100 μm exit slit.

For the experiments we used the 17th harmonic of 1.57 eV ($\hbar\omega_{probe}$ = 26.7 eV) and the 7th harmonic of 3.14 eV at $\hbar\omega_{probe}$ = 22 eV shown in Fig. 3.8 (a). The spectrum was obtained by turning the grating and measuring the photo-current in a channeltron just before the analysis chamber. A channeltron is a channel electron multiplier that can directly detect and amplify energetic photons and charged particles. For all time-resolved experiments the 120 gr/mm grating was used, which in the 22 – 25 eV range results in a theoretical energy FWHM of 100 meV and a temporal resolution of 100 fs FWHM. However, the best energy resolution obtained in our experiments was 150 meV. In the calculation some other factors as the size of the beam at the sample were not taken into account
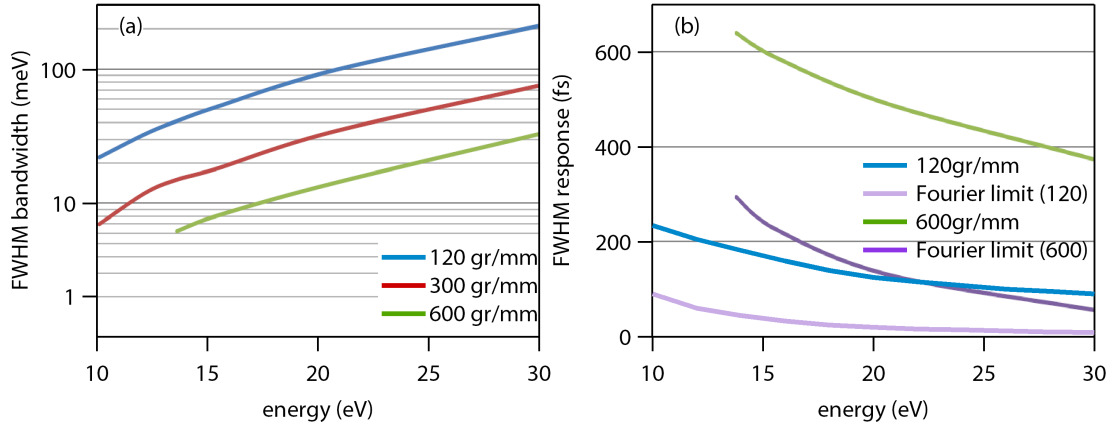
Figure 3.9 | Monochromator theoretical resolution. Calculated energy (a) and time resolution (b) of the beamline's monochromator. In the calculation, an exit slit of 100 μm was taken into account.

and these will affect the energy nad momentum resolution. The chosen harmonic is refocused at the sample position with a toroidal mirror at grazing incidence. For beam diagnostics and spatially overlapping the pump and the probe at the sample position a micro channel plate (MCP) was used. The measured XUV spot size at the sample position was $FWHM_y$ = 300 μm and $FWHM_x$ = 560 μm.

3.2.2 Mid-Infrared Generation

The tr-ARPES setup has the possibility of using light tunable over a broad wavelength range, going from the fundamental 790 nm into the MIR region up to 15 μm as a pump. To generate light in the IR and MIR range a commercial optical parametric amplifier (He-TOPAS) followed by a DFG stage was used.

Optical Parametric Amplification

OPA is a non-linear effect, where a signal (*s*) beam can be amplified in a non-linear material in the presence of a pump (*p*) beam. Each photon of the pump is converted into a signal and idler (*i*) photon following energy conservation:

$$\omega_p = \omega_i + \omega_s \tag{3.12}$$

where ω_p, ω_i and ω_s are the frequencies of the pump, idler and signal beams, respectively. The He-TOPAS can generate two near-infrared (NIR) pulses tunable from λ_{signal} = 1200 nm to λ_{signal} = 1590 nm and λ_{idler} = 1590 nm to λ_{idler} = 1896 nm. For this purpose 10 mJ of the $Ti:Al_2O_3$ amplifier were used. The He-TOPAS consist of three amplification stages. The input is separated into four beams, one with a small fraction of the input energy (about 1 − 3 μJ) to generate the seed for the optical amplification process. This low energy beam is tightly focused into a sapphire plate where

self-phase modulation leads to broadening of the spectrum and to the generation of a white light continuum. The three other beams act as pumps in each consecutive stage. Each amplification stage consist of a type-II BBO crystal in a rotational mount, where the pump and signal are spatially and temporally overlapped. As the white light continuum is chirped, it is possible in the first stage to choose the wavelength that interacts with the pump by adjusting the delay between the two beams. To effectively amplify a certain wavelength the crystal angle needs to be set properly to achieve phase matching for the desired wavelength.

For the experiments discussed in chapter 6 the signal at a photon energy of $\hbar\omega = 1$ eV ($\lambda_{signal} = 1240$ nm) was directly used as a pump. In this case, the signal beam was focused with a $f = 1.5$ m lens and sent inside the vacuum chamber through a fused silica window and steered to the sample. A representative spectrum of the signal beam is shown in Fig. 3.10, and exhibits a central wavelength of 1247 nm with a bandwidth (FWHM) of $\Delta\lambda = 44$ nm. If we assume that the pulse is Fourier-limited and has a Gaussian shape the minimum pulse duration (FWHM) would be $\Delta t = 51$ fs. The two-dimensional beam profile was measured with a Spiricon Pyrocam from Ophir and fitted with a Gaussian function to obtain the FWHM, resulting in a beam size at the sample position of 0.8 mm.
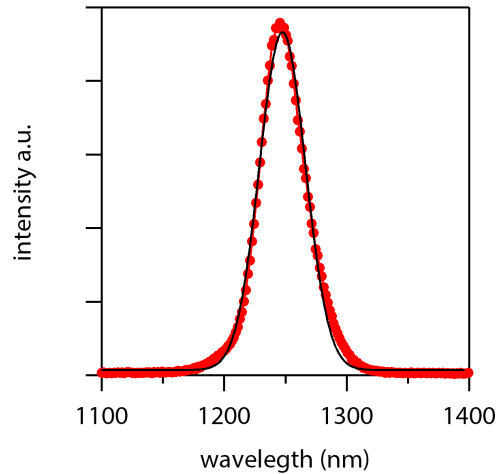
Figure 3.10 | TOPAS spectrum. Measured spectrum from He-TOPAS output (signal).

Difference Frequency Generation

To generate even longer wavelengths it is necessary to exploit another nonlinear effect, DFG, where two photons generate one photon following

$$\omega_{DFG} = \omega_s - \omega_i. \tag{3.13}$$

For this, the He-TOPAS output beams were temporally and spatially overlapped in a GaSe crystal. The central wavelength of the generated beam can be calculated from equation 3.13. However, due to the broad bandwidth of the pulses it is possible to generate light at longer or shorter wavelength if the

corresponding phase matching condition is fulfilled. To ensure that light at the desired wavelength is generated a Fourier-transform interferometer (FTIR) spectrometer was used. In this, light is sent into a Michelson interferometer and the intensity of the interferogram is measured as a function of difference path length. The obtained trace as well as the Fourier-transform of the trace is shown in Fig. 3.11, which yields a central frequency of 46 THz (6.5 μm) and a bandwidth of 5 THz (0.7 μm). Assuming a Gaussian transform-limited pulse the pulse duration would be 88 fs. Depending on the desired wavelength and bandwidth, the signal and the idler beams were blocked with a long pass filter (Spectrogon LP–4860) that transmits light with wavelengths above 4.86 μm, or with a band pass filter (Spectrogon BP–4450 – 200) that transmit light at a central wavelength of 4.45 μm and a bandwidth of 0.2 μm. The MIR beam was then focused with a ZnSe or CaF lens onto the sample position. The two-dimensional beam profile was also measured with the Spiricon Pyrocam. The typical beam size was 1 mm with slight variations.

Figure 3.11 | FTIR signal. Recorded FTIR signal in the time (a) and frequency (b) domain. Data points obtained from the fast-fourier-transform of data in (a) and gaussian fit

3.3 Effects Commonly Present in Tr-ARPES

Some effects arising from electron-photon and electron-electron interactions of the photoemitted electron can be present in the tr-ARPES measurements affecting the energy, momentum and time resolution of the measurements. In the next sections the most common effects relevant in our measurements are briefly explained.
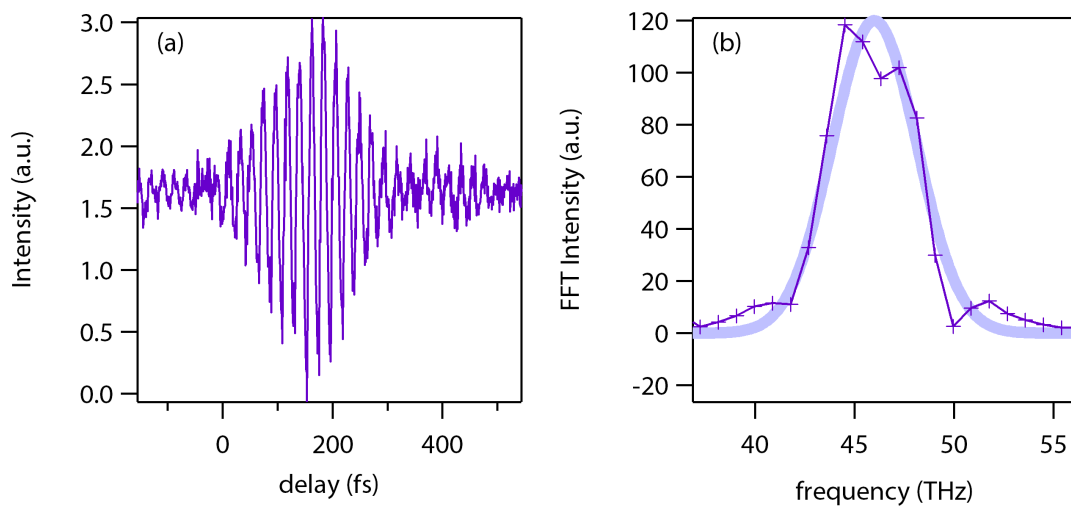
3.3.1 Photon Dressed States

The coherent interaction between electrons and strong laser fields such as the employed pump pulses results in the formation of photon dressed states. The interaction of light with Bloch states, i.e. with the bound electron in the initial state before photoemission, gives rise to Floquet-Bloch states and the interaction of light with free-electron final states at the surface leads to Volkov states or laser assisted photoemission (LAPE). In both cases the interaction of the electrons with the time periodic potential of the pump pulse generates side bands of the original band structure separated by multiples of the driving photon energy. Figure 3.12 shows a sketch of the photoemission processes under different conditions. First for the unperturbed case, giving an electronic transition from bound states to free-electron like states. The next three panels consider the photoemission transition under the influence of a periodic driving field. In one case the periodic potential dresses the bound states, in the next it dresses the free-electron states, and finally, in the last panel, it dresses both the initial and final states generating a mixture of Floquet/Volkov states. The intensity of Floquet and Volkov sidebands depends on the polarization of the driving field and they have different dependence on polarization. Therefore, by changing the polarization of the driving field these two effects can be disentangled [56]. The intensity of LAPE first order sidebands is given by

$$I_1 \propto I_0 (\vec{k} \cdot \vec{E})^2 \lambda_{\text{pump}}^4 \tag{3.14}$$

where $\vec{k}$ is the momentum of the photoelectrons and $\vec{E}$ is the electric field vector of the pump pulse. Thus, LAPE will be particularly strong if $\vec{k} \parallel \vec{E}$ and absent for $\vec{k} \perp \vec{E}$. In one dimensional solids Floquet-Bloch states can only be formed if the polarization of the pump pulse is parallel to the system.

3.3.2 Space Charge

The use of ultrashort pump and probe pulses with high peak intensity can generate so-called vacuum space charge effects caused by the Coulomb interaction between the photoemitted electrons. Space charge can broaden the measured spectrum up to a point that the band structure becomes invisible, and consequently the intensity of both pump and probe should be set to a value where no broadening is visible.
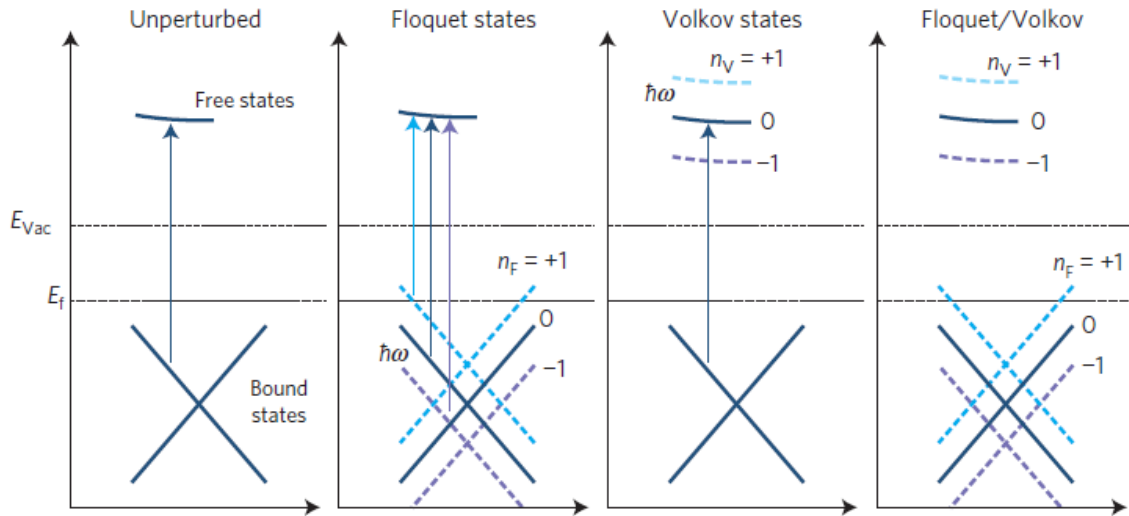
Figure 3.12 | Photon dressed states. Sketch of different photoemission transitions from a solid driven by a periodic electric field. Taken from [56].

Probe-Induced Space Charge

Electrons in a cloud travelling in vacuum will repel each other due to mutual Coulomb interactions. If the cloud is very dense the interaction will alter its energy and spatial spread. If the XUV probe beam is too intense the cloud of photoelectrons will be very dense and it thus will alter the measurement. In addition to the broadening of the spectrum, an overall shift of the spectrum to higher energies will be observed.

Pump-Induced Space Charge

The space charge effects induced by the pump pulse are due to the interaction of two photoelectron clouds. One ejected by the XUV probe pulse and the other by the non-linear emission of electrons by the intense pump pulse. The effect can be described by the interaction of the probe electrons with a mean electric field of the pump electrons [57]. The results are band broadening and energy shift of the bands. The up-shift and broadening increases with increasing fluence. The effects are also depending on delay, at negative time delays the photoelectrons cloud from the pump will add a positive energy shift to the photoemission spectra. When the probe electrons cross the pump electrons cloud there will be a reduction in energy shift, afterwards, as time delay increases the effect will become weaker.

4 In/Si(111)-4X1

The In/Si $(111)-(4\times1)$ structure is one example of a real quasi-1D system, that allows us to investigate the physics of 1D systems. The system undergoes a metal-to-insulator transition at low temperatures accompanied by a doubling of its periodicity along both directions resulting in a In/Si $(111)-(8\times2)$ reconstruction. In Fig. 4.1 the theoretical atomic [9] and electronic [58] structures of the In/Si $(111)-(4\times1)$ and the In/Si $(111)-(8\times2)$ phases are shown.
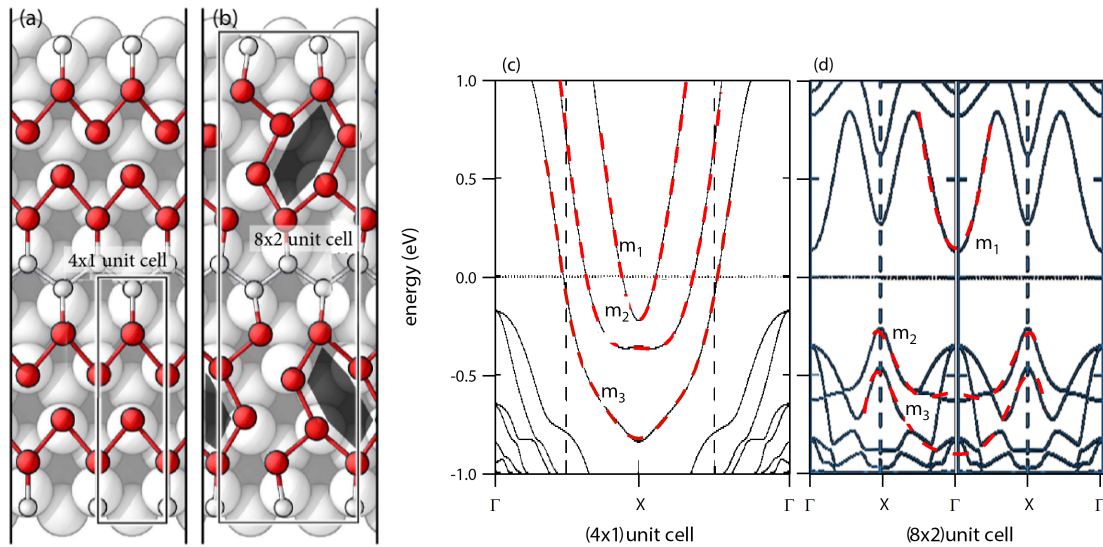
Figure 4.1 | Atomic and electronic structure of (4×1) and (8×2) phases. (a)-(b)Sketch of the indium and silicon atoms at the surface taken from [9] and (c)-(d) DFT calculation from [58] with bands crossing Fermi level labeled as m_1, m_2 and m_3.

The indium wires can be grown in-situ with domain sizes much bigger than 1 mm^2 which makes them suitable to be investigate with ARPES. Self-assembly of indium atoms on silicon can form different 2D reconstructions depending on the amount of indium at the surface [59, 60]. For a coverage of approximately one monolayer (ML) the (4×1) reconstruction is formed. The (4×1) surface reconstruction was first observed with low-energy electron diffraction (LEED) in [59] together with seven other different 2D reconstructions. Some of these reconstructions are shown in Fig. 4.2. The 1D character of this surface was first observed by scanning tunneling microscopy (STM) measurements [61], rapidly followed by different approaches involved in the understanding of the atomic and electronic structure [62, 63, 64, 65]. In 1999, it was found by Yeom [66] that at low temperatures the system undergoes a metal-to-insulator transition, making it particularly interesting. The phase transition was
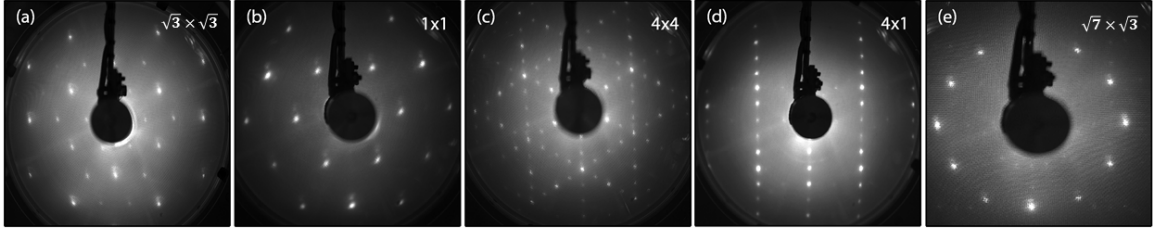
Figure 4.2 | Surface reconstructions of In on Si(111) measured with LEED. (a) ($\sqrt{3} \times \sqrt{3}$) taken with an electron beam energy of 99 eV, (b) (1×1) taken with an electron beam energy of 50 eV, (c) (4×4) pattern resulting from the coexistence of three (4×1) domains with an angle of 120° between them, taken with an electron beam energy of 80 eV, (d) (4×1) taken with an electron beam energy of 77 eV and (e) ($\sqrt{7} \times \sqrt{3}$) taken with an electron beam energy of 82 eV.

initially explained as a Peierls instability. Subsequently other mechanisms such as an order-disorder transition[67], an exothermic reaction with bond breaking [58] and many-body interactions [68] have been proposed. In addition, the question whether the phase transition is first [10] or second order [69, 70] had been controversial. The extensive work based on different models and techniques contributes to understand this system, its phase transition and the responsible mechanism.

In the next sections the metallic and insulating phase as well as the mechanism that leads to the phase transition will be discussed. The explanation below is a summary of the current understanding of this intriguing system. To illustrate the electronic structure static laser-based ARPES measurements will be shown.

4.1 Metallic Phase

The accepted atomic model for the (4×1) reconstruction was proposed by Bunk [65] based on X-ray diffraction measurements, which are in good agreement with LEED [71, 59] and STM [61] measurements.

The indium atoms form pairs of zig-zag chains separated by a chain of silicon atoms resulting in a (4×1) unit cell. In Fig. 4.1 (a) a sketch of the real space structure is shown, where the unit cell is marked. The lattice constant in the direction parallel to the the wires is $a_0 = 3.84$ Å [61, 65, 66, 72].

The dispersion parallel to the zig-zag chains (k_x) in the $\Gamma-X$ direction consists of three parabolic bands centered at the X point. The bands cross the Fermi level at 0.54 Å^{-1} (m_2), 0.75 Å^{-1} (m_1) and 1.2 Å^{-1} (m_3) [73], corresponding to a band filling of 0.11 (m_1), 0.38 (m_2) and 0.5 (m_3) [73, 64]. The m_1 and m_2 bands originate mostly from p_z orbitals of the In atoms. The m_3 band is made from Si-In bonds [73].

The measured dispersion along the wires is shown in Fig. 4.3 for three different k_y values, as marked in Fig. 4.4, revealing the presence of three parabolic bands. The dotted lines in Fig. 4.3 represent the calculated band structure using DFT from [58] shown in Fig 4.1 (c). The photocurrent is strongly modulated by the photoemission matrix element, which makes just part of the band structure visible [74].
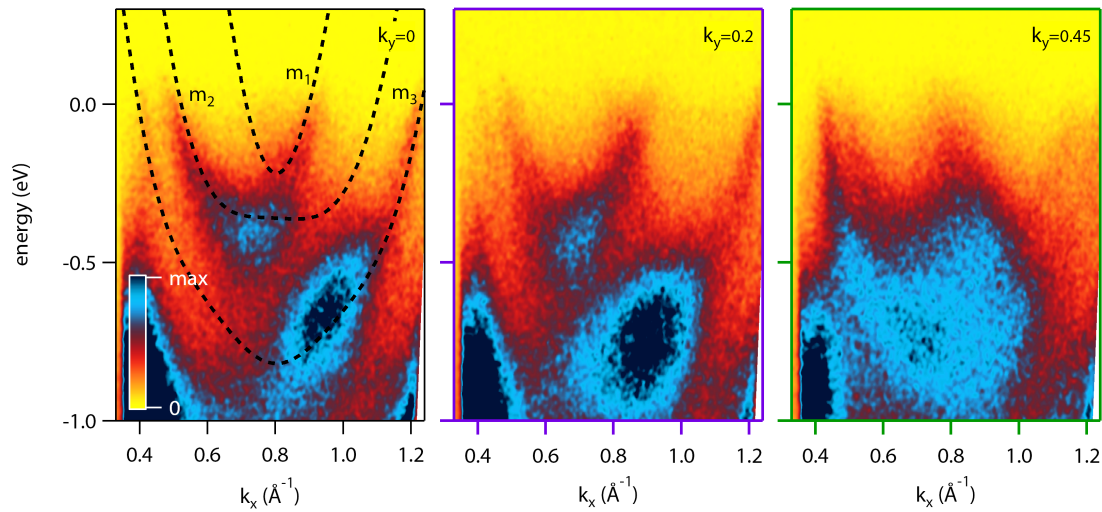
Figure 4.3 | Metallic band structure. Static photoemission current as a function of energy and momentum for the three different k_y cuts marked in Fig. 4.4 parallel to Γ-X direction centered at X. Measured with XUV pulses at $\hbar\omega$ =22 eV using the high energy resolution grating with a groove density of 600 gr/mm.

In Fig. 4.4 we can see the photoemission current as a function of both in-plane momenta for a constant energy at the Fermi level. Here we can see wiggled lines along k_y in the direction perpendicular to the wires. Along k_y the bands have almost no dispersion indicating the quasi-1D character with a weak coupling in the direction perpendicular to the wires. On top of the photoemission current in Fig. 4.4 sinusoidal curves that follow the Fermi surface as well as a sketch of the Brillouin zone boundaries for the (4×1) unit cell and for the (1×1) underlying hexagonal silicon lattice are drawn.
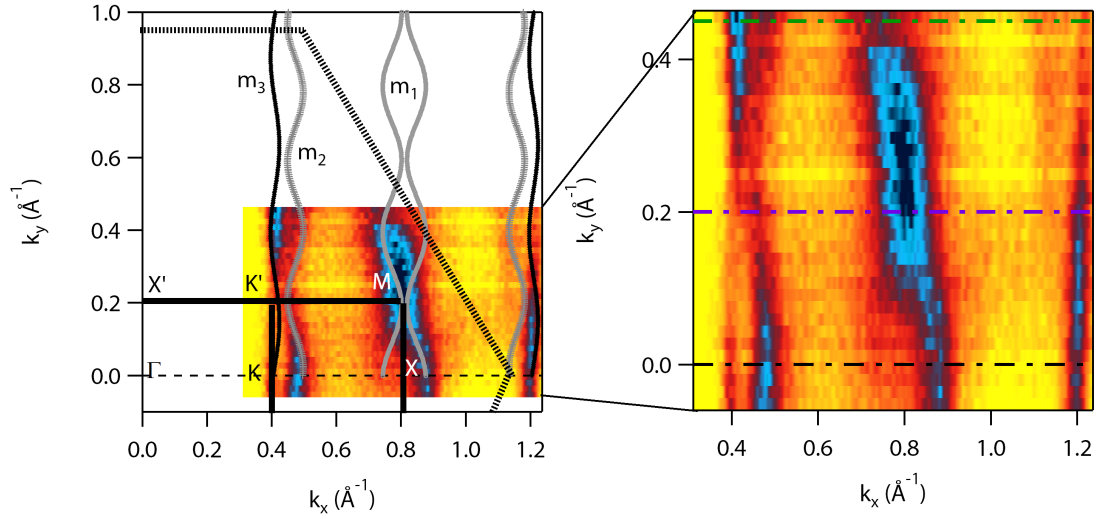
Figure 4.4 | Fermi surface. Static photoemission current as a function of k_x and k_y at the Fermi energy together with sketch of Brillouin zones and sinusoidal curves that illustrate the shape of the Fermi surface, measured with XUV pulses at $\hbar\omega$ =22 eV using the high energy resolution grating with a groove density of 600 gr/mm.

4.2 Equilibrium Phase Transition

At low temperatures the system undergoes a metal-to-insulator transition forming a CDW ground state [73, 75, 66, 72]. The mechanism of the CDW formation involves a multi-band Peierls transition and a charge transfer. Below a critical temperature of around 120 K, the outer indium atoms dimerize resulting in a doubling of the unit cell in the direction of the wires and a subsequent gap opening of the half-filled band m_3. Furthermore the inner indium atoms are displaced by a shear distortion, transferring charge from band m_1 to band m_2, leaving m_1 unoccupied and m_2 almost half filled. Due to dimerization m_2 also gaps. The unit cell doubles in both directions generating a (8×2) unit cell. As a result of the combined dimerization and shear distortion the indium atoms form hexagons as shown in Fig. 4.1. The structure of the low temperature phase was also calculated from X-ray diffraction measurements [76]. The metal-to-insulator transition is accompanied by the softening of two phonon modes, a shear distortion and a rotary mode [69, 9]. The two modes are sketched in Fig. 4.5 (a) and (b). and Fig. 4.5 (c) shows the rotary mode of the hexagonal structure that together with the corresponding shear distortion of the (8×2) symmetry (0.54 THz) drives the inverse insulator-to metal transition [9]. These modes have been identified in Raman spectroscopy measurements [8].

The photoemission spectrum of the low symmetry phase is shown in Fig. 4.6 (b). At low temperatures m_1 is located high above the Fermi level. Therefore, just two bands are visible. m_2 and m_3 gapped at the X point of the (8×2) unit cell. Reported values for the size of the band gap range from 150 meV [75, 77] to 300 meV [78, 79, 58].

In Fig. 4.6 (a) and (b) we show the measured photoemission spectra above and below the transition temperature. Both spectra were measured under the same experimental conditions in the $\Gamma-X$
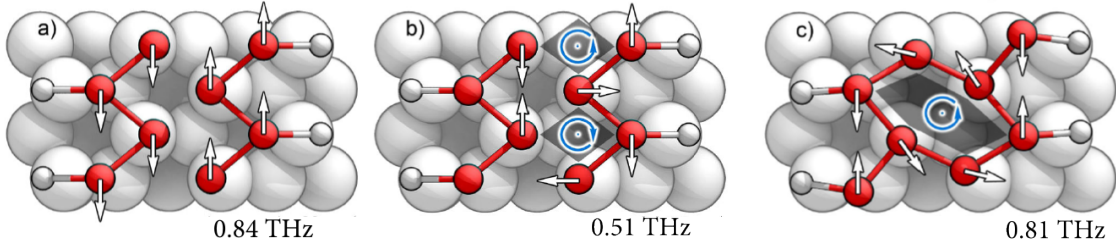
Figure 4.5 | Surface phonons responsible for the structural transition. (a) Shear distortion of the (4×1) phase, (b) rotary mode of the (4×1) phase and (c) hexagonal rotary mode of the (8×2) phase. Taken from [9].
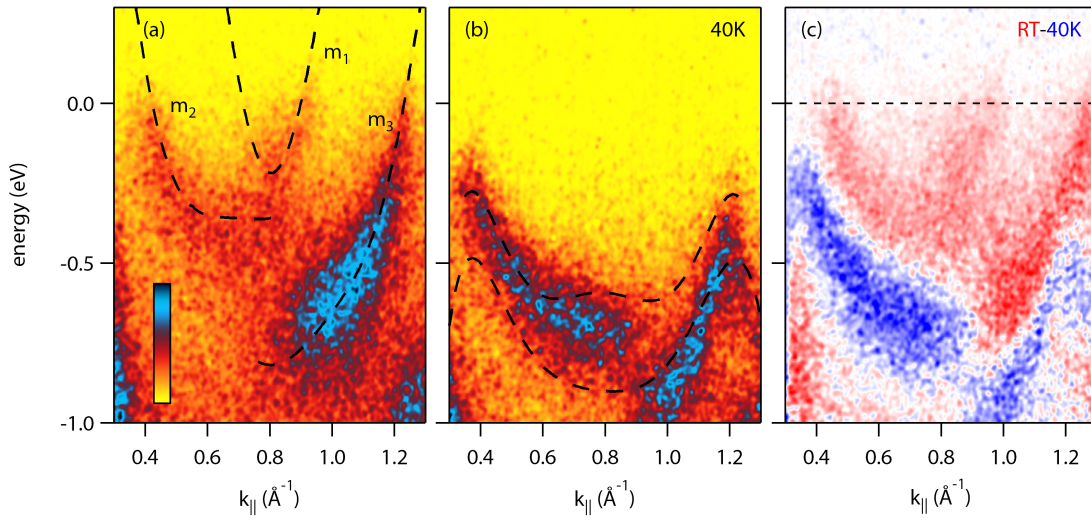
Figure 4.6 | Equilibrium phase transition. Photoemission spectrum centered at the X point of the (4×1) unit cell in the Γ-X direction above (a) and below (b) the transition temperature and difference plot between the two phases (c), measured with XUV pulses at $\hbar\omega$ =22 eV using the grating with a groove density of 120 gr/mm.

direction around the X point ($k_x = 0.81\text{Å}^{-1}$). In comparison with Fig. 4.3 the resolution is lower because for these measurements the monochromator with 120 gr/mm grating instead of the 600 gr/mm was used and the integration time was two times lower. In panel (c) the changes in the band structure resulting from the equilibrium phase transition are shown by subtracting the photocurrent in panel (b) from the photocurrent in panel (a). The difference spectra gives us an idea of the changes we would expect during a light-induced phase transition from the insulator to the metallic phase.

In Fig. 4.7 the potential energy surface as a function of a generalized phonon coordinate Q is sketched following [10]. For $T \gg T_c$ the potential energy surface is a parabola with a minimum at $Q = 0$. For $Q = 0$ the system is ordered in zig-zag chains corresponding to the (4 × 1) phase. At $T \ll T_c$ the surface exhibits two minima, a true equilibrium state at $Q \neq 0$, that corresponds to the (8 × 2) phase with hexagonal ordering, and one at $Q = 0$, that corresponds to a metastable (4 × 1)
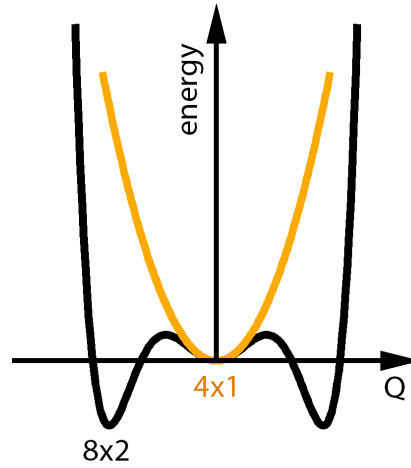
Figure 4.7 | Potential energy surface. Sketch of the PES as a function of a generalized transition coordinate for In/Si(111) at $T < T_c$ and $T > T_c$.

phase. The equilibrium phase transition present hysteresis with a width of W_H = 10 K [80], making it a first order phase transition as explained in [81]. In terms of the potential energy surface hysteresis can be explained by the existence of two minima close to the transition temperature separated by a potential barrier. In some cases below the transition temperature the minimum at $Q = 0$ disappears, leaving only one equilibrium state possible for the system, but for the indium wires the minimum at $Q = 0$ remains even at $T = 0$ K. Therefore, at $T < T_c$ the system can be found in the (4×1) phase if the potential barrier is overcome. According to atomistic thermodynamics calculations presented in [9] the free energy difference between the two stable phases at $T = 0$ K is 6 meV per indium atom and the difference becomes zero at the transition temperature T_c = 125 K .

4.3 Sample Preparation

The samples were prepared on polished phosphorous-doped Si(111) wafers from CrysTec based on the procedures described in [61, 63, 64]. Two different wafers (A and B) were used. Wafer A has a resistivity below 0.01 Ωcm and a 1.5° miscut along the $[\bar{1}\bar{1}2]$ direction and wafer B has a resistivity between $1-20$ Ωcm and a 1° miscut along the $[\bar{1}\bar{1}2]$ direction. In the STM measurements by Nogami et al. [61], rows of (4×1) in three possible directions were visible on different terraces due to the threefold symmetry of the underlying Si. The simultaneous three possible (4×1) orientations on different domains results in a (4×4) LEED pattern, unsuitable for ARPES. Close to the crystal edges, reconstructions would show a preferred direction, therefore using Si(111) wafers with a small miscut angle in the $[\bar{1}\bar{1}2]$ direction ensures the growth in one single orientation [63].

The wafers were first annealed to 1100 °C by direct current heating (DCH) until the pressure in the chamber stayed below 1×10^{-9} mbar and then cooled down slowly to 850°C. In order to obtain regular steps of mono atomic height on the (7×7) surface, the substrate was flashed to 1260°C, and slowly cooled down to 1060°C followed by a fast temperature decrease to 850°C [82]. This proce-

dure was repeated until the pressure stayed below 3×10^{-9} mbar during the 1260°C flash. For the indium deposition an electron beam evaporator was used. The deposition rate was measured with a quartz micro-balance. Around 10 MLs of indium were deposited on the clean substrate at room temperature. The (4×1) surface needs an indium coverage between 0.4 and 1 ML [60]. To get the right amount of indium after deposition various post annealing cycles at different temperatures were made. Each cycle consist on keeping the sample for 5 min at a certain temperature, quickly cooling down and monitored the structure with LEED. Fig. 4.2 shows the LEED patterns obtained for different annealing temperatures as listed in table 4.1.

Table 4.1 | Annealing temperatures after indium deposition. Observed In/Si(111) reconstruction with the experimental annealing temperature to achieve each one.

Reconstruction	$(\sqrt{3} \times \sqrt{3})$	(1×1)	(4×1)	(4×4)	$(\sqrt{7} \times \sqrt{3})$
Annealing Temperature	600 °C	540 °C	500 °C	500 °C	480 °C
In coverage [83]	< 0.2 ML	0.8-1.2 ML	0.7-1 ML	0.7-1 ML	1.2-2 ML

To obtain the right LEED pattern belonging to the (4×1) phase (see Fig. 4.8) it was necessary to postanneal wafer A at 500°C and wafer B at 400°C. To avoid having regions with different reconstructions, it was very important to ensure a homogeneous temperature ($\Delta T_{max} \pm 100°$ C) across the wafer during all the annealing steps. The temperature at the wafer was measured with a pyrometer. After preparation the samples were kept in vacuum with a pressure better than 5×10^{-10} mbar and
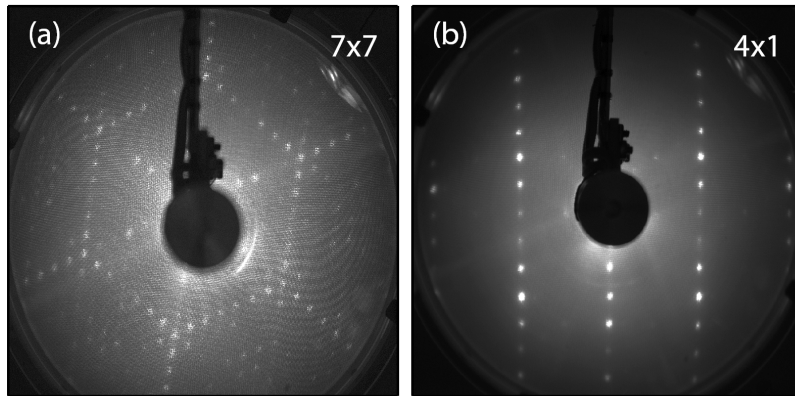
Figure 4.8 | Surface reconstruction of Si(111) and In/Si(111). LEED images for: (a) clean Silicon (7×7) reconstruction and (b) In/Si(111)-(4×1) taken at 58 eV and 77 eV, respectively.

during measurement the pressure in the chamber was below 2×10^{-9} mbar. Even though the samples were kept in ultra high vacuum (UHV) all the time, the surface was found to degrade over time with

dramatic effects on the ARPES spectra (Fig. 4.9). After approximately five hours the bands crossing the Fermi level showed already a considerable broadening. After about ten hours the band structure almost completely disappeared, as shown in Fig. 4.9.
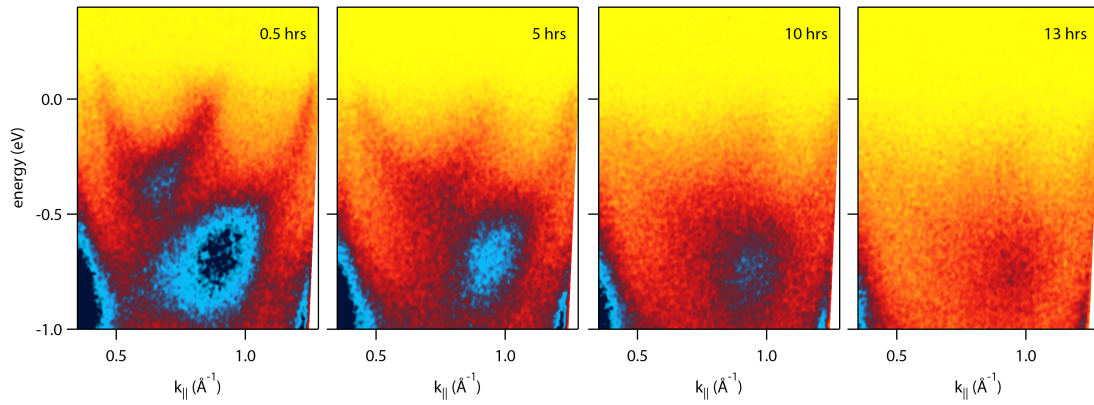
Figure 4.9 | Sample degradation. Measured equilibrium photoemission current for In/Si(111)-(4×1) in Γ-X direction at different times after preparation.

5 Carrier Dynamics in the Metallic Phase

Some of the results in this chapter have been published in: *M. Chávez-Cervantes, R. Krause, S. Aeschlimann, and I. Gierz. Band structure dynamics in indium wires*, Phys. Rev. B, **97**, 201401 (2018) [12] and *M. Chávez-Cervantes, G. E. Topp, S. Aeschlimann, R. Krause, S. A. Sato, M. A. Sentef, and I. Gierz. Charge density wave melting in one-dimensional wires with femtosecond sub-gap excitation*, Phys. Rev. Lett., **123**, 036405 (2019) [13].

The almost free electrons in the metallic phase of $In/Si(111) - (4 \times 1)$ absorb energy from the pump electric field and thereby increase their temperature. The electrons will most likely cool down by transferring the energy to the lattice. In this chapter we will investigate the carrier dynamics after photo-excitation of the $In/Si(111) - (4 \times 1)$ surface at room temperature.

5.1 Hot Carrier Dynamics

As an example of how a hot electron distribution would look like for the $In/Si(111) - (4 \times 1)$ system we simulated ARPES spectra for different electronic temperatures in the $\Gamma - X$ direction centered at the X point of the (4×1) Brillouin zone, which corresponds to $k_{\parallel} = 0.82$ Å. Following section 3.1.1, the ARPES photocurrent is proportional to the spectral function $\mathcal{A}(k, E)$ multiplied by the Fermi-Dirac distribution $f_{FD}(E, T)$ and the photoemission matrix element $|M|^2$. We simulated the spectral function for $In/Si(111) - (4 \times 1)$ by taking the single electron dispersion $\varepsilon_0(k)$ from the DFT calculated bands from [58] shown in Fig. 4.1. The real part of the self energy Σ' was set to zero and the imaginary part $\Sigma'' = 50$ meV was taken as a constant to get a constant bandwidth. $|M|^2$ was taken as a step function for each band that makes visible only one side with respect to the bottom of the corresponding band to match the measured ARPES spectra. Similar photoemission matrix elements were observed in [74]. The simulated ARPES spectra for $T = 300$ K, $T = 900$ K and $T = 1800$ K are shown in Fig. 5.1 (a)-(c). The photocurrent intensity is given by the false color scale shown in panel (a). Panels (d) and (e) were obtained by subtracting (a) from (b) and (c), respectively. They show the difference spectra, highlighting the spectral changes for further comparison with the measured photocurrent.

We investigated the transient distribution of electrons after photo-excitation of the $In/Si(111) - (4 \times 1)$ at room temperature. We measured the photoemission spectra along the $\Gamma - X$ direction centered at the X point of the (4×1) Brillouin zone. We choose to measure in this configuration because it allows us to resolve three Fermi crossings, corresponding to m_2, m_1 and m_3 in the analyzer's momentum window, making it possible to analyze the carrier dynamics for each band independently.
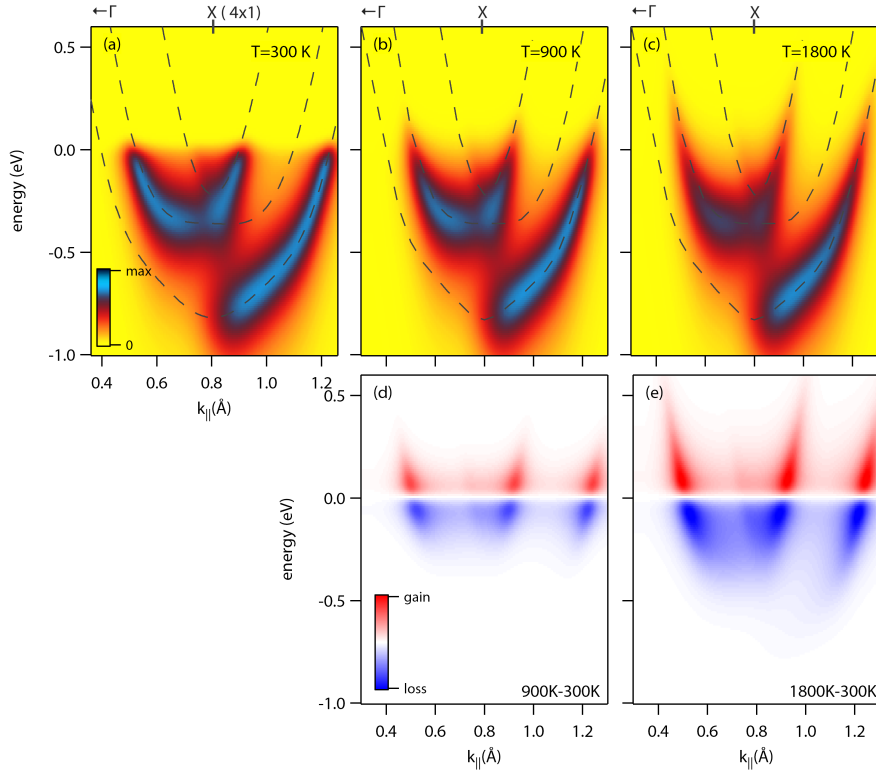
Figure 5.1 | Simulated ARPES spectra. (a)-(c) simulated ARPES spectra for T=300 K, T=900 K and T=1800 K, (d) and (e) difference spectra given by (b)-(a) and (c)-(e), respectively.

In Fig. 5.2 panels (a)-(d) the measured photocurrent for different pump-probe delays after photo-excitation with vertically polarized (V-Pol) pulses with a photon energy of $\hbar\omega$ = 280 meV is shown. In the measurement geometry vertical polarization corresponds to an in-plane polarization perpendicular to the wires. Panel (a) shows the photocurrent at negative time delays and panel (b) corresponds to the maximum excitation. The excited carriers are found to follow the single electron band dispersion. The photocurrent intensity is given by the same false color scale as in Fig. 5.1. Figure 5.2 panels (e)-(g) show the pump-induced changes of the photocurrent, which were obtained by subtracting the data shown in panel (a) from the data shown in panel (b)-(c), respectively. The photo-induced changes in Fig. 5.2 clearly resemble the simulated difference spectra from Fig. 5.1. Furthermore, the occupied states after photo-excitation follow the single electron dispersion for the (4×1) phase, suggesting that the effect of the excitation is solely an increase in the electronic temperature without any underlying changes of the band structure.

To quantify the effect of the pump on the metallic phase, the transient electronic temperature was extracted from the tr-ARPES spectra. We obtained energy distribution curves (EDCs) by integrating the photocurrent over a small momentum window centered at the Fermi momenta k_F corresponding to m_2 and m_3. The EDCs were divided by the density of states, which for a 1D metal is proportional to $1/\sqrt{\mathcal{E}}$. The resulting EDCs were then fitted with a Fermi-Dirac distribution function convoluted
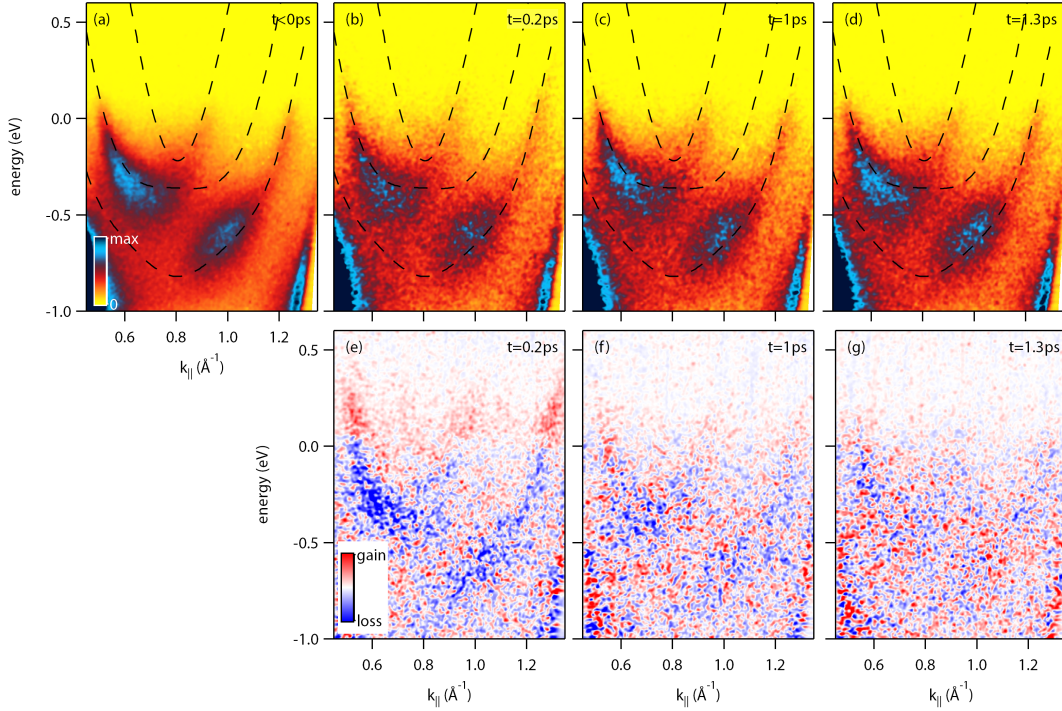
Figure 5.2 | Light-induced hot carrier distribution. (a) Photoemission spectra at negative time delays. (b)-(d) Photoemission spectra for different time delays after photo-excitation with a photon energy of 280 meV and a fluence of 2.2 mJ/cm². Electric field polarization is perpendicular to the wires. (e)-(g) Pump-induced changes of the photocurrent. Dashed lines represent the single electron dispersion.

with a Gaussian function to extract the electronic temperature as a function of pump-probe delay. This fitting function will be referred as Fermi-Dirac distribution fit (FD-fit) throughout this thesis, and is given in appendix D. The Gaussian function accounts for the energy resolution of the setup. Two exemplary EDCs corresponding to m_2 are shown in Fig. 5.3 (b) with the corresponding fits. The temperature extracted from each fit is plotted as a function of delay in Fig. 5.3 (c) for m_2 and m_3. Additionally we also plot the transient electronic temperature extracted from integrated EDCs over the entire momentum window. The peak electronic temperatures reached after photo-excitation were found to be 1150 K for m_2, 1550 K for m_3 and 1330 K for the complete momentum range. We observed that m_3 gets slightly hotter than m_2, but they follow similar dynamics. Due to different orbital content of each band m_3 might absorb more energy from the pump than m_2 . The m_3 band is made of In-Si bonds which are perpendicular to the zig-zag chains, while m_2 is made of p_z orbital. In the previous measurement the pump was parallel to the In-Si bonds, thus m_3 absorbs more energy resulting in a higher electronic temperature. The temporal evolution of the electronic temperature was fitted with an error function multiplied by an exponential decay function convoluted with a Gaussian function. This fitting function will be referred as rise and decay fit (RD-fit), and is also discussed in D. The cooling time for the hot electrons was found to be (0.8 ± 0.1) ps. The electronic temperature follows cooling via phonon emission explained by the two-temperature model (TTM),

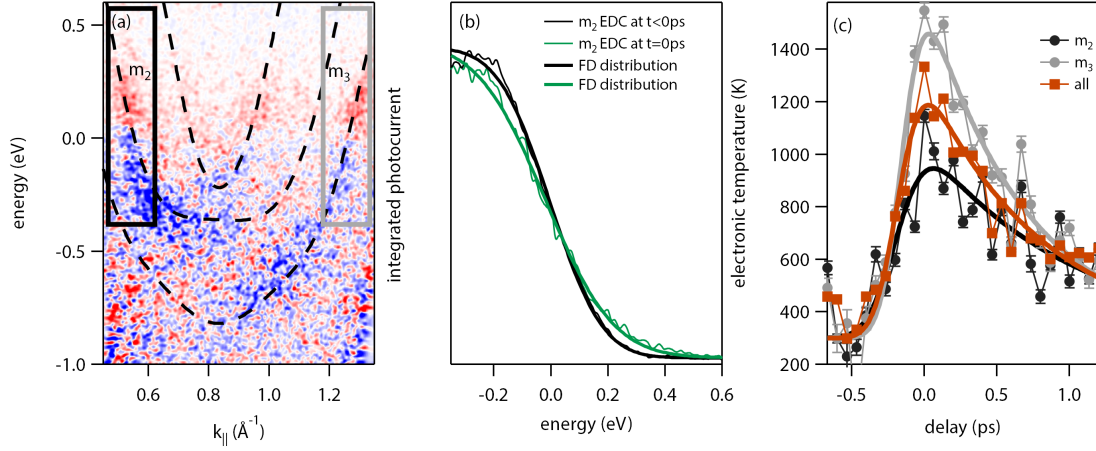**Figure 5.3 | Transient electronic temperature.** (a) Pump-probe signal at peak of excitation (Same as Fig. 5.2 (b)) at a photon energy of 280 meV and fluence 2.2 mJ/cm^2. Regions where photocurrent was integrated to obtain EDCs are marked. (b) EDCs at negative time delays and at peak of excitation for m_2. (c) Electronic temperature as a function of delay extracted from fits to the EDCs at each delay point for m_2, m_3 and the complete momentum window. The error bars show the uncertainty of each fit. Dashed lines represent the single electron dispersion.

discussed in section 2.1. The experimental electronic temperatures fitted with a numerical solution of the two-temperature model are shown in Appendix D.

We investigated the transient electron distribution after photo-excitation under different conditions for different pump photon energies, fluences and polarizations. Appendix D summarizes the fitting parameters for the different data sets. We show the transient electronic temperature after photo-excitation with a photon energy of $\hbar\omega = 170$ meV and $\hbar\omega = 1.57$ eV in Fig. 5.4 (a). The electronic temperature was obtained from the integrated EDCs along the complete momentum window. We found that the electronic system cools down independently of fluence, photon energy or polarization in (0.9 ± 0.2) ps. Figure 5.4 (b) and (c) show the maximum electronic temperature reached as a function of pump fluence and peak electric field. The peak electronic temperature for horizontally polarized pump pulses were taken at $t = 300$ fs to avoid LAPE contributions (see section 5.3). It was found that with increasing fluence the electronic temperature increases and it seems to reach a saturation value. We also found that for the same incident fluence, horizontal polarization (along the wires) resulted in a higher peak electronic temperature for long wavelengths $\lambda > 4500$ nm ($\hbar\omega = 280$ meV). We would expect the same effect for shorter wavelengths, but we didn't investigate thoroughly. The number of excited electrons depends on the energy absorbed by the metal [84]. A quasi-one dimensional metal absorbs energy more efficiently when the polarization of the pump is parallel to the system, resulting in a higher temperature for horizontal polarization (H-pol) in our measurements.
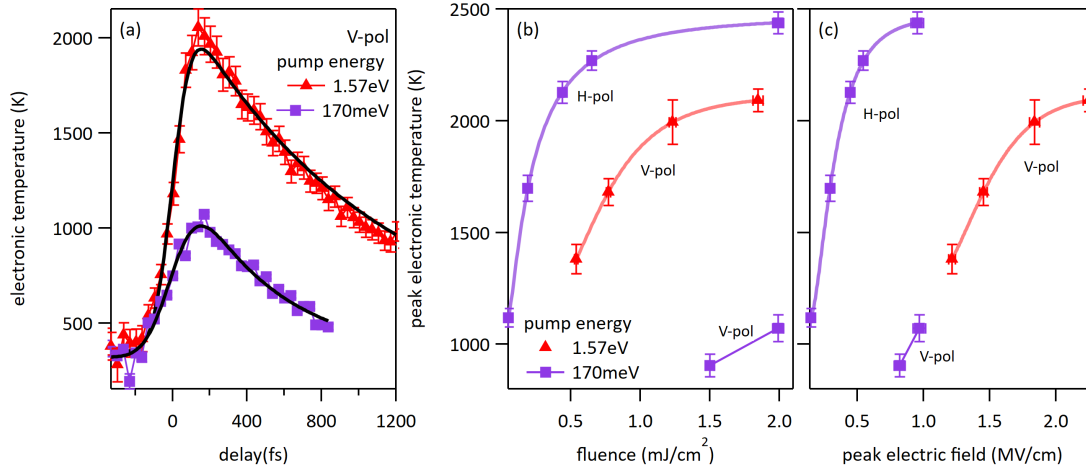
Figure 5.4 | Fluence dependence of the electronic temperature. (a) Extracted electronic temperature after photo-excitation with a photon energy of 170 meV and a fluence of 2 mJ/cm^2, and with a photon energy of 1.57 eV and a fluence of 1.2 mJ/cm^2. (b) peak electronic temperature as a function of fluence. (c) peak electronic temperature as a function of peak electric field.

5.2 Population Dynamics and Coherent Oscillations

Population dynamics reveals many-body interactions without the need of a thermalized carrier distribution. The pump pulse causes a redistribution of the spectral weight by changing the effective interactions at different energies. The energy and fluence dependence of the population lifetime after photoexcitation tracks the effective interactions in the system [85]. To investigate the population dynamics after photo-excitation we integrated the photocurrent inside the boxes marked in Fig. 5.5 (a). The integrated photocurrent as a function of delay was plotted for each box in Fig. 5.5 (b). Each curve represents an energy and was fitted with the RD-fit. From the fits the rise time and decay time were obtained as a function of energy, shown in Fig. 5.5 (c).

We found that the population dynamics show a resolution-limited rise time of approximately 200 fs independent of energy. The rise time of the carrier population in the unoccupied states (above the Fermi level) occurs on the timescale of the pulse duration since photon absorption occurs only while the pump is present. On the contrary, the relaxation time of the carrier population was found to depend on energy. Figure 5.5 (c) shows that the population lifetime increases from (270 ± 50) fs at $E = 0.35$ eV to (0.9 ± 0.1) ps close to the Fermi level. Carriers at higher energies have a bigger phase space, consequently they are more likely to scatter resulting in short lifetimes. Close to the Fermi level almost all states are occupied. Henceforth, the electrons can not move to lower energy states, causing an increased lifetime at the excited state.

Furthermore, we investigated how the relaxation dynamics varies with fluence of the driving pump pulse. In Fig. 5.6 we show the energy dependent relaxation times for three different fluences at photon energy $\hbar\omega = 1.57$ eV. First, we observe that carriers occupy higher energy states in the conduction band with higher fluences, i.e. the curve for the higher fluence used reaches higher energies,
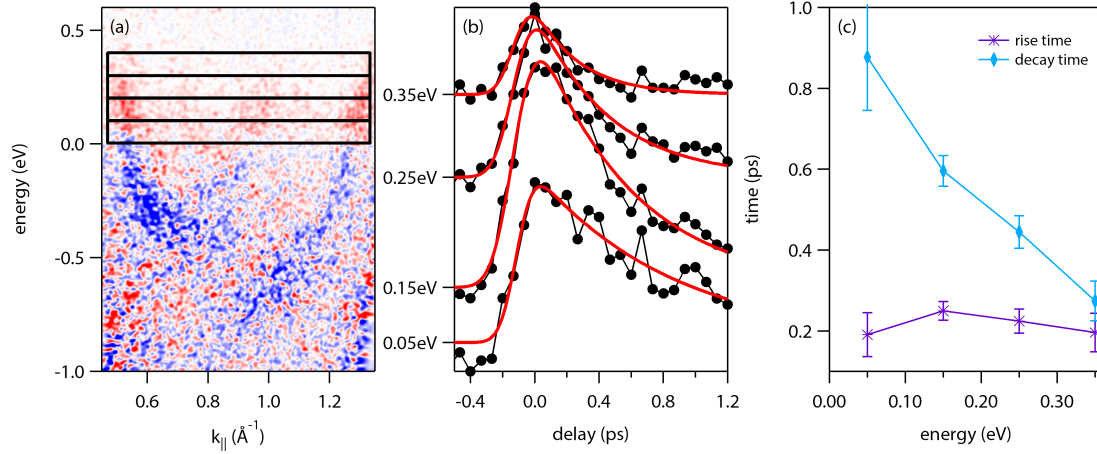
Figure 5.5 | Carrier dynamics after photo-excitation. (a) Pump-probe signal at the peak of photo-excitation with a photon energy of 280 meV and a fluence 2.2 mJ/cm². (b) Integrated spectral weight at different energies marked in (a) as a function of delay. (c) Rise time and relaxation time obtained by fitting the spectral weight curves in (b).

for the other two fluences there was no state ocupied above 0.8 eV. With increasing fluence we observe an overall decrease in the lifetimes more evident close to the Fermi level. The model proposed in [85] for the spectral weight redistribution after photo-excitation predicts longer lifetimes with increasing fluences for energies above the phonon energy coupled to the electronic system. However, we observe the opposite behaviour. We speculate that the discrepancies with the model derive from the difference in dimensionality. The model assumed a 2D system and we have a 1D system. Therefore, the phase space is not the same. We are currently working on calculations of the scattering rates for a 1D metal to explain our observations.
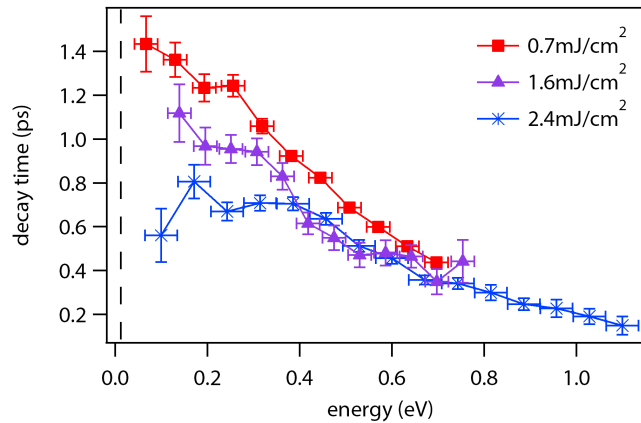
Figure 5.6 | Fluence dependence carrier dynamics. Decay time as a function of energy for different fluences for a pump photon energy of 1.57 eV. Dashed line represents phonon energy.

In addition, we observe coherent oscillations of the photocurrent close to the Fermi level for IR

and MIR excitations. In Fig. 5.7 the integrated spectral weight close to the Fermi level for three data sets is shown. The spectral weight was fitted with the RD-fit. The residual from the RD-fit was fitted with a sinusoidal function to determine the frequency of the oscillations. The frequency of the oscillation was found to be (1.8 ± 0.1) THz. Previous Raman measurements show a peak at the same frequency that was attributed to a phonon that periodically modulates the distance between two neighboring Indium chains [8, 86], as shown in the inset in Fig. 5.7 (c) with a frequency of 2.3 THz. The difference from the experimental and theoretical value for the frequency is because finite temperature effects where not taken into account on the calculations. The oscillations in panel (a) have a phase of $\phi = (1.5 \pm 0.3)$ radians obtained from the sinusoidal fit. This value is almost $\pi/2$ which implies that the oscillations follow a cosine function, showing maximum displacement at $t = 0$ ps when pump and probe pulses overlap suggesting displacive phonon excitation as driving mechanism. The oscillations on panel (b) and (c) have a phase of $\phi = (0.0 \pm 0.1)$ radians obtain by the sinusoidal fit. In case of the MIR-excitation appears to be an impulsive stimulated raman scattering process.
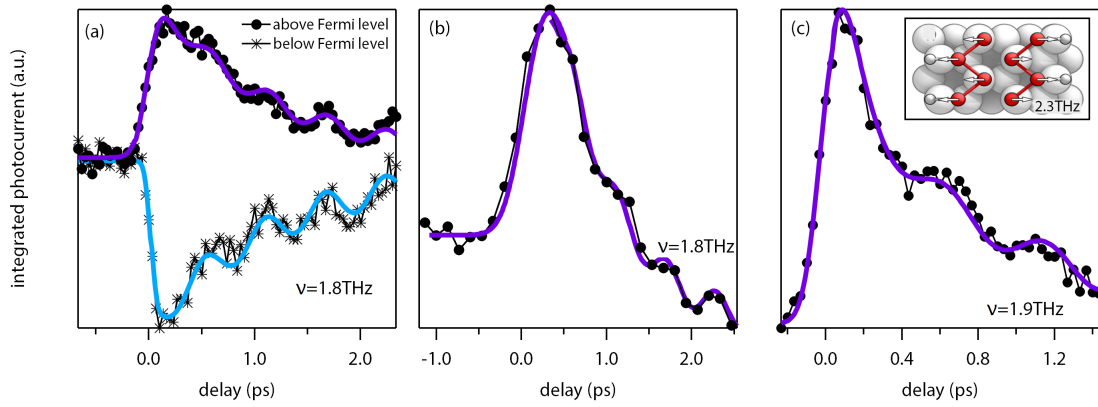
Figure 5.7 | Spectral weight oscillations. (a) Spectral weight below (-0.1 eV) and above (+0.1 eV) the Fermi level for a photo-excitation with a fluence of 1.2 mJ/cm^2 at 1.57 eV. (b) Spectral weight above the Fermi level (+0.1 eV) for a photo-excitation with a fluence of 2.2 mJ/cm^2 at 280 meV (c) Spectral weight above the Fermi level (+0.1 eV) for a photo-excitation with a fluence of 2 mJ/cm^2 at 170 meV and sketch of a the corresponding phonon in the inset [8].

5.3 Laser-Assisted Photoemission (LAPE)

According to Eq. 3.14, the LAPE effect is particularly strong (absent) when the polarization of the pump is parallel (perpendicular) to the direction in which the photoelectrons are detected. In the current experimental setup $\vec{k} \parallel \vec{E}$ for a horizontally polarized pump pulse and $\vec{k} \perp \vec{E}$ for a vertically polarized pump pulse. Therefore, in all our experiments with horizontal polarization of the pump, there is a significant component of the pump field along the direction of the detected photoelectrons which enables the LAPE effect. In addition, according to Eq. 3.14 the intensity of the LAPE sidebands

grows with increasing pump wavelength as λ^4. Therefore, LAPE typically gives a negligible contributions to the pump-probe signal for $\hbar\omega_{\text{pump}} > 1\,\text{eV}$ ($\lambda < 1240\,\text{nm}$) but can dominate the pump-probe signal at MIR wavelengths while the pump is present.

In Fig. 5.8 we provide evidence that the pump-probe signal at $t = 0\,\text{ps}$ for horizontally polarized light with a photon energy of $\hbar\omega = 170\,\text{meV}$ ($\lambda = 7300\,\text{nm}$) can be explained by the formation of sidebands at the photon energy of the pump. Figure 5.8 (a) shows the photocurrent at negative pump-probe delay at room temperature in the metallic phase. Figure 5.8 (b) shows the pump-induced changes of the photocurrent at $t = 0\,\text{ps}$ for different field strengths of $0.16\,\text{MV/cm}$, $0.30\,\text{MV/cm}$ and $0.44\,\text{MV/cm}$ from top to bottom, respectively. In order to simulate the pump-probe signal the measured spectrum at negative delay was shifted up and down in energy by integer multiples of the pump photon energy. The simulated difference spectra are shown in Fig. 5.8 (c). In Fig. 5.8 (d) we compare an EDC extracted from the measured (red) and simulated data (black) spectra to show the excellent quantitative agreement. The experimental data is well reproduced with first order sidebands for a field strength of $0.16\,\text{MV/cm}$, first and second order sidebands for a field strength of $0.30\,\text{MV/cm}$, and first, second, and third order sidebands for a field strength of $0.44\,\text{MV/cm}$.
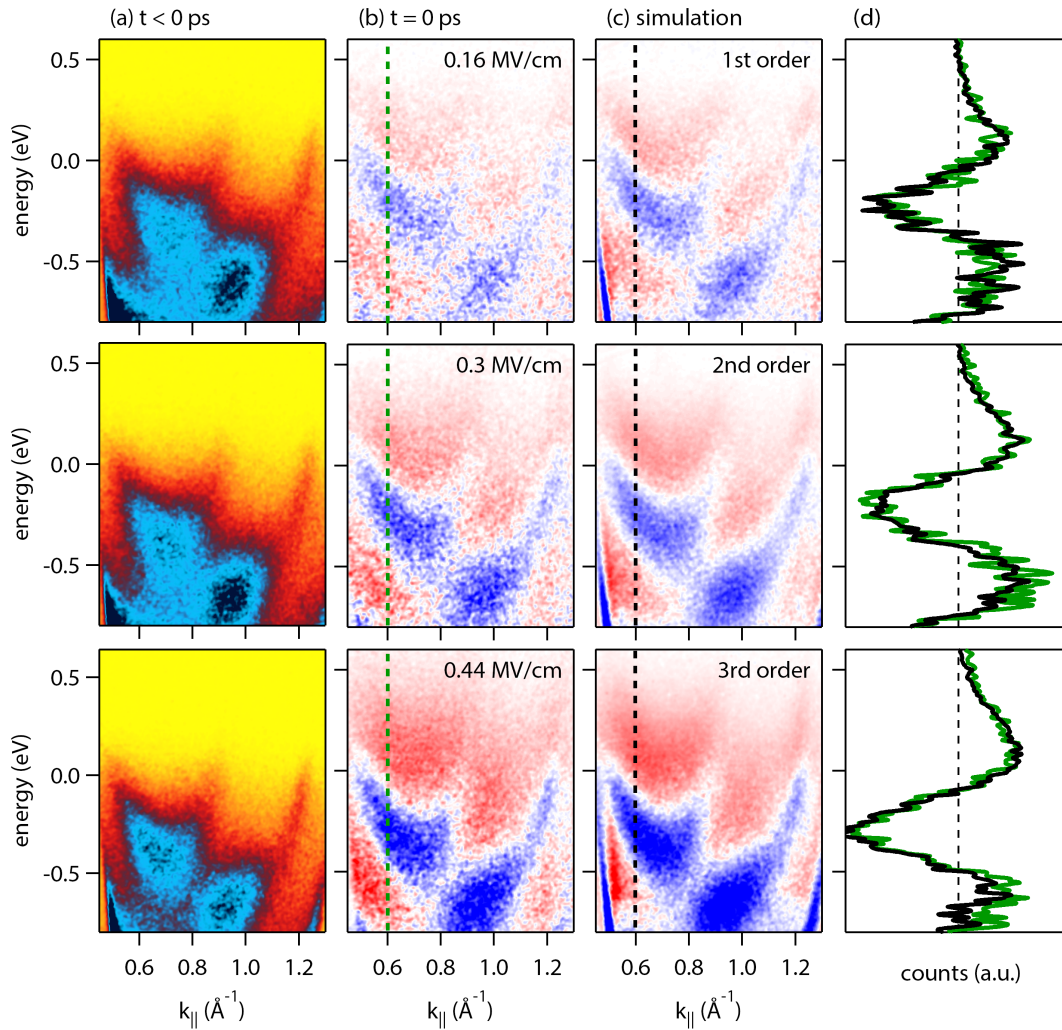
Figure 5.8 | Laser-assisted photoemission. (a) Metallic band structure at negative time delay. (b) Pump-probe signal at t =0 ps with a peak electric field of 0.16 MV/cm (top), 0.30 MV/cm (middle), and 0.44 MV/cm (bottom). (c) simulated pump-probe signal assuming the generation of first order sidebands (top), first and second order sidebands (middle), and first, second, and third order sidebands (bottom). (d) Direct comparison of measured (green) and simulated (black) energy distribution curves extracted along the dashed line in panels (b) and (c).

6 CDW Melting via Single-Photon Absorption: Above-Gap Excitation

Most of the results in this chapter have been published in: *M. Chávez-Cervantes, R. Krause, S. Aeschlimann, and I. Gierz. Band structure dynamics in indium wires*, Phys. Rev. B, **97**, 201401 (2018) [12].

In this chapter the insulator-to-metal transition in In/Si(111) from the (8×2) to the (4×1) structure was induced by photodoping with a photon energy larger than the band gap ($\hbar\omega = 1$ eV $> \mathcal{E}_{gap} = 300$ meV). The electronic structure of the ground state as well as the subsequent transient states after photo-excitation were investigated with tr-ARPES.
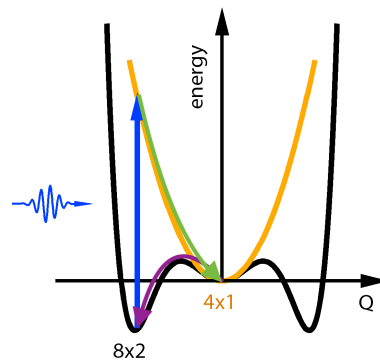
Figure 6.1 | Potential energy surface. PES as a function of a generalized reaction coordinate of the structural phase transition for $T < T_c$ (black), with the absolute minimum corresponding to the (8×2) phase and the other minimum at Q =0 to the (4×1) phase separated by a 40 meV potential barrier. Photo-excitation (blue) takes the system to a modified PES where the minimum corresponding to the (8×2) phase is quenched. Transition into the (4×1) phase after photo-excitation (green), and further relaxation to the (8×2) ground state (purple).

In Fig. 6.1 the potential energy surfaces for the (4×1) and (8×2) structures are shown in yellow and black, respectively, where Q is the generalized reaction coordinate of the structural phase transition [10]. As discussed in section 4.2, the potential energy surface for the (8×2) phase deviates from the standard Mexican hat shape and exhibits an additional minimum at $Q = 0$ that corresponds to a metastable (4×1) phase. The metastable state is separated from the true (8×2) ground state by a potential barrier of approximately 40 meV [10, 72]. Photo-excitation across the CDW gap is expected to bring the system from the black to the yellow potential energy surface along the blue arrow. After the excitation the system is expected to relax to the (4×1) minimum at $Q = 0$ (green arrow) and

eventually back into the (8 × 2) ground state (purple arrow). Tr-ARPES gives us access to the electronic structure before and after photo-excitation. The analysis of the evolution between the stable or metastable states to the ground states provides information of the underlying mechanisms. Different processes have specific timescales depending on their nature. A systematic temporal discrimination of elementary electronic and structural processes will unveil the dominant interaction [37].

Figure 6.2 (a) shows the band structure at T = 40 K measured at negative pump-probe delays. The band structure, shown here, looks different from the equilibrium photoemission spectrum of the (8 × 2) phase shown in Fig. 4.6 for three reasons:

- The ARPES spectra were taken with XUV pulses generated by the fundamental beam and not by the second-harmonic of the fundamental, resulting in a lower energy resolution.

- There is a mixture of the two phases in the ARPES spectra due to an incomplete equilibrium phase transition.

- The presence of the pump ($\hbar\omega$ = 1 eV) broadens the spectral features and causes some spectral weight to reappear at the metallic position of band m_1 below the Fermi level. The latter has also been observed in the material system for pump energies $\hbar\omega$ = 1.55 eV by Wolf´s group [11].

Figure 6.2 (b)-(d) shows the pump-induced changes of the band structure due to photo-excitation of the system with femtosecond pulses at 1.0 eV photon energy with a fluence of 4.18 mJ/cm^2 at different time delays. The pump-induced changes of the photo current are obtained by subtracting the photo-current at negative time delays from the photocurrent at each time delay. Gain and loss are shown in red and blue, respectively. At early times before the lattice is affected, electrons are represented by gain and holes by loss of the photocurrent. If photo-excitation modifies the electronic structure, gain and loss will give us a combination of occupation and changes in the band structure. At the peak of the electronic excitation (t = 0.1 ps) a broad distribution of photoexcited electrons and holes is observed. After 1.1 ps the pump-probe signal is mainly confined to the area below the Fermi level (0.0 eV) and closely resembles the difference plot in figure 4.6 (c) for the equilibrium insulator-to-metal phase transition following CDW melting. No further relaxation within 3 ps is observed, indicating a long-lived transient state.

Compared with the tr-ARPES data taken at room temperature in the (4 × 1) phase discussed in chapter 5, the pump-induced changes observed in the low-temperature data exhibit a completely different behavior. In contrast to the data for the (8 × 2) phase in figures 6.2 that show no relaxation within 3 ps, the pump-induced changes in the (4 × 1) were found to have a lifetime of approximately 1 ps and no photocurrent gain was found below the Fermi level. As explained in chapter 5, the pump-induced changes after photo-excitation of the (4 × 1) phase can be understood in terms of a hot electronic distribution characterized by a time-dependent electronic temperature without any underlying changes of the band structure, with a cooling time of (1.0 ± 0.1) ps for the hot electrons.

In order to quantify the CDW melting and relaxation dynamics the pump-probe signal was integrated over the areas indicated by the black boxes outlined in Fig. 6.2 (b) and (c) yielding the
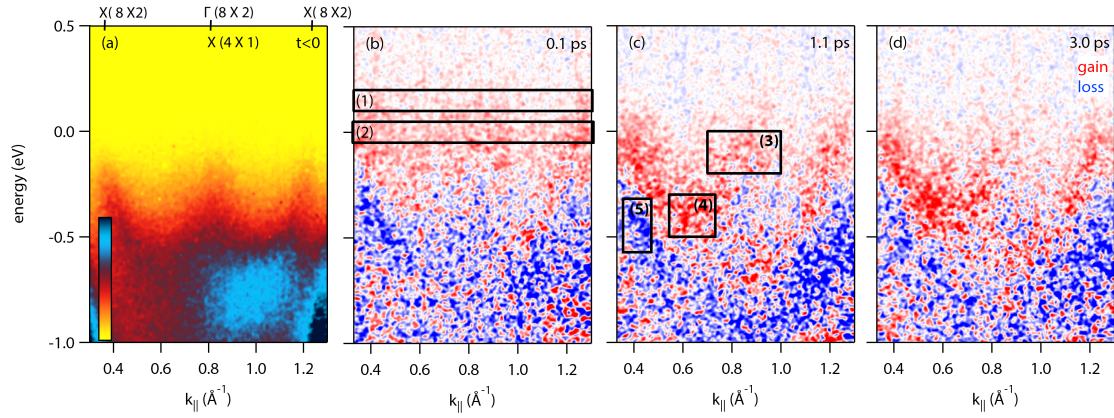
Figure 6.2 | Light-induced (1 eV) phase transition snapshots. (a) Average photocurrent at negative time delays at $T = 40$ K, (b)-(d) pump-induced changes at different time delays after photo-excitation with a photon energy of 1 eV and a fluence of 4.18 mJ/cm^2.

pump-probe traces in figure 6.3 (a). The boxes were chosen to highlight different features of the pump-probe signal. Box 1 is supposed to reveal the carrier dynamics of the unoccupied conduction band. Box 2, has been set to show the carriers in the band gap. Box 3 and box 4 were chosen at the location were the bottom of the m_1 and m_2 bands of the metallic phase should be. Box 5 is placed at the Brillouin zone boundary of the (8×2) phase in order to track the loss dynamics at the top of the valence band. From RD-fits (see appendix D) to the data (thick lines in figure 6.3 (a)), the rise and decay times shown in Fig. 6.3 (b) and (c) were obtained. The photocurrent in boxes 2 and 3 was fitted with a double exponential decay rather than a single exponential because they show two different timescales in the relaxation. At high energies (box 1) we obtained a short-lived pump-probe signal with a rise time of (0.13 ± 0.07) ps and decay time of (0.57 ± 0.10) ps attributed to the electronic excitation. The gap (box 2) was found to get populated on the same timescale as the electronic excitation, followed by a fast decay (0.6 ± 0.08) ps into a very long-lived state $(> 100 \text{ ps})$. The loss at the Brillouin zone boundary (box 5) was found to have a rise time comparable with the electronic excitation, but a long lifetime of (8 ± 2) ps. Band m_1 (box 3) was found to shift below the Fermi level in (0.26 ± 0.06) ps. Finally, we found a very long-lived response $(> 100 \text{ ps})$ with a slow rise time (0.66 ± 0.18) ps in box 4, reflecting the structural transition from the (8×2) to the (4×1) phase. Box 4 corresponds to the position of the m_2 band in the (4×1) phase. Therefore the occupation of electronic states at this position is a direct measurement of the structural transition.

Next, we compare our results to previous time-resolved reflection high-energy electron diffraction (tr-RHEED) measurements of the lattice dynamics [10, 87]. In [87], the structural (8×2) to (4×1) transition was found to occur within 350 fs (680 fs according to our definition of the rise time) in excellent agreement with the longest timescale observed in our data of 660 ± 180 fs. This number is slightly longer than 1/4 period of the two amplitude modes (310 fs and 420 fs, respectively [72]) which set the lower limit for CDW melting in a Peierls picture.

The recovery time of the (8×2) phase was found to be 440 ps with tr-RHEED [10], consistent
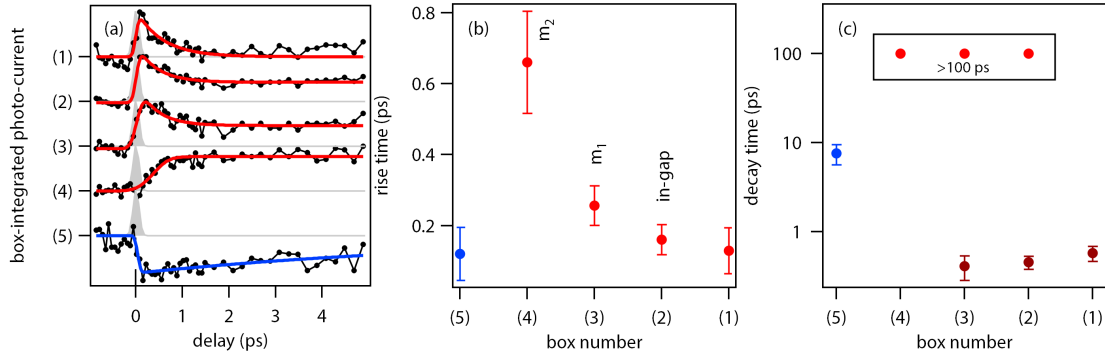
Figure 6.3 | CDW melting dynamics: above-gap excitation. (a) integrated photocurrent as a function of delay for the different boxes marked in Fig. 6.2. The gray shaded region represents the pump pulse. (b) and (c) rise time and relaxation time extracted from RD-fits to the data in (a). In (c) the long lifetime component (>100 ps) is indicate in the inset. Dark and light red distinguished between the fast and slow relaxation time.

with our value of $\tau > 100$ ps for the recovery of the insulating band structure. The long lifetime of the transient (4×1) phase in the tr-RHEED experiments was attributed to trapping in the metastable (4×1) phase shown in Fig. 6.1 [10]. Relaxation into the (8×2) phase was proposed to happen via condensation nuclei that grow with a velocity of 850 m/s [10]. Condensation nuclei are points where recovery of the (8×2) ground state starts. In agreement with [87] we find no indications for coherent amplitude mode oscillations in our data below T_c. This has been attributed to strong damping of the amplitude modes due to rapid energy transfer to various phonon modes of the surface and the substrate [87].

In recent tr-ARPES measurements of the CDW melting in In/Si(111) [11], three different timescales were found for the transition: The band gap was found to close within 200 fs, defining the ultrafast insulator-to-metal transition. Band m_1 was found to move below the Fermi level in 500 fs, and the structural transition was found to be completed in 700 fs. We found very similar timescales for the closing of the band gap and the structural transition as seen in integration boxes 2 and 4. However, we observed that m_1 shifts below the Fermi level in just ~ 260 fs. The reason for this difference is most probably that our ground state was a mixed state of the (4×1) and (8×2) phases. If m_1 is partially ocupied the electrons will easily increase their energy with the pump and ocupy box 3.

Based on DFT and *ab initio* molecular dynamics simulations, constrained by the experimental results in [11] the following microscopic understanding of the photo-induced transition was formulated [87, 11]: Localized holes at the (8×2) zone boundary break the dimer bonds characteristic for the hexagon structure. Electrons populate band m_1, which correspond to In-In bonds across neighboring chains. The population of these states lead to inter-atomic forces that transform the hexagonal structure to a zig-zag structure. Band m_1 is lowered down in energy as the indium atoms contributing to this bond approach.

To further investigate our findings the previous experiment was repeated with a lower fluence. The integrated photocurrent as a function of delay inside boxes 2, 3 and 4 in Fig. 6.2 for a 1 eV photo-

excitation at the (8×2) phase for two fluences is shown. The highest fluence corresponds to the data shown in Fig. 6.3. To quantify the dynamics the integrated photocurrent was fitted with a RD-fit or with a rise and double decay fit (RD2-fit). The fit results are shown in appendix D. For a fluence of 2.5 mJ/cm^2 we observe a very fast rise time (~ 200 fs) for box 2, related to the closing of the band gap. The structural changes (box 4) were found to have a slightly longer rise time of (~ 700 fs) than for the highest fluence. There are clearly two different effects giving rise to the increase of photocurrent at the m_1 band (box 3), fitted with two different rising curves. The fast timescale is related to the electronic excitation that populates states in m_1 above the gap or at the remaining metallic m_1 and the long rise time found is related to the shift of m_1 below the Fermi level. Similar carrier dynamics of the m_1 band were shown in [88].
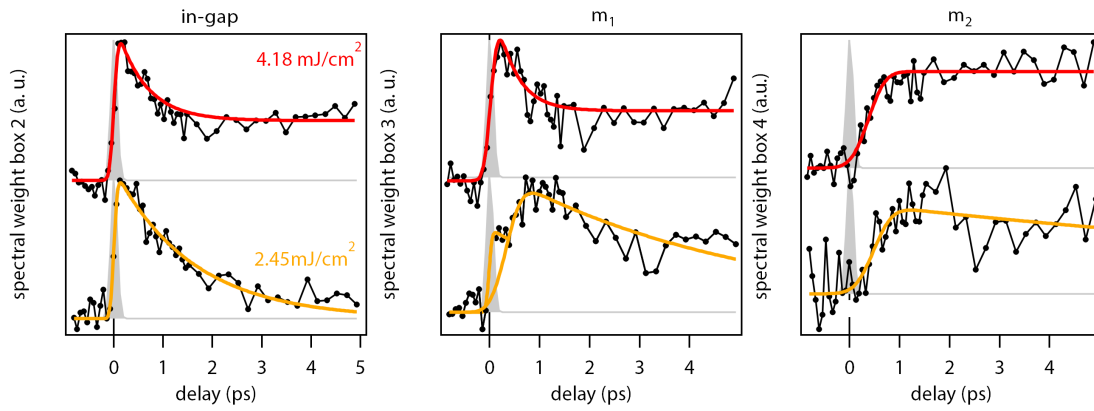

Figure 6.4 | CDW melting for different fluences. Integrated photocurrent as a function of delay for boxes 2, 3 and 4 marked in Fig. 6.2 for two different fluences. Solid lines are RD-fits to the data. In box 3 (2.45 mJ/cm^2) fitted with two curves. The gray shaded region represents the pump pulse.

For our limited fluence dependence we observed that the decay time increases with increasing fluence. Wall *et al.* [10] found out that the relaxation to the (8×2) phase starts at condensation nuclei and propagates by changing the atomic structure of the subsequent unit cell. Increasing the fluence reduces the amount of condensation nuclei and therefore, the recovery time increases. A complete melting will be achived when the system is trapped in the metastable state.

Frigge *et al.* [87] observed that the structural transition gets faster with increasing fluence up to the value of 680 fs. The photo-excitation modifies the potential energy surface. An increase in the pump fluence results in an increase of the potential energy surface slope until the potential energy surface transforms into the free enery surface of the high symmetry phase. Once a complete transformation is reached, higher fluences will just shift the potential energy surface without a change in the slope, maintaining the same transition time.

From the measured rise times and decay times for the two different fluences we can conclude that for a fluence of 4.2 mJ/cm^2 we observe a complete melting of the CDW and for a fluence of 2.5 mJ/cm^2 just an incomplete melting is observed.

We should also point out that before excitation of the (8×2) phase m_1 is partially visible. There-

fore, the excitation will not just melt the CDW of the (8×2) phase, but directly heat the electrons in the remaining (4×1) phase giving an even faster filling of the in-gap region. Just below box 3 in Fig. 6.2 a blue region can be identify providing evidence that there were carriers at m_1 before photo-excitation.

In summary we melted the CDW ground state of $In/Si(111) - (8\times2)$ by photo-excitation with femtosecond pulses. We observe that the gap closes in approximately 200 fs followed by the structural transition into the transient (4×1) structure in 660 fs. We found a long-lived (> 100 ps) transient state attributed to trapping in a (4×1) metastable state.

7 CDW Melting via Multiphoton Absorption: Below-Gap Excitation

The results of this chapter have been published in: *M. Chávez-Cervantes, G. E. Topp, S. Aeschlimann, R. Krause, S. A. Sato, M. A. Sentef, and I. Gierz. Charge density wave melting in one-dimensional wires with femtosecond sub-gap excitation*, Phys. Rev. Lett., **123**, 036405 (2019) [13].

Depending on photon energy, field strength, and size of the band gap, photodoping can occur via single-photon absorption, multiphoton absorption or tunneling ionization. Single-photon processes dominate the absorption whenever the photon energy is larger than the band gap. For photon energies smaller than the band gap, absorption is expected to occur via multiphoton processes or tunneling ionization. Which process is more likely to happen depends on the gap size, field strength and wavelength of the photo-excitation.

The development of MIR sources with MV/cm field strength [89, 90] enables us to investigate CDW melting dynamics following sub-gap excitation. In Fig. 7.1 we present tr-ARPES data taken at a temperature of 40 K for different pump-probe delays after photo-excitation with 300 fs laser pulses with a photon energy of $\hbar\omega = 190$ meV and a peak electric field of 0.9 MV/cm.
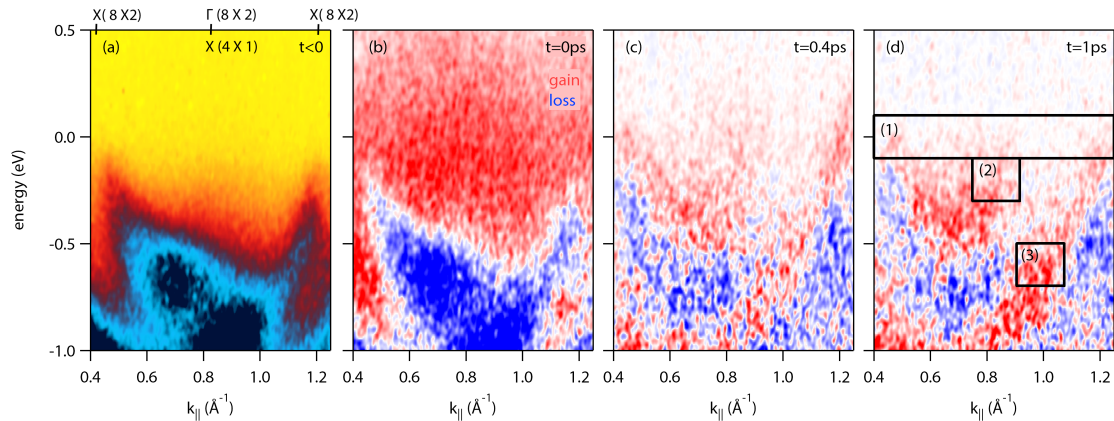
Figure 7.1 | Light-induced phase transition snapshots following below-gap excitation. (a) Measured band structure at negative pump-probe delay. (b) Pump-induced changes of the photocurrent in the presence of the 300 fs pump pulse with a photon energy of 190 meV with a peak electric field of 0.9 MV/cm. (c) Same as (b) but for a pump-probe delay of 0.4 ps. (d) same as (b) but for a pump-probe delay of 1 ps.

Panel (a) shows the average photocurrent taken at negative pump-probe delays, i.e. recorded before the arrival of the pump pulse. The features are broadened with respect to Fig. 4.6 (b) and

some spectral weight of band m_1 reappears due to the presence of the pump pulse. Panel (b) shows the pump-induced changes of the photocurrent at $t = 0$ ps, where pump and probe pulses overlap. The signal is dominated by the formation of sidebands of the unperturbed band structure due to laser-assisted photoemission LAPE as discussed in section 5.3. In Fig. 7.1 (d) we present the pump-probe signal recorded 1 ps after photo-excitation. The observed gain and loss features closely resemble those for the equilibrium insulator-to-metal transition in Fig. 4.6 (c), suggesting a transient melting of the CDW.

For a quantitative analysis of the CDW melting we integrate the pump-induced changes of the photocurrent over different areas marked by black boxes in Fig. 7.1 (d) that highlight three main features associated with CDW melting: the in-gap spectral weight (box 1), the shift of m_1 below the Fermi level (box 2), and the shift of m_3 towards the Fermi level (box 3). The integrated photocurrent is presented in Fig. 7.2 as a function of pump-probe delay for three data sets with different peak field strengths corresponding to 0.9, 0.7 and 0.3 MV/cm. For the lower peak field strengths there is almost no spectral weight after the LAPE contribution. In contrast for a peak field strength of 0.9 MV/cm (green data points) we found and increase in the spectral weight after the LAPE contributions. The rise time of the in-gap spectral weight in Fig. 7.2 (a) was found to be within the pulse duration of 300 fs. From RD-fits to the pump-probe signal in Figs. 7.2 (b) and (c) m_1 was found to shift below the Fermi level within 0.8 ± 0.3 ps and m_3 was found to shift towards the Fermi level within 1.1 ± 0.4 ps. These numbers are similar albeit slightly longer compared to those obtained for photo-excitation at $\hbar\omega = 1$ eV discussed in chapter 6 and at $\hbar\omega = 1.55$ eV in previous time-resolved electron diffraction [10, 87] and tr-ARPES investigations [11]. This indicates that the microscopic picture for the photo-induced melting of the CDW is the same for $\hbar\omega = 190$ meV and $\hbar\omega \geq 1$ eV.
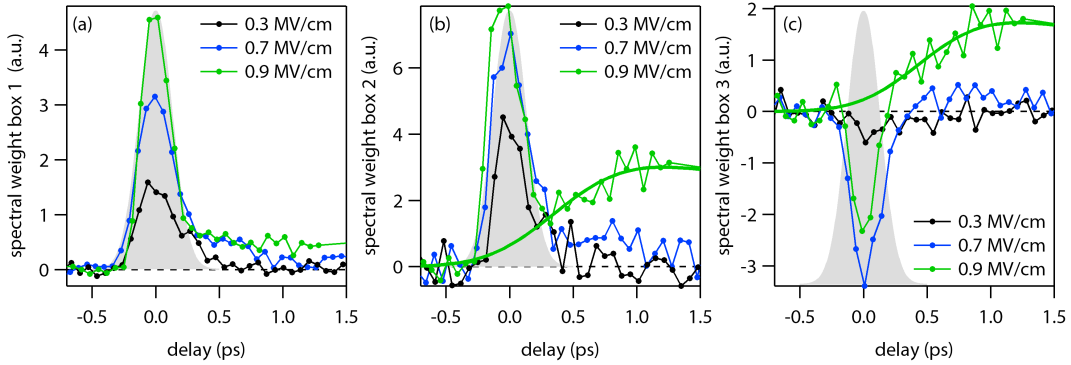
Figure 7.2 | CDW melting dynamics: below-gap excitation. Integrated photocurrent over the areas marked by the black boxes in Fig. 7.1 (d). The gray-shaded region represents the pump pulse. (a) In-gap spectral weight as a function of pump-probe delay for different peak field strengths from box (1). The rise time of the in-gap spectral weight is shorter than the pump pulse. (b) Down-shift of m_1 from box (2) with a rise time of 0.8 ± 0.3 ps. (c) Up-shift of m_3 from box (3) with a rise time of 1.1 ± 0.4 ps.

Next, we investigated the lifetime of the transient state. Figure 7.3 shows the spectral weight for peak field strength 0.9 MV/cm (green data points) from Fig. 7.2 but plotted over a bigger time window

together with RD-fits revealing (6 ± 1) ps lifetime for the transient state.

It was shown in [87] that the time scale for the structural transition decreases with increasing fluence. Further, for very low fluences when the excitation density lies below 0.4 electrons per (8 × 2) unit cell, the structural transition was found to remain incomplete resulting in a few-picosecond lifetime rather than a lifetime of τ > 100 ps as observed in the case of a complete CDW melting. Therefore, the long rise time of ~ 1 ps together with the short lifetime of ~ 6 ps most likely indicate a partial melting of the CDW.

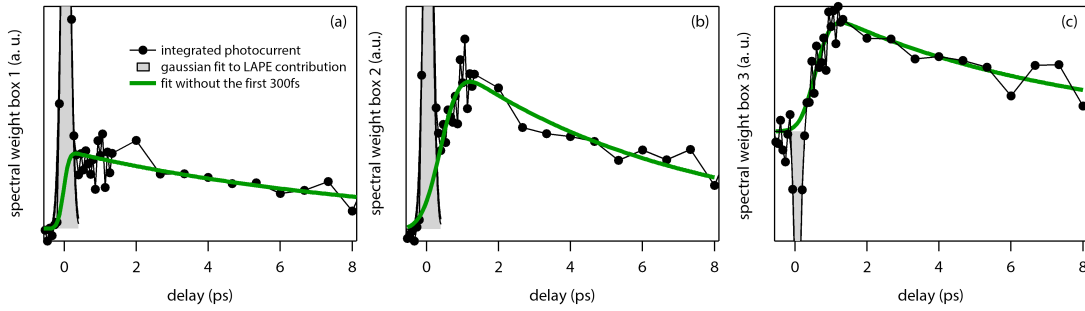**Figure 7.3 | Relaxation dynamics after CDW melting.** Integrated photocurrent as a function of delay at three different momentum-energy zones (a) in-gap region, (b) m_1 position and (c) above m_3.

After providing direct experimental evidence for partial melting of the CDW in one-dimensional indium wires with strong pump pulses the photon energy of which is smaller than the CDW gap in Figs. 7.1, 7.2 and 7.3 we now set out to unravel the underlying mechanism. Nicholson *et al.* [11] previously identified the formation of zone-boundary holes as the primary driving force for the light-induced phase transition in one-dimensional indium wires. With that in mind we can compare our findings to related insulator-to-metal phase transition observed in different materials following photo-excitation with strong MIR and THz pulses.

Monney *et al.* [91] showed that MIR pulses at $\hbar\omega$ = 400 meV, resonant to an optical transition between the backfolded valence and conduction band, melts the CDW in 1T-TiSe$_2$. We use a pump energy of $\hbar\omega$ = 190 meV < $\mathcal{E}_{gap}$ ~ 300 meV, which is why we exclude single-photon absorption across the gap as possible route for CDW melting in the present case. Also, the employed pump photon energy is much smaller than the indirect band gap of silicon, $\mathcal{E}_{gap}$ = 1.1 eV. Therefore, substrate-induced effects such as a transient heating of the sample above the critical temperature are unlikely.

Further, Rini *et al.* [92] showed that resonant excitation of an infrared-active phonon mode at $\hbar\omega$ = 71 meV results in a five-orders of magnitude drop in resistivity in Pr$_{0.7}$Ca$_{0.3}$MnO$_3$. The In/Si(111) − (8 × 2) phase has a maximum phonon frequency of a few THz (few tens of meV) [8, 86], which is much smaller than the pump photon energy of 190 meV. Hence, we can also exclude a resonant excitation of the lattice.

Alternatively, Rini *et al.* [93] demonstrated that defect-mediated sub-gap absorption at $\hbar\omega$ = 180 meV < $\mathcal{E}_{gap}$ = 670 meV in polycrystalline VO$_2$ films drives the phase transition via the generation of photoholes in the valence band of VO$_2$. Due to the single-crystalline nature of our samples we

consider defect-mediated sub-gap absorption as too weak to be able to drive the insulator-to-metal phase transition.

Finally, in [94, 95] strong THz electromagnetic fields were used to drive the insulator-to-metal transition in single crystals of VO_2 which was attributed to tunneling ionization across the gap.

Aside from single-photon absorption and tunneling ionization, multiphoton absorption emerges as a third scenario that might provide the non-equilibrium carrier distribution required to drive the insulator-to-metal phase transition. As we excluded single-photon absorption for an excitation with a photon energy of $\hbar\omega = 190$ meV of the insulating (8×2) phase we are left with two possible scenarios. We can distinguish between tunneling ionization and multiphoton absorption by considering the Keldysh parameter γ_K that is given by the square root of the ratio between gap size and pondero-motive energy, where $\gamma_K > 1$ and $\gamma_K < 1$ correspond to photo-excitation via multiphoton absorption and tunneling, respectively [96]. From the experimental parameters we obtain $\gamma_{K:exp}$=1.6 implying multiphoton absorption. The calculation of the Keldysh is shown in appendix C.
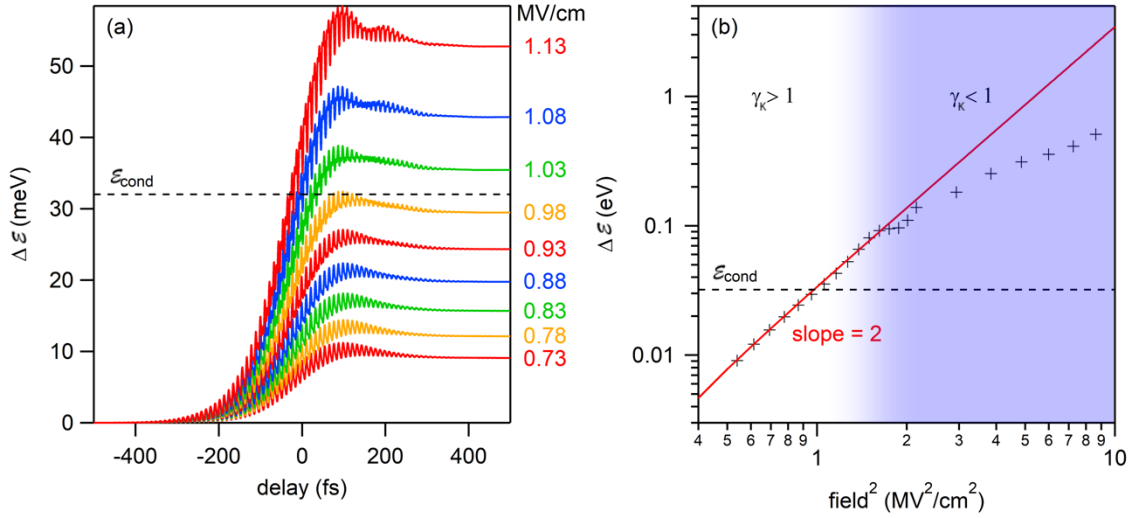
Figure 7.4 | Calculated absorbed energy. (a) Absorbed energy as a function of time for different peak field strengths. The dashed line indicates the CDW condensation energy of 32 meV per (4×2) unit cell. (b) Log-log plot of absorbed energy versus the square of the peak field. The red line has a slope of two as expected for two-photon absorption. White and blue areas distinguish the multiphoton ($\gamma_K > 1$) and the tunneling regime ($\gamma_K < 1$), respectively.

In order to support this interpretation, G. E. Topp [1] simulated the interaction of the MIR pump pulse with our sample and calculated the change in total energy of the system ΔE for different field strengths as a function of pump-probe delay shown in Fig. 7.4 (a). The calculations based on a tight-binding model with the Hamiltonian introduced in the supplementary material of [72] for the In/Si(111) $- (8 \times 2)$ surface are provided in appendix B. We found that for field strengths above ~ 1 MV/cm the absorbed energy exceeds the CDW condensation energy of 32 meV at $T = 40$ K [9] and the latter is expected to melt. The theoretically predicted threshold field agrees well with the

---

[1] Sentef Lab, Theory of Pump-Probe Spectroscopy Group at MPSD Hamburg

Figure 7.5 | Oscillation of the CDW ground state. Integrated photocurrent as a function of delay at m_1 position. The oscillation of the photocurrent has a frequency of (0.6 ± 0.1) THz.
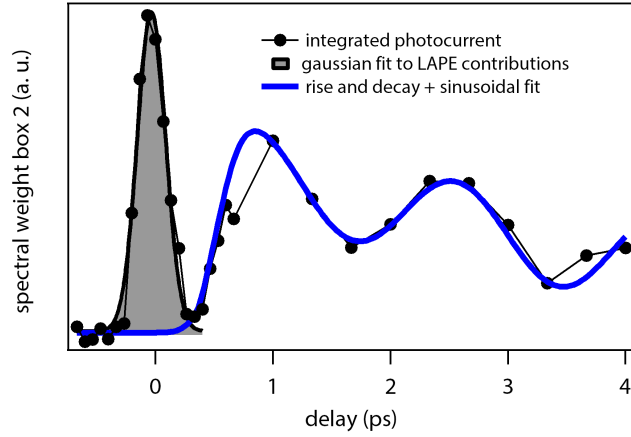
experimental value of 0.9 MV/cm. The small discrepancy between the two values is attributed to uncertainties regarding the size of the gap (literature values range ~ 120 meV [75, 77] to 350 meV [78, 11]) and the condensation energy (literature values range from 47 meV [9] to 66 meV [58] at $T = 0$ K). Further, both quantities are expected to decrease as a function of time when the pump pulse hits the sample. As the model uses a fixed gap size of 300 meV it is expected to overestimate the field required to melt the CDW. Also, the measured rise and decay times indicate that CDW melting might be incomplete such that the experimental threshold field of 0.9 MV/cm should be considered as a lower boundary of the actual threshold field.

The log-log plot of absorbed energy versus intensity (field squared) in figure 7.4 (b) allows us to distinguish between multiphoton and tunneling regime as the two regimes exhibit different slopes. For fields below 1.3 MV/cm we fitted a line with a slope of two indicating that each photoexcited electron absorbs two photons. For higher fields the absorbed energy exhibits a slower increase indicating tunneling ionization. Note that the deviation from a slope of two coincides with the crossover between $\gamma_K > 1$ and $\gamma_K < 1$ (blue shaded area in figure 7.4 (b)) and that the threshold field for CDW melting lies in the multiphoton regime in agreement with the experimental Keldysh parameter.

In contrast to our tr-ARPES data for $\hbar\omega = 1$ eV, some data sets for $\hbar\omega = 190$ eV show indications for coherent amplitude mode oscillations. In Fig. 7.5 the integrated photocurrent around m_1 as a function of delay is plotted. The pump-probe signal was extracted from a data set with a peak electric field of 0.9 MV/cm. The photocurrent intensity was fitted with a RD-fit. The residual of the fit was then fitted with a sinusoidal function to obtain the frequency of the oscillation, which was found to be 0.6 THz with a phase of $\phi = \pi$. The frequency matches the theoretical frequency of the shear displacement mode from the (8×2) phase, one of the amplitude modes responsible for the insulator-to-metal phase transition. It is worth noticing that Nicholson [97] also observed coherent oscillations at 20 K with a 1.55 eV excitation between the m_2 and m_3 bands for low fluence (max 1.1 mJ/cm^2). The measured frequency was 0.8 THz and was attributed to the rotary mode of the (8×2) phase, which

is the other mode associated with the phase transition. In case of complete charge density wave melting we would not expect amplitude mode oscillations because the system gets trapped in the new metastable state. We speculate that for incomplete CDW melting, the damping of the amplitude modes might be reduced allowing for their experimental observation.

In summary, for strong-field MIR excitation at photon energies smaller than the CDW gap, we observe a transient melting of the CDW on a timescale that is similar to the one observed at pump photon energies $\hbar\omega \geq 1\,\text{eV}$, indicating a similar microscopic melting mechanism. Supported by a simple model we attribute our results to photodoping via multiphoton absorption.

8 Summary and Outlook

8.1 Summary

In chapter 5 we have used tr-ARPES to probe the population dynamics after photo-excitation of the metallic phase in one-dimensional indium wires on Si(111). We found that electrons thermalized within our temporal resolution, i. e. the electronic distribution followed a Fermi-Dirac distribution at every time delay. A cooling time of ~ 1 ps was found: Energy is dissipated to a bath of cold phonons consistent with a two-temperature model. Coherent oscillations of the pump-probe signal revealed strong coupling between electrons and a phonon, that modulates the distance between neighboring indium wires.

We have also used tr-ARPES to probe the band structure changes during a metal-to insulator transition in the indium wires in two different photo-excitation regimes (below- and above-gap) as discussed in chapters 7 and 6. The band gap was found to be filled within our temporal resolution in both cases. The band structure changes were found to be completed in ~ 0.66 ps in the case of single photon absorption and in ~ 1 ps for multi-photon absorption. These timescales are slightly longer than 1/4 period of the amplitude modes of the system consistent with a Peierls transition which agrees with tr-RHEED investigations [10, 87] and recent tr-ARPES experiments [11]. After photo-excitation the system was found to get trapped in a metastable (4×1) phase with $\tau > 100$ ps lifetime for the single-photon absorption. A lifetime of only $\tau \sim 6$ ps for the transient state was found for multi-photon absorption, indicative of an incomplete phase transition. The observed rise times agree with the microscopic picture of the photo-induced phase transition proposed by [11]. There, photo-holes at the (8×2) zone boundary are responsible for breaking the dimer bonds between the outer chain of indium atoms. Simultaneously, the electrons populate states at $\Gamma_{8\times2}$ forming In-In bonds between neighboring chains, leading to inter-atomic forces that transform the hexagonal structure into the zig-zag structure.

8.2 Open Questions

In chapter 6 we presented the melting dynamics with two different fluences for a pump photon energy of 1 eV. For these two fluences the time constants found are consistent with previous tr-ARPES and tr-RHEED measurements. However, the dynamics that we observe for an even lower fluence show a unexpected behavior. In Fig. 8.1 we observe that for a fluence of 1mJ/cm^2 the rise time in all boxes is very fast (~ 200 fs) similar to the electronic excitation as observed in box 2 (in-gap) for the other fluences. The relaxation time for box 3 (m$_1$) is less than a picosecond but there is a long lived signal

in box 2 and box 4 (m_2) (18 ps and 7 ps, respectively). The fast rise and decay times in box 3 could be explained as an occupation of m_1 above the Fermi level or an occupation of the remaining metallic m_1 without an structural transition. However, the puzzling part is that we observe a fast and relatively long lived signal above m_2 (box 4). To date we have no explanation for this counter-intuitive behavior.
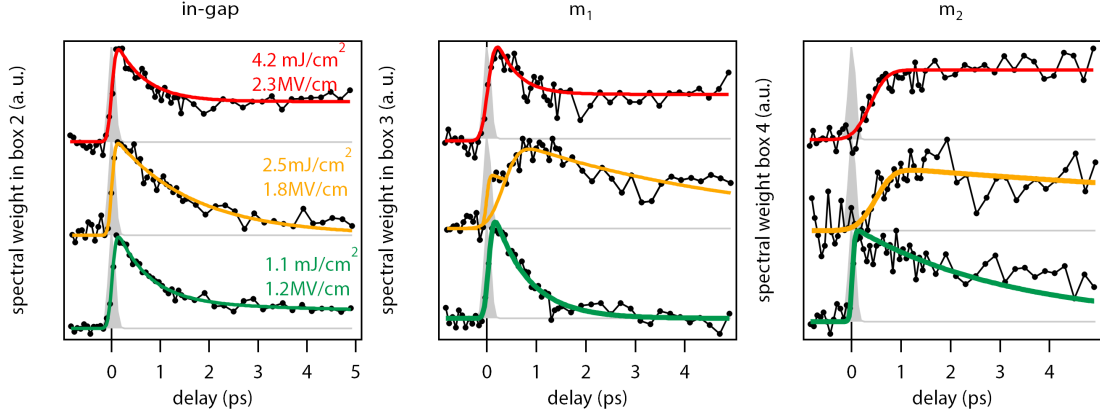

Figure 8.1 | CDW melting for different fluences. Integrated photocurrent as a function of delay for boxes 2, 3, 4 marked in Fig. 6.2 for three different fluences.

In chapter 6 we assumed that photodoping is reached by bringing electrons across the band gap via single-photon absorption because the photon energy used is larger than the band gap. To support this assumption G. E. Topp calculated the absorbed energy of the $In/Si(111) - (4 \times 2)$ surface during the interaction with a vertically polarized laser pulse at $\hbar\omega = 1\,eV$ ($E \perp$ to the wires) and a pulse duration (FWHM) of $\Delta t = 200$ fs following the same model as used in chapter 7 and described in appendix B. The calculated absorbed energies are shown in Fig. 8.2 (a). We found here that for a peak field strength of 0.3 MV/cm the absorbed energy is higher than the condensation energy. In the log-log plot of absorbed energy versus intensity (field squared, Fig. 8.2 (b)) the peak electric field necessary for CDW melting lies on the line with slope = 1, in agreement with a single-photon absorption picture, as expected. However, the simulations show a region where the absorbed energy decreases with increasing fluence that we do not understand. In the experiment we needed much higher peak electric fields than 0.3 MV/cm to melt the CDW. For a peak electric field of ~ 1.2 MV/cm we observe the peculiar behavior explained before. The CDW was found to partially melt for ~ 1.8 MV/cm and completely melt for a peak field of ~ 3 MV/cm. For a better understanding of the CDW melting dynamics a bigger number of experimental data sets with different fluences should be investigated.

From our experiments we see no difference between the metallic equilibrium phase and the transient metallic state reached following the light-induced phase transition. It would be interesting to investigate whether the transient state is the same as the equilibrium metallic states. This might be realized by exciting the transient metastable metallic state by a subsequent pulse and compare the dynamics with the dynamics of the equilibrium metallic state shown in chapter 5.

From the timescales found for the two different excitation regimes for the CDW melting we concluded that the microscopic mechanism that triggers the phase transition is the same in both ex-
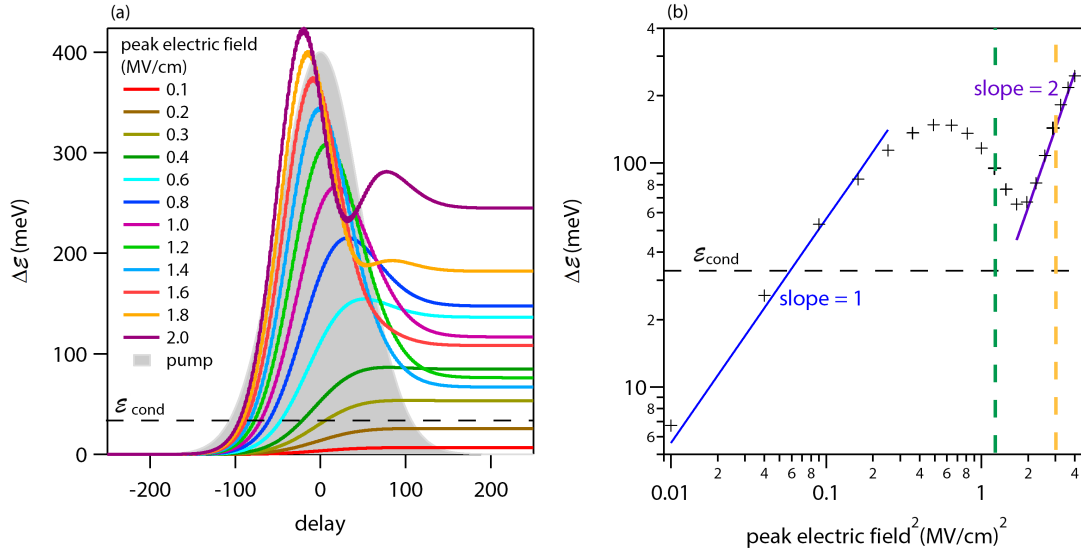
Figure 8.2 | Calculated absorbed energy. Absorbed energy as a function of time for different peak field strengths for a laser pulse with 1eV photon energy. The dashed line indicates the CDW condensation energy of 32 meV per (4×2) unit cell. (b) Log-log plot of absorbed energy versus the square of the peak field. The dashed colored vertical lines indicate the square peak field used for measurements shown in Fig. 8.1.

citations regimes. Can we obtain a complete melting of the CDW by increasing the peak electric field in the multi-photon regime? Is there a difference in the mechanism that avoids a complete melting following MIR excitation?

8.3 Outlook: Dynamical Band Structure Engineering

The manipulation of solids by coherent light sources gives the possibility of achieving new states of matter or of stabilizing states that are not stable in the unperturbed system. The light field can couple to the solid by displacing the atoms or electrons periodically. In both cases the Hamiltonian $\mathcal{H}(t)$ describing the perturbed system will depend on time. Within Floquet's framework a time independent Hamiltonian $\mathcal{H}_{eff}$ can be found which describes the quasi-stationary properties of the perturbed system. In first approximation we have $\mathcal{H}_{eff} = \mathcal{H}_0 + \mathcal{H}(t)$ where $\mathcal{H}_0$ is the equilibrium Hamiltonian and $\mathcal{H}(t)$ is given by the driving field. The eigenstates of $\mathcal{H}_{eff}$ can be controlled by tailoring the driving field.

Resonant excitation of infrared-active phonon modes

Laser pulses resonant to IR-active phonon modes of the system will displace the atoms and periodically modulate the orbital overlap (hopping parameter) between neighboring atoms and therefore the electronic properties of the system. The band structure changes arising from the excitation of IR-active modes occur at twice the driving frequency. Further, non-linear coupling to Raman-active
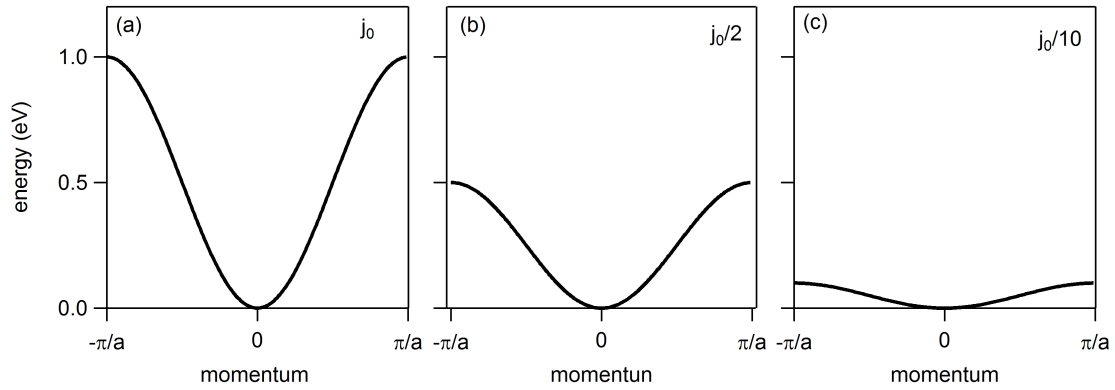
Figure 8.3 | Dynamical localization. Tight-binding dispersion for a 1D crystal for different hopping parameters.

phonons (ionic Raman scattering) might lead to the displacive excitation of a Raman mode creating a new transient crystal structure with new electronic properties. Resonant excitation of IR-active phonons has been shown to induce an insulator-to-metal transition in $Pr_{07}Ca_{03}MnO_3$ [92] and explained by non-linear phonon coupling to a Raman active mode [98]. Non-linear phonon coupling was directly observed in [99], where MIR-pulses were used to resonantly excite the Mn-O stretching mode in $La_{07}Sr_{03}MnO_3$ at $\nu = 18$ THz and observed oscillations at 1.2 THz attributed to a Raman active mode. Non-linear coupling to Raman modes has also been used to drive a system into a superconducting state even at room temperatures in $YBa_2Cu_3O_{6.5}$ [100, 101, 102].

Coherent Interaction Between Light and Bloch Electrons

A charged particle on a discrete lattice under the action of an electric field will move following the driving field. Electrons in a one-dimensional crystal with lattice constant a under a sinusoidal electric field E with frequency ω exhibit an effective hopping parameter given by $j_{eff} = j_0 \mathcal{J}_0\left(\frac{eEa}{\hbar\omega}\right)$, where j_0 is the hopping parameter without the driving field and $\mathcal{J}_0$ is the zero order Bessel function. If $\frac{eEa}{\hbar\omega} = 2.405$ then j_{eff} will become zero and the electrons will be localized [103]. To observe the effect the following condition needs to be fulfill $\omega\tau > 1$ were τ is the scattering rates for the electrons in the system. In Fig. 8.3 (a) the first electronic band for a 1D crystal using the tight-binding model is shown. In (b) and (c) the hopping parameter was reduced by a factor of 2 and 10, respectively. As the hopping reduces the bands get flatter until electrons become completely localized. This effect could be used to induce a metal-to-insulator transition. Dynamical localization has been observed in cold atoms experiments [104, 105], but so far has never been observed in crystals.

Application to Indium Wires

One possibility to engineer the band structure of the indium wires grown on Si(111) dynamically is to excite the IR-active phonons of the system. For example by non-linear coupling to one of the Raman
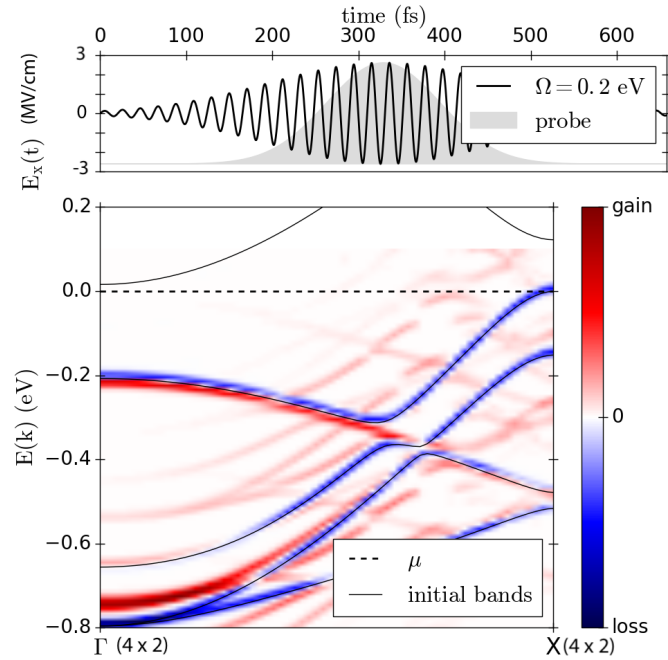
Figure 8.4 | Electronic band structure engineering. (a) Simulated difference tr-ARPES spectra of the In/Si(111)−(4×2) phase during photo-excitation at a photon energy of 200 meV with a peak field strength of 2.6 MV/cm^2. Polarization along the wires. Courtesy of G. E. Topp.

active amplitude modes we could induce a metal-to-insulator transition at $T > T_c$. The phonon frequencies of the indium wires are on the order of 1 THz [86]. Therefore, the first requirement is a THz pump combined with tr-ARPES. At the moment the highest wavelength we can reach with our pump beam is $\lambda = 15\,\mu m$(20 THz), requiring big changes to the current tr-ARPES setup.

The other possibility is to make use of the dynamical localization. In this case we would expect that by applying a strong sinusoidal electromagnetic field to the indium wires we would observe a flattening of the bands. The effect is proportional to $(1/\omega)$. To visualize the expected changes in the band structure, G. E. Topp and M. A. Sentef calculated the interaction of the Indium wires with a MIR laser pulse and simulated the ARPES spectra at the peak of the excitation. For this the tight-binding model from [72] was used with hopping parameters set to match our experimental band structure. The ARPES simulation at the peak of the excitation with a laser pulse at $\lambda = 6.2\,\mu m$($\hbar\omega =$ 200 meV) is shown in Fig. 8.4. The pump had a temporal FWHM of 300 fs and a peak field strength of 2.6 MV/cm^2 with a polarization along the wires.

The simulations show important changes in the band structure that could be detected with our experimental energy resolution. To observe dynamical localization we also need to consider the following:

- Fulfill condition $\omega\tau > 1$. The electronic scattering times for metals are around 10 fs, requiring $\omega > 100$ THz ($\lambda < \mu m$). In order to be able to drive with a longer wavelength we need a

system with longer scattering times. Insulators have infinite scattering rates because the band is completely occupied and there is no free phase space to scatter to. For this reason we will investigate dynamical localization on the insulating phase of the indium wires.

- Minimize LAPE effects. As explained in section 3.3.1 LAPE effects are maximized when the polarization of the driving field has a component in the photo-electron's propagation direction. For MIR pulses the effect can completely hide the carrier dynamics while the pump is present as shown in section 5.3. An almost complete suppression of LAPE can be achieved by minor changes of the measurement geometry.

- Avoid CDW melting. If we melt the CDW the changes of the band structure related to dynamical localization might be mixed with the changes associated to the CDW and difficult to disentangle. In addition, the system will be metallic with $\tau \sim 10\,\text{fs}$.

A Thermodynamic Potential and Phase Transitions

In this appendix a summary of Landau's theory of phase transitions is given following [106]. The macroscopic state of a system can be described in terms of thermodynamic potentials, one of which being the Helmholtz free energy $F(V, T)$, henceforth referred to as free energy. The change in energy in a system can be quantified by the change in its free energy.

$$dF(V, T) = -S\,dT - P\,dV \tag{A.1}$$

were S is the entropy, P the pressure, V the volume and T the temperature of the system. If more parameters define the state of the system, the change in the potential should be augmented by terms proportional to differentials of the other parameters

$$dF = -S\,dT - P\,dV + \sum_i \Lambda_i\,d\lambda_i. \tag{A.2}$$

The mean value of the derivative of the Hamiltonian with respect to any parameter (λ) is equal to the derivative of any thermodynamic potential (F, G, W, E) with respect to the same parameter (λ).

A system at equilibrium corresponds to a minimum of $F(V, T)$. Followings Landaus theory, we can describe quantitatively the change in the structure of a body while passing through a phase transition by defining a quantity Δ called the order parameter, that can be given for example as the displacement of the atoms in the crystal. The order parameter takes a non-zero value in the low symmetry phase and turns to zero in the high symmetry phase. The free energy $F(V, T, \Delta)$ can be written as a Taylor expansion of the order parameter around the transition point. The potential $F(V, T, \Delta)$ is symmetric. Therefore only the even powers of the expansion contribute,

$$F(P, T, \eta) = F_0 + A(V, T)\Delta^2 + B(V, T)\Delta^4 + C(V, T)\Delta^6 + \mathcal{O}^6. \tag{A.3}$$

The equilibrium values of the order parameter are given by the minimum of the thermodynamic potential, i.e.

$$\frac{dF(\Delta)}{d\Delta} = 0 \tag{A.4}$$

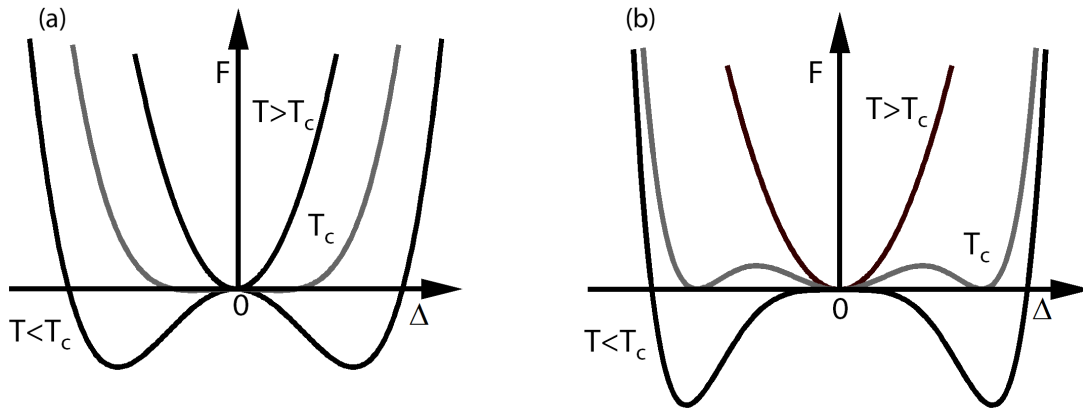$$\frac{d^2F(\Delta)}{d\Delta^2} > 0 \tag{A.5}$$

Figure A.1 | Thermodynamic potential. (a) for a second order phase transition and (b) for a first order phase transition

From this conditions and setting F(Δ = 0) to be a minimum for the high symmetry phase the values of the parameters A, B, and C can be found.

According to Landau the phase transition can be divided in two kinds. The corresponding free energy curves are shown in figure A.1. The second kind shown in Fig. A.1 (a) presents a continuous change of state, but presents a discontinuous symmetry change. The $\mathcal{O}^4$ terms in equation A.3 have almost no contribution, leaving $F(P, T, \eta) = F_0 + A(V, T)\Delta^2$. To fullfill the previous conditions $A(V, T) > 0$ for $T > T_c$ and $A(V, T) < 0$ for $T < T_c$, forcing $A(V, T) = 0$ at the transition point leading to a continuous change of state. Therefore, the thermodynamic potential of each phase on the far side of a transition point corresponds to a non-equilibrium state. The order parameter will change continuously as a function of temperature in a second order phase transition. The first kind has a discontinuous change of state shown in Fig. A.1 (b). The thermodynamic potentials $F_1(V, T)$ and $F_2(V, T)$ of the two phases are equal at the transition point, each function on either side of the transition correspond to an equilibrium state of the order parameter. As $F(V, T)$ can have several minima, different metastable states can exist separated by a potential barrier. In the high symmetry phase ($T > T_c$), where T_c is the transition temperature, the potential has a parabolic shape with one minimum at $\Delta = 0$, but as the temperature goes below T_c a new minimum at $\Delta \neq 0$ appears, corresponding to the new ground state often accompanied by a broken symmetry. For a first order phase transition there is a temperature at which both phases describe equilibrium states generating a discontinuity in the order parameter.

B Theoretical Model for Absorbed Energy

The critical field strength necessary to melt the CDW by the MIR pump pulse was obtained by computing the absorbed energy in a tight-binding model[1]. For simplicity the model Hamiltonian introduced in the Supplementary Material of [72] was used, with parameters adjusted to reproduce the reported direct band gap of approximately 300 meV from the DFT-HSE06 calculation [58], and close to the recently reported estimate of 250 meV [11]. To this end the following choice of hopping integrals and onsite energies for the CDW phase (in eV, notation as in [72]) was used: $\varepsilon_0 = 0.056$, $\varepsilon_I = 0.089$ (on-site potentials), $t_0 = -0.29$, $t_0' = -0.545$, $t_{I1} = 0.1$, $t_{I1}' = 0.55$, $t_{I2} = -0.104$ and $t_{I0} = 0.147$ (next-neighbour hopping integrals). The corresponding band structure in the reduced 4 × 2 Brillouin zone (BZ) is shown in Fig. B.1. The key feature relevant for the discussion in the main text is the 300 meV direct band gap at the reduced zone boundary.
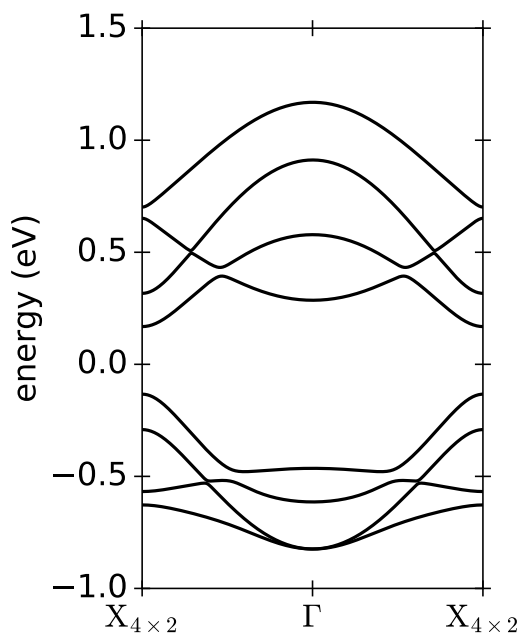

Figure B.1 | Model band structure. Band structure of the broken symmetry phase with a 300 meV direct band gap at the X-point of the reduced (4×2) Brillouin zone.

$e = \hbar = c = 1$ was set to sample the one-dimensional reduced BZ with 1024 k-points, and the

---

[1] The simulations and calculation presented in this Appendix were performed by G. E. Topp.

temperature was set to T = 40 K. The pump pulse is included via a time-dependent vector potential $\mathbf{A}(t) = A_{\max} p_{\sigma_p}(t) \sin(\Omega t) \mathbf{e}_x$ with a Gaussian envelope $p_{\sigma_p}(t) = \exp(-(t - t_0)^2/(2\sigma_p^2))$ and a linear polarization along the wire $\mathbf{e}_x$ via Peierls substitution in the tight-binding model. We use the midpoint Euler real-time propagation scheme with a time step of δt = 0.07 fs. The peak electric field strength is related to the maximum of the vector potential as $E_{\max} = \Omega A_{\max}$ [107]. The peak vector potential $A_{\max}$ is given in units of the inverse lattice constant of the $(4{\times}1)$ unit cell, $(3.84\,\text{Å})^{-1}$. Values reported in chapter 7 range from $A_{\max} = 0.21 - 0.29\,(3.84\,\text{Å})^{-1}$, corresponding to peak electric field strengths ranging from $E_{\max}$ = 1.02 - 1.42 MV/cm. As in the experiment, we use a pump photon frequency Ω = 190 meV and a pulse duration of 300 fs at FWHM. The reported absorbed energy (Fig. 7.4 (a)) is then computed from the difference of the initial energy and the final energy after the pump. The CDW condensation energy reported in Fig. 7.4 (b) is taken from [58, 9], corresponding to the 300 meV CDW band gap reported therein.

C Experimental Details

C.1 Calculation of the Peak Electric Field

We estimate the peak electric field in the surface of the sample parallel to the wires as follows. First we measure the average power P and the spot size d (FWHM of the Gaussian beam profile) at the sample position. The pump pulse duration Δt is obtained by fitting the time dependence of the LAPE signal with a Gaussian the width of which is the cross-correlation between pump and probe pulses with a nominal pulse duration of 100 fs (FWHM). From these parameters the peak intensity of the pump pulse is:

$$I = \frac{4P}{R\Delta t\pi d^2} \tag{C.1}$$

where R is the 1 kHz repetition rate of the laser. The incident electric field strength E_i is given by:

$$E_i = \sqrt{\frac{2I}{c\epsilon_0}} \tag{C.2}$$

with the speed of light c and the vacuum permitivity ϵ_0. The ratio between the incoming field E_i and the transmitted field E_t is given by the Fresnel equation for p-polarized light:

$$\frac{E_t}{E_i} = \frac{2\cos\theta_i}{n\cos\theta_i + \cos\theta_t} \tag{C.3}$$

where $n = 3.42$ is the refractive index of the silicon substrate at 6.6μm and $\theta_i = 25°$ is the angle of incidence of the light. θ_t is related to θ_i via Snell's law. The field amplitude projected into the surface of the sample along the direction of the wires $E_{t,x}$ can be calculated as

$$\frac{E_{t,x}}{E_i} = \frac{E_t\cos\theta_t}{E_i}. \tag{C.4}$$

All things considered, the field strength in the surface of the sample in the direction parallel to the wires is given by:

$$E_{t,x} = 0.44E_i. \tag{C.5}$$

C.2 Keldysh Parameter

The Keldysh parameter is given by

$$\gamma_K = \frac{2\pi\nu\sqrt{2m^*\mathcal{E}_{\text{gap}}}}{eE} \tag{C.6}$$

where ν is the frequency of the pump, m^* is the effective mass, $\mathcal{E}_{\text{gap}} = 300\,\text{meV}$ is the size of the band gap, e is the charge of the electron, and E is the peak electric field. The effective mass m^* is determined from parabolic fits of the valence and conduction band of the (8×2) structure in [58] as

$$\frac{1}{m^*} = \frac{1}{m_{\text{VB}}} + \frac{1}{m_{\text{CB}}} = 0.08m_e \tag{C.7}$$

yielding $m^* = 0.08m_e$ where m_e is the mass of the free electron. The fits for the valence and conduction bands are shown in Fig. C.1. For a field strength of 0.9 MV/cm we get a Keldysh parameter $\gamma_K = 1.64$.
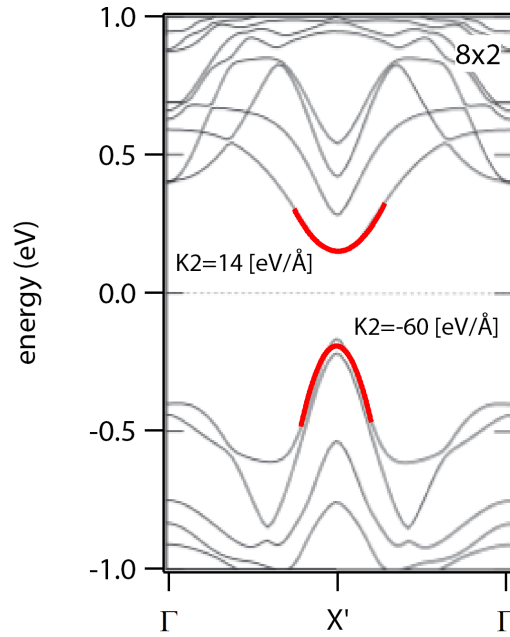

Figure C.1 | Effective mass from dispersion. In/Si(111) − (8 × 2) band structure from [58] and fitted parabolas at band gap to obtain the effective mass.

D Fit Functions

Rise and Decay Fit

The product of a step edge and an exponential decay convolved with a Gaussian was used to fit the integrated photocurrent as a function of delay between the pump and the probe. The fitting function is given by:

$$I(t) = \frac{a}{2}\left[1 + \text{erf}\left(\frac{(t - t_0)/\tau - rt^2/(8\ln2)}{rt\tau/2\sqrt{\ln2}}\right)\right]\exp\left(\frac{rt^2/(8\ln2)^2 - 2(t - t_0)\tau}{2\tau^2}\right) \tag{D.1}$$

where a is the amplitude of the photocurrent, rt is the full width at half maximum of the derivative of the rising edge, t_0 is the inflection point of the rising edge and τ is the exponential lifetime.

Rise and Double Decay Fit

In cases where the integrated photocurrent as a function of delay could not be fitted with a single exponential decay a double exponential decay was used. The fit function is given by the product of a step edge and a double exponential decay convolved with a Gaussian.

$$I(t) = \frac{a}{2}\left[1 + \text{erf}\left(\frac{(t - t_0)/\tau_1 - rt^2/(8\ln2)}{rt\tau_1/2\sqrt{\ln2}}\right)\right]\left[\exp\left(\frac{rt^2}{(8\sqrt{2}\ln2\tau_1)^2}\right)\right]$$
$$\times\left[a_1\exp\left(\frac{-(t - t_0)}{\tau_1}\right) + (1 - a_1)\exp\left(\frac{-(t - t_0)}{\tau_2}\right)\right] \tag{D.2}$$

where τ_1 and τ_2 are the two decay times. The parameter a_1 is a factor that determines the relative amplitude of each exponential decay.

Fermi-Dirac Distribution Fit

The momentum-integrated photocurrent from the ARPES spectra yields an EDC.

$$EDC = n(\varepsilon) \times f_{\text{FD}} \tag{D.3}$$

The EDCs were divided by the density of states $n(\varepsilon)$ and then fitted with a Fermi-Dirac distribution (f_{FD}) convoluted with a Gaussian to account for the energy resolution of the system. The

electronic temperature of the system was extracted from the Fermi-Dirac distribution. The follow-ing equations were used in the fit procedure.

$$I(\varepsilon) = af_{FD}(\varepsilon) \otimes G(\varepsilon) \tag{D.4}$$

$$f_{\text{FD}}(\varepsilon) = \frac{1}{\exp\left(\frac{\varepsilon-\mu}{k_B T}\right) + 1} \tag{D.5}$$

$$G(\varepsilon) = \exp\left(\frac{-4\ln(2)\varepsilon^2}{w^2}\right) \tag{D.6}$$

where a is the amplitude, μ is the chemical potential, k_B is Boltzmann's constant, T the tempera-ture and w the Gaussian FWHM.

Data Sets and Fitting Parameters

In table D.1 the fitting parameters for the data sets presented in section 5.1 are summarized.

Table D.1 | Electronic peak temperatures. Extracted peak temperatures and cooling times after pho-toexcitation of the metalic phase of the indum wires at room temperature for different fluences, photon energies and polarization.

wavelength	photon energy	polarization	fluence	temperature	rise time	relaxation time
μm	eV		mJ/cm^2	K	fs	ps
0.79	1.57	V	1.5	1781	250	1.1
1.24	1	V	2.3	1700	100	0.6
4.5	0.28	V	2.2	1200	250	0.7
4.5	0.28	H	2.2	1700	300	0.5
6.6	0.19	V	1.5	900	150	0.9
6.6	0.19	H	1.5	1700	250	1.2
7.3	0.17	V	1.9	1100	250	0.7
7.3	0.17	H	2.0	2500	200	0.9
7.3	0.17	H	0.64	2200	--	--
7.3	0.17	H	0.05	1100	--	--

Table D.2 shows the extracted rise and decay times from fiting the integrated photocurrent as a function of time shown in Fig. 6.4 and Fig. 8.1.

Table D.2 | Rise and decay times. Fitting parameters for CDW melting at different fluences.

in-gap spectral weigth (box 2)				
fluence	**peak E**	**rise time**	**decay**	**double decay**
mJ/cm^2	MV/cm	fs	ps	ps
4.1	2.3	160±35	0.6±0.2	100±10
2.5	1.8	140±35	1.6±0.1	
1.1	1.2	160±15	0.7±0.1	18±1

m1 shift (box 3)				
fluence	**peak E**	**rise time**	**decay**	**double decay**
mJ/cm^2	MV/cm	fs	ps	ps
4.1	2.3	260±65	0.4±0.1	100±10
2.5	1.8	120±65	600±80	5±0.7
1.1	1.2	170±30		0.7± 0.05

m2 shift (box 4)			
fluence	**peak E**	**rise**	**decay**
mJ/cm^2	MV/cm	fs	ps
4.1	2.3	660 ± 180	100 ± 10
2.5	1.8	700 ± 250	150 ± 10
1.1	1.2	120 ± 50	7 ± 0.2

Two-Temperature Model Fit

To verify that the electronic temperature in our system follows the two-temperature model presented in chapter 2, we fitted the electronic temperature extracted from the EDC of the tr-ARPES data with the numerical solution of the two temperature model. The results are shown in Fig. D.1.

The fit fuction was obtained by numerically integrating the following coupled differential equations:

$$\frac{dT_{el}}{dt} = \frac{1}{\gamma T_{el}}\left(-g(T_{el} - T_{ph}) + A_p \exp\left(-\frac{4\ln 2 t}{w^2}\right)\right) \tag{D.7a}$$

$$\frac{dT_{ph}}{dt} = \frac{g}{C_{ph}}(T_{el} - T_{ph}) \tag{D.7b}$$

where T_{el} and T_{ph} are the electronic and phononic temperature. The other parameters are the electron-phonon coupling g, the phonon heat capacity C_{ph} and the electron heat capacity constant γ. A_p is the amplitude of the heat transfer from the pump pulse to the electronic system and w is the duration of the pump pulse (FWHM). The parameters to fit the data are listed in table D.3.
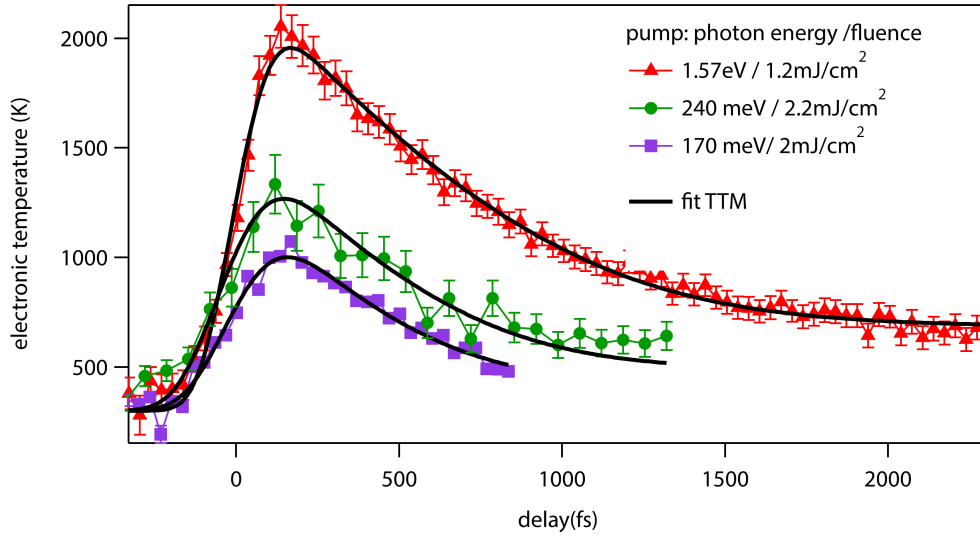
Figure D.1 | Electronic temperature extracted from tr-ARPES data. Data from chapter 5 with two-temperature model (TTM) fit . Electronic temperatures extracted from the angle-integrated photo-emission spectra corresponding to all three bands.

Table D.3 | Two-temperature model constants. Parameters from numerical fit to data

band	photon energy	rise time	A_p	g	γ	C_{ph}
	eV	fs (FWHM)	W/m^3	W/Km^3	J/(K^{2}m^3)	J/(K^{2}m^3)
all	1.57	186	4.6×10^{20}	6.93×10^{16}	3.61×10^1	2.22×10^5
all	0.17	237	1.09×10^{20}	6.93×10^{16}	3.61×10^1	2.22×10^5
all	0.28	243	1.7×10^{20}	6.93×10^{16}	3.61×10^1	2.22×10^5
m_2	0.28	243	1.3×10^{20}	6.93×10^{16}	3.61×10^1	2.22×10^5
m_3	0.28	243	2.13×10^{20}	6.93×10^{16}	3.61×10^1	2.22×10^5

As the system In/Si(111)-(4 × 1) remains the same, the parameters g, γ and C_{ph} were obtained from the fit to one curve (pump 1.57 eV) and then kept fixed for the other curves. The system equilibrium temperature before the interaction with the light pulse was fixed to 300 K for all curves.

Bibliography

[1] H. Fröhlich. Theory of the superconducting state. I. The ground state at the absolute zero of temperature. *Phys. Rev.*, 79:845–856, 1950.

[2] R. E. Peierls. *Quantum Theory of Solids*. Oxford, first edition, 1955.

[3] P. M. Grant, R. L. Greene, G. C. Wrighton, and G. Castro. Temperature dependence of the near-infrared optical properties of tetrathiofulvalinium tetracyanoquinodimethane (TTF-TCNQ). *Phys. Rev. Lett.*, 31:1311–1314, 1973.

[4] P. Brüesch, S. Strässler, and H. R. Zeller. Fluctuations and order in a one-dimensional system. a spectroscopical study of the Peierls transition in $K_2Pt(CN)_4Br_{0.3}\cdot(3H_2O)$. *Phys. Rev. B*, 12:219–225, 1975.

[5] S. Iwai, M. Ono, A. Maeda, H. Matsuzaki, H. Kishida, H. Okamoto, and Y. TokuraY. Ultrafast optical switching to a metallic state by photoinduced Mott transition in a halogen-bridged nickel-chain compound. *Phys. Rev. Lett.*, 91:057401, 2003.

[6] A. Cavalleri, Cs. Tóth, C. W. Siders, J. A. Squier, F. Ráksi, P. Forget, and J. C. Kieffer. Femtosecond structural dynamics in VO_2 during an ultrafast solid-solid phase transition. *Phys. Rev. Lett.*, 87:237401, 2001.

[7] M. Chollet, L. Guerin, N. Uchida, S. Fukaya, H. Shimoda, T. Ishikawa, K. Matsuda, T. Hasegawa, A. Ota, H. Yamochi, G. Saito, R. Tazaki, S. Adachi, and S. Koshihara. Gigantic photoresponse in ¼-filled-band organic salt (EDO-TTF)2PF6. *Science*, 307(5706):86–89, 2005.

[8] K. Fleischer, S. Chandola, N. Esser, W. Richter, and J. F. McGilp. Surface phonons of the $Si(111) : In-(4 \times 1)$ and (8×2) phases. *Phys. Rev. B*, 76:205406, 2007.

[9] S. Wippermann and W. G. Schmidt. Entropy explains metal-insulator transition of the Si(111)-In nanowire array. *Phys. Rev. Lett.*, 105:126102, 2010.

[10] S. Wall, B. Krenzer, S. Wippermann, S. Sanna, F. Klasing, A. Hanisch-Blicharski, M. Kammler, W. G. Schmidt, and M. Horn von Hoegen. Atomistic picture of charge density wave formation at surfaces. *Phys. Rev. Lett.*, 109:186101, 2012.

[11] C. W. Nicholson, A. Lücke, W. G. Schmidt, M. Puppin, L. Rettig, R. Ernstorfer, and M. Wolf. Beyond the molecular movie: Dynamics of bands and bonds during a photoinduced phase transition. *Science*, 362(6416):821–825, 2018.

[12] M. Chávez-Cervantes, R. Krause, S. Aeschlimann, and I. Gierz. Band structure dynamics in indium wires. *Phys. Rev. B*, 97:201401, 2018.

[13] M. Chávez-Cervantes, G. E. Topp, S. Aeschlimann, R. Krause, S. A. Sato, M. A. Sentef, and I. Gierz. Charge density wave melting in one-dimensional wires with femtosecond sub-gap excitation. *Phys. Rev. Lett.*, 123:036405, 2019.

[14] W. A. Little. Possibility of synthesizing an organic superconductor. *Phys. Rev.*, 134:A1416–A1424, 1964.

[15] C. Kittel. *Introduction to Solid State Physics*. John Wiley and Sons, Inc., 1301 Sansome St., San Francisco, CA 94111, USA, eight edition, 2005.

[16] M. Fowler. Electrons in one dimension: the Peierls transition. Graduate Quantum Mechanics Lectures Notes Online, 2007.

[17] R. E. Peierls. *More Surprises in Theoretical Physics*. Princeton University Press, 41 William St., Princeton, New Jersey 08540, USA, first edition, 1991.

[18] G. Grüner. *Density Waves in Solids*. Perseus Publishing, Cambridge MA., 1994.

[19] G. Grüner. The dynamics of charge-density waves. *Rev. Mod. Phys.*, 60:1129–1181, 1988.

[20] S. I. Anisimov, B. L. Kapeliovich, and T. L. Perel'man. Electron emission from metal surfaces exposed to ultrashort laser pulses. *Zh. Eksp. Teor. Fiz.*, 66:776, 1974.

[21] L. Rettig. *Ultrafast Dynamics of Correlated Electrons*. PhD thesis, Freie Universität Berlin, 2012. http://www.fhi-berlin.mpg.de/~wolf/femtoweb/docs/thesis/rettig_2012_diss.pdf, retrieved on 2019-03-09.

[22] M. I. Kaganov, I. M. Lifshitz, and L. V. Tanatarov. Relaxation between electrons and the crystalline lattice. *J. Exptl. Theoret. Phys.*, 4(2):173–178, 1957.

[23] P. B. Allen. Theory of thermal relaxation of electrons in metals. *Phys. Rev. Lett.*, 59(13):1460–1463, 1987.

[24] L. Perfetti, P. A. Loukakos, M. Lisowski, U. Bovensiepen, M. Wolf, H. Berger, S. Biermann, and A. Georges. Femtosecond dynamics of electronic states in the Mott insulator 1T-TaS2 by time resolved photoelectron spectroscopy. *New Journal of Physics*, 10(5):053019, 2008.

[25] C.-K. Sun, F. Vallée, L. H. Acioli, E. P. Ippen, and J. G. Fujimoto. Femtosecond-tunable measurement of electron thermalization in gold. *Phys. Rev. B*, 50:15337–15348, 1994.

[26] R. H. M. Groeneveld and R. Sprik. Femtosecond spectroscopy of electron-electron and electron-phonon energy relaxation in Ag and Au. *Phys. Rev. B*, 51(17):11433–11445, 1995.

[27] M. Lisowski, M. Loukakos, P. A. Bovensiepen, J. Stähler, C. Gahl, , and M. Wolf. Ultra-fast dynamics of electron thermalization, cooling and transport effects in Ru(001). *Applied Physics A*, 78:165, 2004.

[28] K. Ishioka and O. V. Misochko. Coherent lattice oscillations in solids and their optical control, part I. In K. Yamanouchi, A. Giulietti, K. Ledingham, F. P. Schäfer, J. P. Toennies, and W. Zinth, editors, *Progress in Ultrafast Intense Laser Science*, volume 98 of Springer Series in Chemical Physics, page 23–63. Springer Berlin Heidelberg, 2010.

[29] L. Dhar, J. A. Rogers, and K. A. Nelson. Time-resolved vibrational spectroscopy in the impulsive limit. *Chemical Reviews*, 94(1):157–193, 1994.

[30] H. J. Zeiger, J. Vidal, T. K. Cheng, E.P. Ippen, G. Dresselhaus, and M. S. Dresselhaus. Theory for displacive excitation of coherent phonons. *Phys. Rev. B*, 45:768–778, 1992.

[31] T. Dekorsy, G. C. Cho, and H. Kurz. Coherent phonons in condensed media. In M. Cardona and G. Güntherodt, editors, *Light Scattering in Solids VIII. Topics in Applied Physics*, volume 76, page 169–209. Springer Berlin Heidelberg, 2006.

[32] P. Kusar, V. V. Kabanov, J. Demsar, T. Mertelj, S. Sugai, and D. Mihailovic. Controlled vaporization of the superconducting condensate in cuprate superconductors by femtosecond photoexcitation. *Phys. Rev. Lett.*, 101:227001, 2008.

[33] L. Perfetti, P. A. Loukakos, M. Lisowski, U. Bovensiepen, H. Berger, S. Biermann, P. S. Cornaglia, A. Georges, and M. Wolf. Time evolution of the electronic structure of $1T-\text{TaS}_2$ through the insulator-metal transition. *Phys. Rev. Lett.*, 97:067402, 2006.

[34] F. Schmitt, P. S. Kirchmann, U. Bovensiepen, R. G. Moore, L. Rettig, M. Krenz, J.-H. Chu, N. Ru, L. Perfetti, D. H. Lu, M. Wolf, I. R. Fisher, and Z.-X. Shen. Transient electronic structure and melting of a charge density wave in TbTe_3. *Science*, 321(5896):1649–1652, 2008.

[35] T. Rohwer, S. Hellmann, M. Wiesenmayer, C. Sohrt, A. Stange, B. Slomski, A. Carr, Y. Liu, L. M. Avila, M. Kalläne, S. Mathias, L. Kipp, K. Rossnagel, and M. Bauer. Collapse of long-range charge order tracked by time-resolved photoemission at high momenta. *Nature*, 471(7339):490, 2011.

[36] J. C. Petersen, S. Kaiser, N. Dean, A. Simoncig, H. Y. Liu, A. L. Cavalieri, C. Cacho, I. C. E. Turcu, E. Springate, F. Frassetto, L. Poletto, S. S. Dhesi, H. Berger, and A. Cavalleri. Clocking the melting transition of charge and lattice order in $1T-\text{TaS}_2$ with ultrafast extreme-ultraviolet angle-resolved photoemission spectroscopy. *Phys. Rev. Lett.*, 107:177402, 2011.

[37] S. Hellmann, T. Rohwer, M. M. Kalläne, K. Hanff, C. Sohrt, A. Stange, A. Carr, M. M. Murnane, H. C. Kapteyn, L. Kipp, M. Bauer, and K. Rossnagel. Time-domain classification of charge-density-wave insulators. *Nature Communications*, 3:1069, 2012.

[38] H. Y. Liu, I. Gierz, J. C. Petersen, S. Kaiser, A. Simoncig, A. L. Cavalieri, C. Cacho, I. C. E. Turcu, E. Springate, F. Frassetto, L. Poletto, S. S. Dhesi, Z.-A. Xu, T. Cuk, R. Merlin, and A. Cavalleri. Possible observation of parametrically amplified coherent phasons in $\text{K}_{0.3}\text{MoO}_3$ using time-resolved extreme-ultraviolet angle-resolved photoemission spectroscopy. *Phys. Rev. B*, 88:045104, 2013.

[39] S. Mathias, S. Eich, J. Urbancic, S. Michael, A. V. Carr, S. Emmerich, A. Stange, T. Popmintchev, T. Rohwer, M. Wiesenmayer, A. Ruffing, S. Jakobs, S. Hellmann, P. Matyba, C. Chen, L. Kipp, M. Bauer, H. C. Kapteyn, H. C. Schneider, K. Rossnagel, M. M. Murnane, and M. Aeschlimann. Self-amplified photo-induced gap quenching in a correlated electron material. *Nature Communications*, 7:12902, 2016.

[40] L. Rettig, R Cortés, J.-H. Chu, I. R. Fisher, F. Schmitt, R. G.Moore, Z.-X. Shen, P. S. Kirchmann, M. Wolf, and U. Bovensiepen. Persistent order due to transiently enhanced nesting in an electronically excited charge density wave. *Nature Communications*, 7:10459, 2016.

[41] R. T. Williams, T. R. Royt, J. C. Rife, J. P. Long, and M. N. Kabler. Picosecond time–resolved photoelectron spectroscopy of ZnTe. *Journal of Vacuum Science and Technology*, 21(2):509–513, 1982.

[42] H. Hertz. Über einen Einfluss des ultravioletten Lichtes auf die elektrische Entladung. *Annalen der Physik*, 267:983, 1887.

[43] A. Einstein. Über einen die Erzeugung und Verwandlung des Lichtes betreffenden heuristischen Gesichtspunkt. *Annalen der Physik*, 17:132, 1905.

[44] J. Hölzl and F. K. Schulte. *Work function of metals*. Springer Berlin Heidelberg, Berlin, Heidelberg, 1979.

[45] S. Hüfner. *Photoelectron Spectroscopy*. Springer-Verlag Berlin Heidelberg GmbH, 1995.

[46] A. Damascelli. Probing the electronic structure of complex systems by ARPES. *Physica Scripta*, T109:61–74, 2004.

[47] D. Strickland and G. Mourou. Compression of amplified chirped optical pulses. *Optics Communications*, 55(6):447–449, 1985.

[48] Rick Trebino. *Frequency-Resolved Optical Gating: The Measurement of Ultrashort Laser Pulses*. Springer Science+Business LLC, 2002.

[49] J. D. Koralek, J. F. Douglas, N. C. Plumb, J. D. Griffith, S. T. Cundiff, H. C. Kapteyn, M. M. Murnane, and D. S. Dessau. Experimental setup for low-energy laser-based angle resolved photoemission spectroscopy. *Review of Scientific Instruments*, 78(5):053905, 2007.

[50] P. B. Corkum. Plasma perspective on strong field multiphoton ionization. *Phys. Rev. Lett.*, 71:1994–1997, 1993.

[51] A. D. Shiner, C. Trallero-Herrero, N. Kajumba, H.-C. Bandulet, D. Comtois, F. Légaré, M. Giguère, J-C. Kieffer, P. B. Corkum, and D. M. Villeneuve. Wavelength scaling of high harmonic generation efficiency. *Phys. Rev. Lett.*, 103:073902, 2009.

[52] MDSwo. The three step model. Wikipedia, 2007. `https://commons.wikimedia.org/w/index.php?curid=7669983`, CC BY-SA 3.0, retrieved on 2019-03-09.

[53] S. Eich, A. Stange, A. V. Carr, J. Urbancic, T. Popmintchev, M. Wiesenmayer, K. Jansen, A. Ruffing, S. Jakobs, T. Rohwer, S. Hellmann, C. Chen, P. Matyba, L. Kipp, K. Rossnagel, M. Bauer, M. M. Murnane, H. C. Kapteyn, S. Mathias, and M. Aeschlimann. Time- and angle-resolved photoemission spectroscopy with optimized high-harmonic pulses using frequency-doubled ti:sapphire lasers. *Journal of Electron Spectroscopy and Related Phenomena*, 195:231 – 236, 2014.

[54] J. L. Krause and K. J. Schaferand K. C. Kulander. High-order harmonic generation from atoms and ions in the high intensity regime. *Phys. Rev. Lett.*, 68:3535–3538, 1992.

[55] F. Frassetto, C. Cacho, C. A. Froud, I. C. E. Turcu, P. Villoresi, W. A. Bryan, E. Springate, and L. Poletto. Single-grating monochromator for extreme-ultraviolet ultrashort pulses. *Opt. Expr.*, 19(20):19169–19181, 2011.

[56] F. Mahmood, C.-K. Chan, Z. Alpichshev, D. Gardner, Y. Lee, P. A. Lee, and N. Gedik. Selective scattering between Floquet-Bloch and Volkov states in a topological insulator. *Nature Physics*, 12(04):306, 2016.

[57] L. P. Oloff, K. Hanff, A. Stange, G. Rohde, F. Diekmann, M. Bauer, and K. Rossnagel. Pump laser-induced space-charge effects in HHG-driven time- and angle-resolved photoelectron spectroscopy. *Journal of Applied Physics*, 119(22):225106, 2016.

[58] S.-W. Kim and J.-H. Cho. Origin of the metal-insulator transition of indium atom wires on Si(111). *Phys. Rev. B*, 93:241408, 2016.

[59] J. J. Lander and J. Morrison. Surface reactions of silicon (111) with aluminum and indium. *Journal of Applied Physics*, 36(5):1706–1713, 1965.

[60] J. Kraft, M.G. Ramsey, and F. P. Netzer. Surface reconstructions of In on Si(111). *Phys. Rev. B*, 55:5384–5393, 1997.

[61] J. Nogami, S. Parkl, and C. F. Quate. Indium-induced reconstructions of the Si(111) surface studied by scanning tunneling microscopy. *Phys. Rev. B*, 36:6221–6224, 1987.

[62] D. M. Cornelison, M. S. Worthington, and I. S. T. Tsong. Si(111) − (4 × 1)In surface reconstruction studied by impact-collision ion-scattering spectrometry. *Phys. Rev. B*, 43:4051–4056, 1991.

[63] J. L. Stevens, M. S. Worthington, and I. S. T. Tsong. (4 × 1) reconstruction of indium deposited on vicinal Si(111) surfaces. *Phys. Rev. B*, 47:1453–1459, 1993.

[64] T. Abukawa, M. Sasaki, F. Hisamatsu, T. Goto, T. Kinoshita, A. Kakizaki, and S. Kono. Surface electronic structure of a single-domain Si(111) − (4 × 1)–In surface: a synchrotron radiation photoemission study. *Surf. Sci.*, 325(1):33 − 44, 1995.

[65] O. Bunk, G. Falkenberg, J. H. Zeysing, L. Lottermoser, R. L. Johnson, M. Nielsen, F. Berg-Rasmussen, J. Baker, and R. Feidenhans'l. Structure determination of the indium-induced Si(111) − (4 × 1) reconstruction by surface X-ray diffraction. *Phys. Rev. B*, 59:12228–12231, 1999.

[66] H. W. Yeom, S. Takeda, E. Rotenberg, I. Matsuda, K. Horikoshi, J. Schaefer, C. M. Lee, S. D. Kevan, T. Ohta, T. Nagao, and S. Hasegawa. Instability and charge density wave of metallic quantum chains on a silicon surface. *Phys. Rev. Lett.*, 82:4898–4901, 1999.

[67] C. González, F. Flores, and J. Ortega. Soft phonon, dynamical fluctuations, and a reversible phase transition: Indium chains on silicon. *Phys. Rev. Lett.*, 96:136101, 2006.

[68] G. Lee, S.-Y. Yu, H. Kim, and Ja-Young Koo. Defect-induced perturbation on Si(111) − (4 × 1)−In: Period-doubling modulation and its origin. *Phys. Rev. B*, 70:121304, 2004.

[69] C. González, J. Ortega, and F. Flores. Metal–insulator transition in one-dimensional In-chains on Si(111): combination of a soft shear distortion and a double-band Peierls instability. *New Journal of Physics*, 7(1):100, 2005.

[70] J. Guo, G. Lee, and E. W. Plummer. Intertwined electronic and structural phase transitions in the In/Si(111) interface. *Phys. Rev. Lett.*, 95:046102, 2005.

[71] J. J. Lander and J. Morrison. Surface reactions of silicon with aluminum and with indium. *Surface Science*, 2:553 – 565, 1964.

[72] E. Jeckelmann, S. Sanna, W. G. Schmidt, E. Speiser, and N. Esser. Grand canonical Peierls transition in In/Si(111). *Phys. Rev. B*, 93:241407, 2016.

[73] J. R. Ahn, J. H. Byun, H. Koh, E. Rotenberg, S. D. Kevan, and H. W. Yeom. Mechanism of gap opening in a triple-band Peierls system: In atomic wires on Si. *Phys. Rev. Lett.*, 93:106401, 2004.

[74] H. Morikawa, C. C. Hwang, and H. W. Yeom. Controlled electron doping into metallic atomic wires: Si(111) − (4 × 1)-In. *Phys. Rev. B*, 81:075401, 2010.

[75] Y. J. Sun, S. Agario, S. Souma, K. Sugawara, Y. Tago, T. Sato, and T. Takahashi. Cooperative structural and Peierls transition of indium chains on Si(111). *Phys. Rev. B*, 77:125115, 2008.

[76] C. Kumpf, O. Bunk, J. H. Zeysing, Y. Su, M. Nielsen, R. L. Johnson, R. Feidenhans'l, and K. Bechgaard. Low-temperature structure of indium quantum chains on silicon. *Phys. Rev. Lett.*, 85:4916–4919, 2000.

[77] H. W. Yeom, K. Horikoshi, H. M. Zhang, K. Ono, and R. I. G. Uhrberg. Nature of the broken-symmetry phase of the one-dimensional metallic In/Si(111) surface. *Phys. Rev. B*, 65:241307, 2002.

[78] S. Chandola, K. Hinrichs, M. Gensch, N. Esser, S. Wippermann, W. G. Schmidt, F. Bechstedt, K. Fleischer, and J. F. McGilp. Structure of Si(111)-In nanowires determined from the mid-infrared optical response. *Phys. Rev. Lett.*, 102:226805, 2009.

[79] T. Tanikawa, I. Matsuda, T. Kanagawa, and S.Hasegawa. Surface-state electrical conductivity at a metal-insulator transition on silicon. *Phys. Rev. Lett.*, 93:016801, 2004.

[80] O. Gallus, T. Pillo, M. Hensberger, P. Segovia, and Y. Baer. A system with complex phase transition: Indium chains on Si(111). *Eur. Phys. J. B*, 20:313, 2001.

[81] T. Frigge. *Ultraschnelle strukturelle Nichtgleichgewichtsdynamik des optisch angeregten* Si(111)(8 × 2) → (4 × 1)-In *Phasenübergangs*. PhD thesis, Universität Duisburg-Essen, 2016. https://duepublico2.uni-due.de/servlets/MCRFileNodeServlet/duepublico_ derivate_00041735/Frigge_Diss.pdf, retrieved on 2019-03-09.

[82] J.-L. Lin, D. Y. Petrovykh, J. Viernow, F. K. Men, D. J. Seo, and F. J. Himpsel. Formation of regular step arrays on $Si(111) - (7 \times 7)$. *Journal of Applied Physics*, 84(1):255–260, 1998.

[83] D. Vlachos, M. Kamaratos, S. D. Foulias, F. Bondino, E. Magnano, and M. Malvestuto. Indium growth on reconstructed $Si(111) \sqrt{3} \times \sqrt{3}$ and 4×1 In surfaces. *The Journal of Physical Chemistry C*, 114(41):17693–17702, 2010.

[84] G. Saathoff, L. Miaja-Avila, M. Aeschlimann, M. M. Murnane, and H. C. Kapteyn. Laser-assisted photoemission from surfaces. *Phys. Rev. A*, 77:022903, 2008.

[85] A. F. Kemper, M. A. Sentef, B. Moritz, J. K. Freericks, and T. P. Devereaux. Effect of dynamical spectral weight redistribution on effective interactions in time-resolved spectroscopy. *Phys. Rev. B*, 90:075126, 2014.

[86] E. Speiser, N. Esser, S. Wippermann, and W. G. Schmidt. Surface vibrational raman modes of In:$Si(111)(4 \times 1)$ and (8×2) nanowires. *Phys. Rev. B*, 94:075417, 2016.

[87] T. Frigge, B. Hafke, T. Witte, B. Krenzer, C. Streubühr, A. Samad Syed, V. Mikšić Trontl, I. Avigo, P. Zhou, M. Ligges, D. von der Linde, U. Bovensiepen, M. Horn von Hoegen, S. Wippermann, A. Lüke, S. Sanna, U. Gerstmann, and W. G. Schmidt. Optically excited structural transition in atomic wires on surfaces at the quantum limit. *Nature*, 544:207, 2017.

[88] C. W. Nicholson, M. Puppin, A. Lücke, U. Gerstmann, M. Krenz, W. G. Schmidt, L. Rettig, R. Ernstorfer, and M. Wolf. Excited-state band mapping and momentum-resolved ultrafast population dynamics in In/Si(111) nanowires investigated with XUV-based time- and angle-resolved photoemission spectroscopy. *Phys. Rev. B*, 99:155107, 2019.

[89] R. A. Kaindl, M. Wurm, K. Reimann, P. Hamm, A. M. Weiner, and M. Woerner. Generation, shaping, and characterization of intense femtosecond pulses tunable from 3 to 20 μm. *J. Opt. Soc. Am. B*, 17(12):2086–2094, 2000.

[90] C. Ventalon, J. M. Fraser, J.-P. Likforman, D. M. Villeneuve, P. B. Corkum, and M. Joffre. Generation and complete characterization of intense mid-infrared ultrashort pulses. *J. Opt. Soc. Am. B*, 23(2):332–340, 2006.

[91] C. Monney, M. Puppin, C. W. Nicholson, M. Hoesch, R. T. Chapman, E. Springate, H. Berger, A. Magrez, C. Cacho, R. Ernstorfer, and M. Wolf. Revealing the role of electrons and phonons in the ultrafast recovery of charge density wave correlations in $1T - TiSe_2$. *Phys. Rev. B*, 94:165165, 2016.

[92] M. Rini, R. Tobey, N. Dean, J. Itatani, Y. Tomioka, Y. Tokura, R. W. Schoenlein, and A. Cavalleri. Control of the electronic phase of a manganite by mode-selective vibrational excitation. *Nature*, 449(7158):72, 2007.

[93] M. Rini Z. Hao, R. W. Schoenlein, C. Giannetti, F. Parmigiani, S. Fourmaux, J. C. Kieffer, A. Fujimori, M. Onoda, S. Wall, and A. Cavalleri. Optical switching in VO_2 films by below-gap excitation. *Applied Physics Letters*, 92(18):181904, 2008.

[94] B. Mayer, C. Schmidt, A. Grupp, J. Bühler, J. Oelmann, R. E. Marvel, R. F. Haglund, T. Oka, D. Brida, A. Leitenstorfer, and A. Pashkin. Tunneling breakdown of a strongly correlated insulating state in VO_2 induced by intense multiterahertz excitation. *Phys. Rev. B*, 91:235113, 2015.

[95] A. X. Gray, M. C. Hoffmann, J. Jeong, N. P. Aetukuri, D. Zhu, H. Y. Hwang, N. C. Brandt, H. Wen, A. J. Sternbach, S. Bonetti, A. H. Reid, R. Kukreja, C. Graves, T. Wang, P. Granitzka, Z. Chen, D. J. Higley, T. Chase, E. Jal, E. Abreu, M. K. Liu, T.-C. Weng, D. Sokaras, D. Nordlund, M. Chollet, R. Alonso-Mori, H. Lemke, J. M. Glownia, M. Trigo, Y. Zhu, H. Ohldag, J. W. Freeland, M. G. Samant, J. Berakdar, R. D. Averitt, K. A. Nelson, S. S. P. Parkin, and H. A. Dürr. Ultrafast terahertz field control of electronic and structural interactions in vanadium dioxide. *Phys. Rev. B*, 98:045104, 2018.

[96] L. Keldysh. Ionization in the field of a strong electromagnetic wave. *Journal of Experimental and Theoretical Physiscs (U.S.S.R.)*, 20(5):1307–1314, 1965.

[97] C. W. Nicholson. *Electronic Structure and Dynamics of Quasi-One Dimensional Materials*. PhD thesis, Freie Universität Berlin, 2017. `https://refubium.fu-berlin.de/handle/fub188/22174`, accessed on 2019-03-09.

[98] A. Subedi, A. Cavalleri, and A. Georges. Theory of nonlinear phononics for coherent light control of solids. *Phys. Rev. B*, 89:220301, 2014.

[99] M. Först, R. Mankowsky, H. Bromberger, D. M. Fritz, H. Lemke, D. Zhu, M. Chollet, Y. Tomioka, Y. Tokura, R. Merlin, J. P. Hill, S. L. Johnson, and A. Cavalleri. Displacive lattice excitation through nonlinear phononics viewed by femtosecond x-ray diffraction. *Solid State Communications*, 169:24 – 27, 2013.

[100] S. Kaiser, C. R. Hunt, D. Nicoletti, W. Hu, I. Gierz, H. Y. Liu, M. Le Tacon, T. Loew, D. Haug, B. Keimer, and A. Cavalleri. Optically induced coherent transport far above T_c in underdoped $YBa_2Cu_3O_{6+\delta}$. *Phys. Rev. B*, 89:184516, 2014.

[101] W. Hu, S. Kaiser, D. Nicoletti, C. R. Hunt, I. Gierz, M. C. Hoffmann, M. Le Tacon, T. Loew, B. Keimer, and A. Cavalleri. Optically enhanced coherent transport in $YBa_2Cu_3O_{6.5}$ by ultrafast redistribution of interlayer coupling. *Nature Materials*, 13(11):705, 2014.

[102] R. Mankowsky, A. Subedi, M. Först, S. O. Mariager, M. Chollet, H. T. Lemke, J. S. Robinson, J. M. Glownia, M. P. Minitti, A. Frano, M. Fechner, N. A. Spaldin, T. Loew, B. Keimer, A. Georges, and A. Cavalleri. Nonlinear lattice dynamics as a basis for enhanced superconductivity in $YBa_2Cu_3O_{6.5}$. *Nature*, 516(03):71, 2014.

[103] D. H. Dunlap and V. M. Kenkre. Dynamical localization of a charged particle moving under the influence of an electric field. *Phys. Rev. B*, 34:3625, 1986.

[104] H. Lignier, C. Sias, D. Ciampini, Y. Singh, A. Zenesini, O. Morsch, and E. Arimondo. Dynamical control of matter-wave tunneling in periodic potentials. *Phys. Rev. Lett.*, 99:220403, 2007.

[105] G. Jotzu, M. Messer, F. Görg, D. Greif, R. Desbuquois, and T. Esslinger. Creating state-dependent lattices for ultracold fermions by magnetic gradient modulation. *Phys. Rev. Lett.*, 115:073002, 2015.

[106] L. D. Landau and E. M. Lifshitz. *Statistical Physics*, volume 5. Pergamon Press Ltd., 3rd edition, 1980.

[107] M. A. Sentef, M. Claassen, A. F. Kemper, B. Moritz, T. Oka, J. K. Freericks, and T. P. Devereaux. Theory of Floquet band formation and local pseudospin textures in pump-probe photoemission of graphene. *Nature Communications*, 6:7047, 2015.

Acknowledgments

Glossary, Acronyms and Symbols

For reference, a list of the most common acronyms and symbols is provided.

Acronyms

1D	one dimensional. v, vi, 1, 3, 4, 31, 33, 40, 44
2D	two dimensional. 1, 31, 44
ARPES	angular-resolved photoemission spectroscopy. 1, 20, 31, 32, 36, 38, 39, 50, 73
BBO	β-Barium Borate. 23, 24, 27
CDW	charge density wave. v, 1, 14, 15, 49–60, 62, 63, 66, 69
CPA	chirped pulse amplification. 22
DCH	direct current heating. 36
DFG	difference-frequency generation. 22, 26, 27
DFT	density functional theory. 31, 32, 39, 52
EDC	energy distribution curve. 40–42, 46, 73, 75
FD-fit	Fermi-Dirac distribution fit. 41
FROG	frequency-resolved optical gating. 22
FTIR	Fourier-transform interferometer. 28
FWHM	full-width at half-maximum. 17, 20, 22, 25–27, 62, 70, 71, 74, 75
HHG	high-harmonic generation. 22–25
HSA	hemispherical analyzer. 20
IMPRS-UFAST	International Max Planck Research School for Ultrafast Imaging and Structural Dynamics. ix
IR	infrared. v, 9, 11, 14, 26, 44, 63, 64
LAPE	laser assisted photoemission. 29, 42, 45, 56, 66
LEED	low-energy electron diffraction. 31, 32, 36, 37
MCP	micro channel plate. 26

Symbols and Constants

$\mathcal{E}_B$	binding energy. 18, 20	
m^*	effective mass. 13, 72	
$\mathcal{E}_{\mathbf{gap}}$	size of the direct band gap. v, vi, 5, 49, 72	
$\mathcal{E}_{\mathbf{kin}}$	kinetic energy. 18, 20	
$\mathcal{E}$	energy. 19, 40	
ε	eigen energy of Hamiltonian. 3, 4	
ϵ_0	dielectric constant ($8.854187817 \times 10^{12}$ F/m $= (\mu_0 c_0^2)^{-1}$). 71	
$\varepsilon_{\mathbf{F}}$	Fermi energy. 4, 8	
F	free energy. 8, 67	
$f_{\mathbf{FD}}$	Fermi-Dirac distribution. 4, 20, 73, 74	
g	electron-phonon coupling constant. 7, 12, 75	
γ	electronic heat capacity proportionality constant. 12, 75	
H	energy transfer from electronic to phononic system. 11	
$\mathcal{H}$	Hamiltonian. 3, 7, 19	
$\hbar$	reduced Planck constant ($1.054571800 \times 10^{34}$ Js). 3, 4, 7, 8, 18	
I	intensity. 19, 73	
k	wave vector, momentum. 3	
k_B	Boltzmann's constant 1.380×10^{-23} J/K, $8.617 \times 10 - 5$ eV/K. 4, 8, 74	
$\gamma_{\mathbf{K}}$	Keldysh Parameter. 58, 59, 72	
$k_{\mathbf{F}}$	Fermi wavevector. 5, 6, 8	
λ	wavelength. 23, 24	
μ	chemical potential. 4	
$n(\varepsilon)$	density of states. 4, 73	
ϕ	phase of the complex order parameter. 8	
P	power. 71	
Φ	work function. 18, 19	
$\phi(x, t)$	phase fluctuations of the order parameter. 9	
$\phi_{\mathbf{ext}}$	external perturbation. 6	
ψ_n	electronic wave function. 3	
Q	atomic displacement/phonon coordinate. 13, 14	
$\rho(x)$	charge density. 6	
$\rho^{\mathbf{ind}}$	induced charge distribution. 6	
S	heating of the electronic system due to the light pulse. 11	
Σ	electron proper self energy. 20, 39	
T	temperature. 2	
τ	lifetime. v, 52	
T_c	critical temperature (for InSi 125K). v, 2, 8, 68	
$T_{\mathbf{el}}$	electronic temperature. 11, 75	
$T_{\mathbf{ph}}$	phononic temperature. 11, 75	